

## INFORMATION TO USERS

This reproduction was made from a copy of a document sent to us for microfilming. While the most advanced technology has been used to photograph and reproduce this document, the quality of the reproduction is heavily dependent upon the quality of the material submitted.

The following explanation of techniques is provided to help clarify markings or notations which may appear on this reproduction.

1. The sign or "target" for pages apparently lacking from the document photographed is "Missing Page(s)". If it was possible to obtain the missing page(s) or section, they are spliced into the film along with adjacent pages. This may have necessitated cutting through an image and duplicating adjacent pages to assure complete continuity.
2. When an image on the film is obliterated with a round black mark, it is an indication of either blurred copy because of movement during exposure, duplicate copy, or copyrighted materials that should not have been filmed. For blurred pages, a good image of the page can be found in the adjacent frame. If copyrighted materials were deleted, a target note will appear listing the pages in the adjacent frame.
3. When a map, drawing or chart, etc., is part of the material being photographed, a definite method of "sectioning" the material has been followed. It is customary to begin filming at the upper left hand corner of a large sheet and to continue from left to right in equal sections with small overlaps. If necessary, sectioning is continued again—beginning below the first row and continuing on until complete.
4. For illustrations that cannot be satisfactorily reproduced by xerographic means, photographic prints can be purchased at additional cost and inserted into your xerographic copy. These prints are available upon request from the Dissertations Customer Services Department.
5. Some pages in any document may have indistinct print. In all cases the best available copy has been filmed.

**University  
Microfilms  
International**

300 N. Zeeb Road  
Ann Arbor, MI 48106



8500627

**Nealon, Michael James**

**QUASI TWO-DIMENSIONAL ACCUMULATION LAYER ON N-TYPE INDIUM-  
ARSENIDE IN TIPPED MAGNETIC FIELDS**

*The University of Oklahoma*

**PH.D. 1984**

**University  
Microfilms**

**International** 300 N. Zeeb Road, Ann Arbor, MI 48106



PLEASE NOTE:

In all cases this material has been filmed in the best possible way from the available copy. Problems encountered with this document have been identified here with a check mark ☒.

1. Glossy photographs or pages \_\_\_\_\_
2. Colored illustrations, paper or print \_\_\_\_\_
3. Photographs with dark background \_\_\_\_\_
4. Illustrations are poor copy \_\_\_\_\_
5. Pages with black marks, not original copy \_\_\_\_\_
6. Print shows through as there is text on both sides of page \_\_\_\_\_
7. Indistinct, broken or small print on several pages ☒ \_\_\_\_\_
8. Print exceeds margin requirements \_\_\_\_\_
9. Tightly bound copy with print lost in spine \_\_\_\_\_
10. Computer printout pages with indistinct print \_\_\_\_\_
11. Page(s) \_\_\_\_\_ lacking when material received, and not available from school or author.
12. Page(s) \_\_\_\_\_ seem to be missing in numbering only as text follows.
13. Two pages numbered \_\_\_\_\_. Text follows.
14. Curling and wrinkled pages \_\_\_\_\_
15. Other \_\_\_\_\_

University  
Microfilms  
International



UNIVERSITY OF OKLAHOMA  
GRADUATE COLLEGE

QUASI TWO-DIMENSIONAL ACCUMULATION  
LAYER ON  $n$ -TYPE  $\text{InAs}$  IN  
TIPPED MAGNETIC FIELDS

A DISSERTATION  
SUBMITTED TO THE GRADUATE FACULTY  
in partial fulfillment of the requirements for the  
degree of  
DOCTOR OF PHILOSOPHY

By  
MICHAEL J. NEALON  
Norman, Oklahoma  
1984

QUASI TWO-DIMENSIONAL ACCUMULATION

LAYER ON  $n$ -TYPE  $\text{InAs}$  IN

TIPPED MAGNETIC FIELDS

A DISSERTATION

APPROVED FOR THE DEPARTMENT OF

PHYSICS AND ASTRONOMY

Approved by

Ryan I. Duggan  
W. F. R. R. R. R. R.  
Patrick H. R. R. R.  
John J. R. R. R.  
Rajendra Singh



## **ACKNOWLEDGEMENT**

Those people who have contributed to this work know who they are, with the possible exception of Bill Kloepping.

## TABLE OF CONTENTS

	Page
List of Tables . . . . .	vi
List of Figures . . . . .	vii
 <b>CHAPTER</b>	
I. Introduction . . . . .	1
II. Preliminary Considerations . . . . .	7
A. General Background . . . . .	7
1. MOSFET . . . . .	7
2. Energy Band Picture . . . . .	8
3. Conductance . . . . .	11
4. Transconductance . . . . .	12
5. Capacitance . . . . .	13
B. Potential Well . . . . .	15
1. Schrödinger's Equation . . . . .	15
2. Density of States . . . . .	16
3. Non-Parabolicity . . . . .	18
C. Electric Subbands . . . . .	19
1. Self-Consistent Potential . . . . .	19

2. Potential Approximations . . . . .	22
D. Magnetic Field . . . . .	23
1. Normal Magnetic Field . . . . .	23
2. Parallel Magnetic Field . . . . .	26
3. Tipped Magnetic Field . . . . .	30
E. Accumulation on InAs . . . . .	31
1. Bulk Properties of InAs . . . . .	31
2. 1971-1973 . . . . .	32
3. 1977-1979 . . . . .	34
4. 1980-1982 . . . . .	35
III. Experimental Apparatus . . . . .	37
A. Cryostat . . . . .	37
B. Circuit Analysis . . . . .	40
C. Sample Preparation . . . . .	45
D. Temperature . . . . .	49
IV. Data and Analysis . . . . .	57
A. Introduction . . . . .	57
B. Normal Field . . . . .	59
1. Shubnikov-de Haas Effect . . . . .	59
2. Spin Splitting . . . . .	64
C. Parallel Field . . . . .	66
1. Hybrid Subbands . . . . .	66
2. Spin Splitting . . . . .	75

D. Tipped Field . . . . .	79
E. Discussion of Parallel and Tipped Fields . . . . .	87
1. Electrical Transport . . . . .	87
2. Infrared Absorption . . . . .	90
F. Temperature Dependence of Hybrid Oscillation	
Amplitude . . . . .	94
G. Magnetic Freeze-Out of Impurity Band Conduction . .	99
V. Conclusions . . . . .	108
A. Summary . . . . .	108
B. Further Investigations . . . . .	110
APPENDICES	
A. Properties of Bulk InAs . . . . .	112
B. Physical Constants and Conversion Factors . . . . .	113
REFERENCES . . . . .	114

## LIST OF TABLES

TABLE	Page
I. Triangular Well Approximation for n-InAs . . . . .	28
II. Sample Properties . . . . .	46
III. Thermometer Calibration . . . . .	52
IV. Population Rates and Threshold Shifts . . . . .	72

## LIST OF FIGURES

FIGURE	Page
1. MOSFET . . . . .	8
2. Energy Band Picture for an n-type Semiconductor . . . . .	9
3. Conductance of a p-type MOSFET . . . . .	11
4. Transconductance of a p-type MOSFET . . . . .	12
5. Capacitance of a p-type MOSFET . . . . .	13
6. Self-consistent Potential, Dispersion Relation and Density of States . . . . .	18
7. Landau Levels . . . . .	26
8. Dispersion Relations . . . . .	30
9. Cryostat . . . . .	38
10. Sample Rotation Mechanism . . . . .	41
11. Schematic Circuit . . . . .	43
12. Bulk Magnetoresistance . . . . .	43
13. Complete Circuit for Transconductance-vs-Gate Voltage . . . .	44
14. Cleaning the Sample . . . . .	47
15. Source/Drain Connection . . . . .	48
16. Gate Connection . . . . .	49

17. Wheatstone Bridge . . . . .	51
18. Temperature Gradient . . . . .	55
19. Shubnikov-de Haas Oscillations . . . . .	60
20. Fan Chart . . . . .	62
21. Landau Level Sequence . . . . .	63
22. Surface Density . . . . .	63
23. Spin Splitting . . . . .	65
24. Parallel Field Transconductance . . . . .	68
25. Depopulation Mechanism . . . . .	68
26. Schematic Picture of Conductance . . . . .	70
27. Hybrid Fan Chart . . . . .	70
28. Hybrid Oscillations in Sample IAS/34( $10^{17}$ ) . . . . .	74
29. Hybrid Fan Chart . . . . .	74
30. Spin Split Hybrid Oscillations . . . . .	76
31. Spin Split Hybrid Fan Chart . . . . .	76
32. Spin Split Hybrid Dispersion Relation . . . . .	78
33. Transconductance in Tipped Fields . . . . .	80
34. Transconductance in Tipped Fields . . . . .	82
35. Transconductance- <i>versus</i> -Angle . . . . .	84
36. Transconductance- <i>versus</i> - $\frac{1}{H_{\perp}}$ . . . . .	84
37. Depopulation of the $i = 2$ Subband . . . . .	85
38. Hybrid Dispersion Relation . . . . .	96
39. Temperature Dependence of the Hybrid Oscillation Amplitude . . . . .	96

40. Amplitude Decay . . . . .	98
41. Hybrid Subband Energy Spacing . . . . .	100
42. Impurity Band Transconductance . . . . .	100
43. Impurity Band Density of States . . . . .	102
44. Magnetic Freeze-Out . . . . .	102
45. Electron Clouds . . . . .	106
46. Capacitance . . . . .	107



# **QUASI TWO-DIMENSIONAL ACCUMULATION LAYER ON n-TYPE InAs IN TIPPED MAGNETIC FIELDS**

## **CHAPTER I**

### **INTRODUCTION**

By reducing the dimensionality of a physical system the complexity of the system is reduced, which in general, if none of the physical properties are lost, leads to a better understanding of the system. Furthermore, unique properties of the reduced dimensional system may be revealed. For example, a monolayer of helium atoms adsorbed onto the surface of a substrate condenses into a two-dimensional solid at low temperatures, in contrast to the three-dimensional bulk helium properties.<sup>1</sup> In fact, a general class of two-dimensional systems realizable for experimental study is the adsorption of a monolayer of atoms or molecules, such as Ar, Ne, O<sub>2</sub> or N<sub>2</sub>, onto a substrate such as glass or graphite.<sup>2</sup> Another example of a two-dimensional system of considerable interest is a two-dimensional electron gas (2DEG).<sup>3</sup> An electron gas can be reduced to a two-dimensional

system by requiring that it be confined in one direction over a distance less than the electron wavelength in that direction. Many other systems behave two-dimensionally, including, but certainly not limited to, liquid crystals, superconducting thin metal films (if the superconducting coherence length is greater than the film thickness), and certain bulk materials such as tantalum disulfide, which has an anisotropic conductivity.<sup>4</sup>

Numerous physical properties of two-dimensional systems are of interest, two of which are the electrical transport and the nature of various phases and phase transitions. Solid, liquid and gaseous phases have been observed in monolayers of atoms and molecules. In the solid phase, the two-dimensional lattice can make a transition between phases commensurate and incommensurate with the substrate lattice.<sup>5</sup> Another transition of interest is the onset of two-dimensional superfluidity in thin helium films a few atoms thick.

Transport properties reveal a variety of information about the fundamental nature of a two-dimensional electron gas. Localization, for example, gives rise to the minimum metallic conductivity which, in two dimensions, is independent of material constants.<sup>6</sup> Effects that can be tested experimentally in a 2DEG include, among others, the predictions of many-body theory (for example, the enhancement of the Landé g-factor<sup>7</sup>) and metal-insulator transitions (via percolation theory<sup>8</sup> for example).

A two-dimensional electron gas of low number density (typically  $\sim 10^9/\text{cm}^2$ ) can be produced by injecting electrons onto the smooth sur-

face of superfluid liquid helium. The electrons are held near the surface by their image charges inside the fluid. Novel physics of this system is the condensation of the 2DEG into an electron solid (Wigner lattice) at low temperatures and low densities.<sup>9</sup>

A 2DEG with a greater number density can be produced in a semiconductor by binding the charge carriers in a potential well at the semiconductor surface. An example of such a system is the potential well formed by an externally applied bias voltage at the semiconductor surface in a metal-oxide-semiconductor field effect transistor (MOSFET). An accumulation or inversion space charge layer forms in this potential well. Another example is a heterojunction between two dissimilar semiconductors, such as Ge and GaAs. Because the band gaps are mismatched, a quantum well in which forms a 2DEG is produced at the interface. Heterojunctions are used commercially in a variety of applications including use as diodes and photodetectors.

A superlattice is the periodic potential produced by multiple quantum wells. One kind of superlattice can be made by stacking heterojunctions. One interesting superlattice of this type is the modulation doped GaAs/Ga<sub>1-x</sub>Al<sub>x</sub>As structure.<sup>10</sup> In this device, only the Ga<sub>1-x</sub>Al<sub>x</sub>As layers are doped (with Si), yet the 2DEG's are formed in the GaAs. The electron mobility is much higher than in uniformly doped heterojunction superlattices because the primary scatters, the donor ions, are separated from the 2DEG by the potential barrier at the junction. Another type of superlattice

is the “nipi” structure of alternating n- and p-doped layers. This structure has a sawtooth potential in which form alternating layers of electrons and holes.<sup>11</sup>

The quantum Hall effect was first discovered in a 2DEG inversion layer in a silicon MOSFET.<sup>12</sup> Unlike the usual three dimensional Hall effect, the quantum Hall effect is observed as a constant value of Hall resistance over a small range of (2D) electron densities. These constant values of Hall resistance are quantized in the sense that they are proportional to  $\hbar/e^2 i$ , where  $i$  is an integer. Classically, the electrons undergo cyclotron orbits about the magnetic field direction (normal to the plane of the 2DEG) and the electron energies become quantized into highly degenerate harmonic oscillator energies, called Landau levels. The quantum number  $i$  is the number of Landau levels into which the electrons are distributed. Since its discovery, the quantum Hall effect has been used to determine a value for the fine structure constant, and is under study for use as a secondary resistance standard. The quantum Hall effect has been seen also in a GaAs/Ga<sub>1-x</sub>Al<sub>x</sub>As heterojunction. In this device the 2D number density is constant, although plateaus in the Hall resistance are observed as the magnetic field strength is varied. However, at very high magnetic fields ( $\geq 10$  Tesla) anomalous behavior is apparent. The plateaus occur at fractional quantum numbers:  $i = \frac{1}{3}, \frac{2}{3}, \frac{2}{5}, \dots$  *et al.*<sup>13,14</sup> These numbers indicate the fraction of the ground state Landau level which is filled by the electrons in the 2DEG. The implication here is that the ground state Landau level is not

a smooth energy distribution but has gaps at these fractional filling factors. Although not well understood yet, the anomalous behavior is thought to result from a new type of ground state: an incompressible two-dimensional electron liquid.<sup>15</sup>

Apart from curiosity about the fundamental nature of a two-dimensional electron gas, the study of these space charge layers is important for practical reasons as well. The space charge layer on the surface of Si has been studied extensively,<sup>3</sup> mainly because of its importance in the commercial semiconductor industry.<sup>16</sup> In fact, not only are most semiconductor devices made of Si, but the Si-SiO<sub>2</sub> metal-oxide-semiconductor is the most common structure for both logic and memory devices in digital electronic components.

One reason that MOS devices are of particular interest, both commercially and scientifically, is that the number of charge carriers in the 2DEG is variable simply by varying an externally applied gate bias voltage. In the energy band picture, this is equivalent to changing the Fermi energy level.

The major scattering mechanisms near the surface (at low temperatures where phonons are frozen out) are Coulomb scattering from fixed charge centers and surface roughness scattering. In a uniformly doped semiconductor the majority of the donor ions reside in the bulk semiconductor, so the number of fixed donor charges near the surface is small compared to the number of oxide and impurity charges in the interface. Furthermore,

if the oxide layer is  $\text{SiO}_2$ , the number of charges trapped in the interface ( $\leq 10^{10} \text{ cm}^{-2}$ ) is small compared to the number of charges in the 2DEG (typically  $10^{10} - 10^{13} \text{ cm}^{-2}$ ).

Although the 2DEG on semiconductor surfaces is a mature field of study there is still considerable interest and new developments in the electronic properties of such systems, especially in novel compound semiconductors and heterostructures. An ideal 2DEG is one in which the Landau quantization depends on only the perpendicular magnetic field component. Not all 2DEGs are ideally two-dimensional. The 2DEG accumulation layer on InAs (the first material to directly exhibit surface subband quantization<sup>109</sup>) is quasi two-dimensional since the length of interest, the cyclotron radius, is on the order of the width of the surface potential well. An investigation of the subband population in tipped fields is an important method of probing the quasi 2D accumulation layer, since the parallel field component does have an effect on the electron energies.

A general description of the physics of an ideal 2DEG is given in Chapter II, and the reader is referred to Reference 3 for a complete review of the subject. The methods of taking data and the apparatus are described in Chapter III. The analysis of the data is presented in Chapter IV followed by a summary and a few concluding remarks in Chapter V.

## CHAPTER II

### PRELIMINARY CONSIDERATIONS

#### A. General Background

##### 1. MOSFET

A metal-oxide-semiconductor field effect transistor (MOSFET) is shown schematically in Figure 1. Because the oxide is an electrical insulator, the configuration of the MOSFET is that of a parallel plate capacitor. A potential bias applied across the semiconductor and gate electrode, called the gate voltage  $V_G$ , will induce an electric field in the insulator. Unlike a metal capacitor, the electric field does not vanish at the surface. Because the semiconductor dielectric constant is less than that of a metal but greater than that of the oxide the electric field penetrates into the semiconductor, yet decays to zero in the semiconductor bulk. The magnitude of the electric field  $F$  just inside the semiconductor is (cgs units)

$$F = \frac{4\pi e(N_s + N_{depl})}{\kappa_{SC}}, \quad (2.1)$$

where  $e$  is the magnitude of the electronic charge,  $N_s$  and  $N_{depl}$  are the two-dimensional number densities of the surface charge and depletion charge, respectively, and  $\kappa_{SC}$  is the semiconductor dielectric constant.

## 2. Energy Band Picture

The energy band picture for an n-type semiconductor is shown in Figure 2. As a result of the electric field in the space charge region, the conduction and valence energy band edges bend near the semiconductor surface. This band bending is measured by the electrostatic surface potential,  $\phi_s$ , associated with the surface electric field. The flat band condition is shown in Figure 2a. In this case the surface potential is zero, the band edges are flat, and  $N_s = 0$ . For a real MOSFET this condition does not necessarily occur at  $V_G = 0$  because of fixed impurity charges or surface states at the semiconductor-insulator interface. In a degenerate semiconductor, the Fermi level is pinned above the conduction band edge (for n-type material), charges accumulate at the surface without an external gate bias, and flat band occurs at  $V_G \neq 0$ .

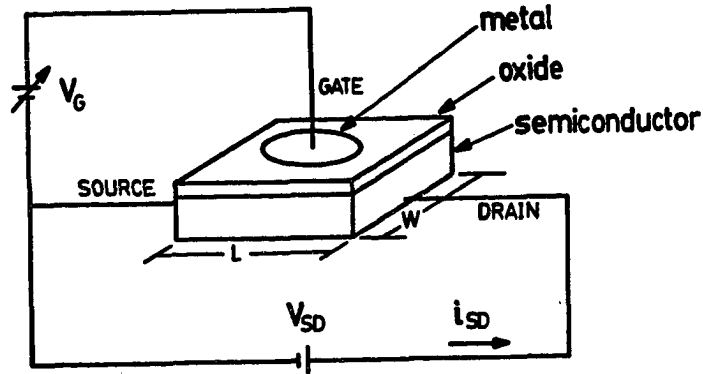


**Figure 1. MOSFET.** A schematic view of a metal-oxide-semiconductor field effect transistor of length  $L$  and width  $W$ . The MOSFET is configured as a parallel plate capacitor with the oxide thickness typically about  $1000 \text{ \AA}$ . The semi-transparent metal gate is evaporated onto the oxide. The space charge layer is

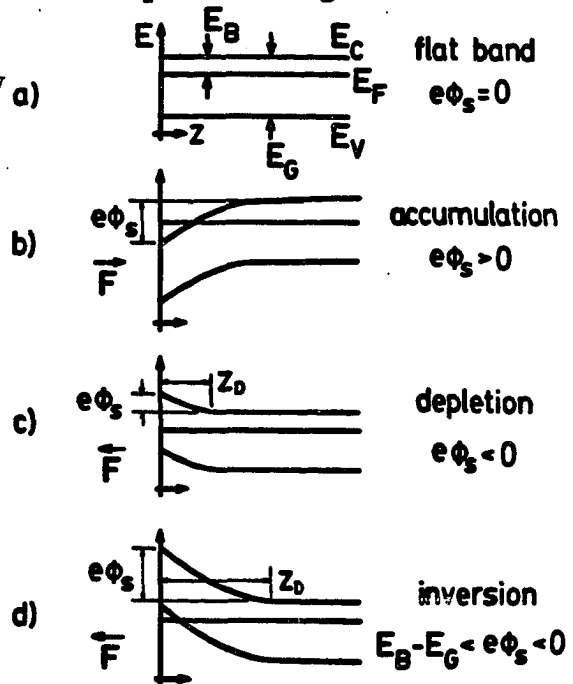
formed inside the semiconductor at the semiconductor-oxide interface. The gate voltage  $V_G$  determines the number of charge carriers in the space charge layer. Transport properties of the space charge layer are probed through the externally applied source/drain current  $i_{SD}$ , which is produced by the source/drain voltage  $V_{SD}$ .



With the electric field pointing into the semiconductor, which corresponds to a positive gate voltage relative to the semiconductor, the band edges in the n-type semiconductor bend down, as in Figure 2b. This creates a one-dimensional potential energy well, bounded by the infinite potential of the insulator and the screened self-consistent potential of the conduction band edge. Electrons in the conduction band occupy allowed, discrete energy levels in the potential well below the Fermi level.

The band edges bend up with a negative gate bias, as in Figures 2c and 2d. The electric field pushes the majority electrons away from the surface and forms the depletion region of net positive charge due to the

Figure 2. Energy Band Picture for an n-type Semiconductor. The electron energy  $E$  is plotted as a function of spatial distance  $z$  into the semiconductor near the semiconductor-insulator interface ( $z = 0$ ).  $E_F$  is the Fermi energy,  $E_C$  and  $E_V$  are the conduction and valence band edges, respectively,  $E_B = E_C - E_F$ , and  $E_G = E_C - E_V$ . The flat band condition (a) occurs if the surface electrostatic potential  $\phi_s$  is zero. (b) For a positive surface potential the conduction and valence band edges bend down (an equal amount). Accumulation of electrons near the surface occurs if  $e\phi_s > 0$ , but bound states below the Fermi level occur if  $e\phi_s > E_B$ . The accumulation threshold gate voltage is such that the potential well is deep enough to support a bound state.  $F$  indicates the direction of the electric field in the space charge region. (c) A negative surface potential bends the band edges up, creating a depletion region of width  $z_D$ . The particular case shown here is the threshold for inversion, i.e.,  $E_F - E_V - e\phi_s = E_B$ . (d) Inversion of the surface space



charge layer occurs if  $E_B - E_G < e\phi_s < 0$ . The valence band edge bends up above the Fermi level, and minority holes occupy bound states in the potential well above the Fermi level. The inversion layer is electronically insulated from the bulk by the depletion region.

spatially fixed donors. The width of the depletion region,  $z_D$ , is essentially the penetration depth of the electric field, and is given by

$$z_D = \left[ \frac{\kappa_{SC} \varphi_D}{2\pi e |N_A - N_D|} \right]^{\frac{1}{2}}, \quad (2.2)$$

where  $\varphi_D$  is the surface potential due to the fixed depletion layer charge only,<sup>17</sup> and  $N_A$  and  $N_D$  are the number per unit volume of ionized acceptors and donors, respectively. At low temperatures,  $e\varphi_D \simeq E_F - E_V$ . If the gate bias is strong enough, the valence band edge bends up above the Fermi level, creating an inverted space charge layer of holes. Similar constructions are made for p-type semiconductors.

The threshold gate voltage,  $V_T$ , for conduction in accumulation or inversion layers is not universally defined<sup>96</sup> because the onset of conduction is not sharp. The threshold voltage may be taken, in an n-type inversion layer for example, as the condition that

$$E_F - E_V - e\varphi_s = E_B, \quad (2.3)$$

as in Figure 2c. For n-type accumulation, as in Figure 2b, the threshold voltage for bound subbands is such that the potential well is deep enough to support a bound state below the Fermi level. The threshold voltage is often taken experimentally as the linear extrapolation of gate voltage to zero conductance in the turn-on region of either the conductance or transconductance-*versus*-gate voltage curves.

### 3. Conductance

The sheet conductance,  $G = i_{SD}/V_{SD}$ , of a surface space charge layer can be found by measuring the source/drain voltage  $V_{SD}$ , and the current through the charge layer,  $i_{SD}$ . With the geometrical factors from Figure 1, then, the two-dimensional sheet conductivity is

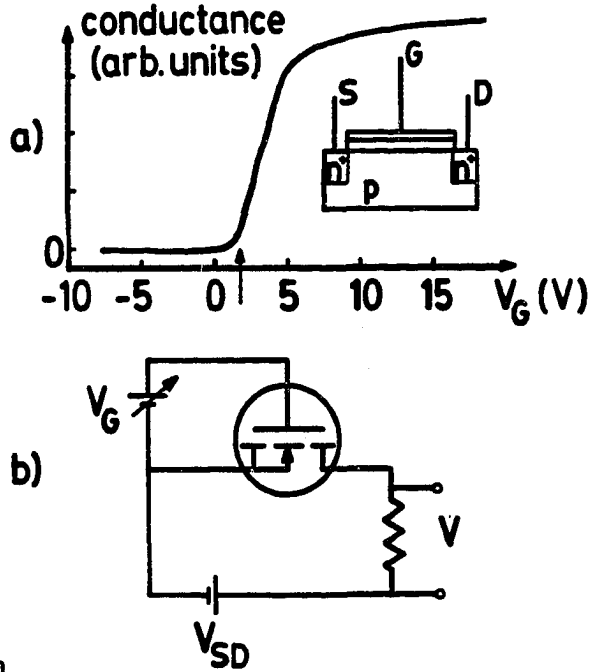
$$\sigma = \frac{GL}{W}. \quad (2.4)$$

The conductivity is also given in terms of the charge carrier mobility  $\mu$ ,

$$\sigma = eN_s\mu. \quad (2.5)$$

The SI unit of two-dimensional conductance is  $\Omega^{-1}$ .

**Figure 3. Conductance of a Commercial p-type MOSFET.** The n-channel enhancement (normally off) MOSFET has an on state resistance of nominally  $3\Omega$ . Source/-drain contacts are made through heavily doped  $n^+$  regions. The conductance is plotted against gate voltage in (a). The threshold voltage (arrow),  $V_G \simeq +1.5V$  comes from the extrapolation to zero conductance of the turn-on region. Under accumulation,  $V_G < 0$ , the surface channel consists of majority holes and the  $n^+$  contacts are reverse biased, therefore, no conduction. Under inversion,  $V_G > 0$ , the surface channel consists of minority electrons and conduction occurs. The schematic circuit for conduction measurements is shown in (b). The voltage  $V$  is proportional to the MOSFET channel conductance if the channel resistance is much greater than the series resistance. The conductance is measured at a constant source/drain voltage  $V_{SD}$ .



The conductance as a function of gate voltage of a commercial n-channel enhancement (normally off) MOSFET is shown in Figure 3. The source/drain contacts to the p-type semiconductor are made with heavily doped  $n^+$  regions. With a strong negative gate voltage, the majority holes are attracted to the surface channel under accumulation, but because the source/drain contacts act like reverse biased diodes, the channel does not conduct. Under strong inversion with a positive gate voltage, the surface channel conducts through the minority electrons.

#### 4. Transconductance

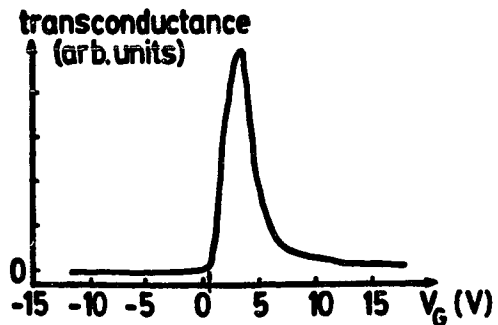
The transconductance,  $G_M$ , is a measure of how well a small change in gate voltage affects a change in the source/drain current (for amplifying or switching, for example), and is defined at constant  $V_{SD}$  as the derivative

$$\begin{aligned} G_M &\equiv \left. \frac{di_{SD}}{dV_G} \right|_{V_{SD}} \\ &= \frac{V_{SD}W}{L} \left. \frac{d\sigma}{dV_G} \right|_{V_{SD}}. \end{aligned} \quad (2.6)$$

Figure 4 shows the transconductance of the same MOSFET used in Figure

3. The transconductance is also a measure of the field effect mobility

**Figure 4. Transconductance of a Commercial p-type MOSFET.** The transconductance plotted against gate voltage is the slope of the curve in Figure 3. Here, the extrapolated threshold gate voltage for conduction under inversion is  $V_G \simeq +0.5V$ , a slightly different value than that given by the conductance curve.



$\mu_{FE} = G_M / C_{ins} V_{SD}$ , where  $C_{ins}$  is the insulator capacitance per unit area.

Because the surface channel is in parallel with the bulk semiconductor, the measured conductance can be written<sup>18–20</sup>

$$\frac{\sigma_b d_b + \sigma_s}{d}, \quad (2.7)$$

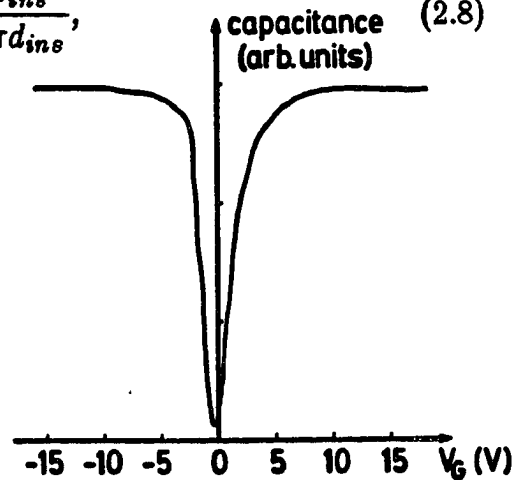
where  $\sigma_b = ne\mu$  is the bulk conductivity,  $d_b$  and  $d_s$  are the bulk and surface thicknesses, respectively, so  $d = d_b + d_s (\simeq d_b)$  is the overall thickness. The bulk conductivity and thickness have no gate voltage dependence, so the transconductance separates the surface and bulk properties. See Figure 12.

## 5. Capacitance

The MOS device capacitance consists of the series capacitance of the insulator and semiconductor, since the gate voltage is dropped across both, i.e.,  $V_G = V_{ins} + \varphi_s$ , where  $V_{ins}$  is the voltage drop across the insulator. The capacitance per unit area of the insulator is

$$C_{ins} = \frac{\kappa_{ins}}{4\pi d_{ins}}, \quad (2.8)$$

Figure 5. Capacitance of a Commercial p-type MOSFET. The capacitance (at 200 Hz) of the same MOSFET used in Figures 3 and 4. Under strong accumulation and inversion the capacitance value is that of the insulator. The minimum capacitance occurs near flat band.



where  $\kappa_{ins}$  and  $d_{ins}$  are the insulator dielectric constant and thickness, respectively. The semiconductor differential capacitance per unit area is

$$C_{SC} = \frac{dQ}{d\phi_s}, \quad (2.9)$$

where  $Q$  is the surface space charge per unit area. The total capacitance per unit area,  $C$ , is found from

$$\frac{1}{C} = \frac{1}{C_{ins}} + \frac{1}{C_{SC}}. \quad (2.10)$$

In the simplest approximation, the semiconductor capacitance is neglected, and the device capacitance is due to the insulator. This is a valid approximation for thick insulating layers ( $d_{ins} > 1 \mu\text{m}$  for Si-SiO<sub>2</sub> MOS devices<sup>21</sup>). This is valid also under strong gate bias, either accumulation or inversion, because the induced surface charge is tightly bound to the surface. A C-V curve for a MOS device exhibits a minimum near flat band if the semiconductor capacitance is not negligible, as in Figure 5, and in the limits of strong gate bias, both positive and negative, approaches the value of the insulator capacitance.

Under strong gate bias, the gate voltage is used as a measure of the two-dimensional number density via the insulator capacitance

$$N_s = \frac{C_{ins}}{e}(V_G - V_T). \quad (2.11)$$

The dielectric breakdown strength of the insulator limits  $N_s$  and the gate voltage. For a SiO<sub>2</sub> insulator, the breakdown strength is about  $10^7$  V/cm,

and  $\kappa_{ins} = 3.9$ , so  $N_s < 10^{13} \text{ cm}^{-2}$ , and for  $d_{ins} = 1000 \text{ \AA}$ , the maximum gate voltage is about 100 V.

## B. Potential Well

### 1. Schrödinger's Equation

The total energy  $E$  of a charge carrier in a space charge layer is found by solving Schrödinger's equation  $\mathcal{H}\Psi = E\Psi$ . For an isotropic effective mass  $m^*$  and a one-dimensional potential, the single particle Hamiltonian is separable

$$\mathcal{H} = \left[ \frac{\hat{p}_z^2}{2m^*} + V(z) \right] + \frac{1}{2m^*} [\hat{p}_x^2 + \hat{p}_y^2], \quad (2.12)$$

where the usual symbols are used for the components of the momentum operator, and  $V(z)$  is the potential energy of an electron in the well. The configuration space coordinates  $x$  and  $y$  are in the plane of the surface and  $z$  is normal to the surface. For free particle like motion in the plane of the surface, corresponding to Bloch waves, product wave functions are assumed

$$\Psi = \psi_i(z) e^{i\vec{k} \cdot \vec{r}}, \quad i = 0, 1, 2, \dots \quad (2.13)$$

where  $\vec{k} = (k_x, k_y)$  is the two-dimensional Bloch wavevector for motion in the plane of the surface, and  $\vec{r} = (x, y)$ . Schrödinger's equation then reduces to

$$\left[ -\frac{\hbar^2}{2m^*} \frac{\partial^2}{\partial z^2} + V(z) \right] \psi_i(z) = E_i \psi_i(z), \quad i = 0, 1, 2, \dots \quad (2.14)$$

with eigenvalues  $E_i$ . The total energy measured from the conduction band edge is therefore

$$E = E_i + \frac{\hbar^2}{2m^*}(k_x^2 + k_y^2). \quad i = 0, 1, 2 \dots \quad (2.15)$$

Because the electrons are assumed not to penetrate into the insulator, the one-dimensional envelope wavefunctions  $\psi_i(z)$  go to zero at the semiconductor-insulator interface (i.e., at  $z = 0$ ). In addition, because the electrons are bound closely to the surface, the wave functions vanish in the semiconductor bulk. The boundary conditions, then, are

$$\psi_i(0) = \psi_i(\infty) = 0. \quad (2.16)$$

The potential energy which appears in the Schrödinger equation can be found from Poisson's equation for the electrostatic potential  $\varphi(z) = -\frac{1}{e}V(z)$  in the space charge region,

$$\frac{d^2}{dz^2}\varphi(z) = -\frac{4\pi\rho(z)}{\kappa_{SC}}, \quad (2.17)$$

where  $\rho(z)$  is the net charge density. In the simplest approximation,  $\rho(z)$  is due to the mobile electrons and the spatially fixed uniformly distributed charge of the ionized donors. Because Schrödinger's and Poisson's equations are coupled through the potential energy, a self-consistent solution of the two equations is required in order to extract the energy eigenvalues.

## 2. Density of States

The energy dispersion relation (2.14) consists of a set of nested paraboloids of revolution; each paraboloid is called an electric subband,



and has a minimum energy value  $E_i$ . The conduction band electrons fill the one-electron levels of the subbands up to the Fermi energy, while the total number of carriers in the space charge layer is determined by  $V_G$ . Defining  $k_{\parallel}^2 = k_x^2 + k_y^2$ , the parabolic dispersion relation

$$E = E_i + \frac{\hbar^2 k_{\parallel}^2}{2m^*}, \quad i = 0, 1, 2, \dots \quad (2.18)$$

is shown in Figure 6. The constant energy "surface" is a circle with radius  $k_{\parallel}$ . In two-dimensional  $k$ -space the density of allowed wavevectors<sup>22</sup> is  $\frac{g_v g_s}{(2\pi)^2}$ , where  $g_s$  is the spin degeneracy, and the valley degeneracy,  $g_v$ , is the number of bulk conduction band minima which produce the space charge layer charge carriers. The number of allowed wavevectors in the range  $E$  to  $E + dE$  is  $2\pi k_{\parallel} dk_{\parallel}$ , so the two-dimensional density of states per unit area, per unit energy (referred to simply as the density of states) is

$$D(E) = \frac{g_v g_s}{(2\pi)^2} 2\pi k_{\parallel} \frac{dk_{\parallel}}{dE}. \quad (2.19)$$

For a single subband, the 2D density of states is

$$D(E) = \begin{cases} \frac{g_v g_s m^*}{2\pi \hbar^2}, & E \geq E_i \\ 0, & E < E_i \end{cases} \quad (2.20)$$

Unlike the cases in 1D and 3D, this 2D density of states is independent of energy. If more than one subband is occupied, the total density of states is the sum of the density of states of each subband (see Figure 6). The number of electrons in each subband per unit area,  $N_{Si}$ , is

$$N_{Si} = D(E)(E_F - E_i), \quad (2.21)$$

and the total number density is

$$N_s = \sum_i N_{Si}. \quad (2.22)$$

### 3. Non-parabolicity

If the dispersion relation is not parabolic then the effective mass and density of states are not constant, but depend on the energy of the charge carriers.<sup>23-26</sup> Using the notation  $m^*$  to represent the effective mass at the conduction band edge, the energy dispersion relation<sup>23</sup>

$$E\left(1 + \frac{E}{E_G}\right) = E_i + \frac{\hbar^2 k_{\parallel}^2}{2m^*} \quad i = 0, 1, 2, \dots \quad (2.23)$$

results in an effective mass enhancement for each subband

$$\begin{aligned} m^*(E) &= \hbar^2 \left( \frac{d^2 E}{dk_{\parallel}^2} \right)^{-1} \\ &= \left( 1 + \frac{2E}{E_G} \right) m^*. \end{aligned} \quad (2.24)$$

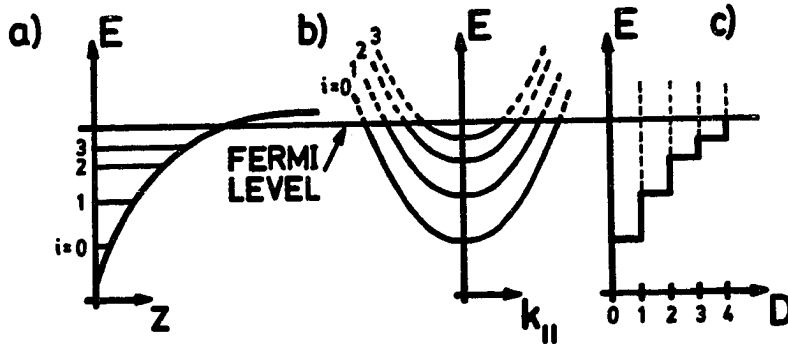


Figure 6. Self-consistent Potential, Dispersion Relation and Density of States. (a) The self-consistent potential for an n-type semiconductor, shown with four subbands. (b) The parabolic dispersion relation: energy  $E$  plotted against the in-plane wavevector  $k_{\parallel}$ . The energy minima of the electric subbands are  $E_i$ . (c) The density of states for one subband is independent of energy for a parabolic dispersion (dashed lines). The total density of states plotted here in units of  $\frac{2\pi 2m^*}{2\pi \hbar^2}$  is the sum of the density of the states for each occupied subband.

The density of states, enhanced over the usual 2D expression, is

$$D_i(E) = \begin{cases} \frac{g_v g_s m^*}{2\pi\hbar^2} \left(1 + \frac{2(E - E_i)}{E_G}\right), & E > E_i \\ 0, & E < E_i. \end{cases} \quad (2.25)$$

The number of electrons in each subband can be found by integrating over the density of states<sup>24</sup>

$$\begin{aligned} N_{Si} &= \int_{E_i}^{E_F} D_i(E) dE \\ &= \frac{g_v g_s m^*}{2\pi\hbar^2} (E_F - E_i) \left(1 + \frac{(E_F - E_i)}{E_G}\right). \end{aligned} \quad (2.26)$$

### C. Electric Subbands

#### 1. Self-Consistent Potential

Solving for the bound state energies of the subbands in a surface space charge layer, either accumulation or inversion, requires a self-consistent numerical calculation because the potential that appears in Poisson's equation depends on the wavefunction. However, with appropriate assumptions, various schemes have been used to obtain approximate solutions. Perhaps the simplest method is to model the potential as a triangular well,<sup>27</sup> which results in exact analytical solutions. This approximation works best for the lowest bound states because the self-consistent potential is linear deep in the well. Another approximate solution is to choose a variational wavefunction,<sup>28</sup> from which the energy eigenvalues can be calculated.

A third method is to model a reasonable decaying potential and to calculate the energies numerically.<sup>29</sup>

A self-consistent calculation of energy levels for an accumulation layer on *n*-type Si has been given by Stern<sup>30</sup> and by Ando.<sup>31</sup> Neglecting many-body effects (which require additional terms in the potential), the potential  $V(z)$  in Schrödinger's equation is composed of three terms

$$V(z) = V_s(z) + V_{depl}(z) + V_I(z). \quad (2.27)$$

The first term  $V_s(z)$  is the Hartree potential due to the surface accumulation electrons.<sup>32</sup> This term comes about because the electrons are assumed to respond to the average potential of all the other electrons. The potential is given by

$$V_s(z) = \frac{4\pi e^2}{\kappa_{SC}} \sum_i N_{Si} \left[ z - \int_0^z (z' - z) \psi^2(z') dz' \right], \quad (2.28)$$

where the terms in the brackets are summed over all occupied subbands  $i$ , and  $\psi$  is now the normalized wavefunction. The second term  $V_{depl}(z)$  arises from the electrostatic potential of the spatially fixed charge density associated with the minority acceptors. This corresponds to the depletion charge density in inversion layers. Under accumulation, however, the donor level near the semiconductor surface is bent below the Fermi level and becomes filled. The bulk donors provide the conduction band electrons which are free to occupy bound states in the accumulation layer. This term is given by<sup>30,31</sup>

$$V_{depl} = \begin{cases} \frac{4\pi e^2}{\kappa_{SC}} N_{depl} z \left(1 - \frac{z}{2z_D}\right), & z \leq z_D \\ \frac{4\pi e^2}{\kappa_{SC}} N_{depl} \frac{z_D}{2}, & z > z_D \end{cases} \quad (2.29)$$

$$(2.30)$$

with  $N_{depl} = N_a z_D$ , and

$$z_D = \left( \frac{\kappa_{SC} E_B}{2\pi e^2 N_A} \right)^{\frac{1}{2}}. \quad (2.31)$$

The last term in the potential,  $V_I(z)$ , is due to an image charge in the insulator. For a semi-infinite volume of semiconductor bounded at  $z = 0$  by a semi-infinite volume of insulator, the work done in moving an electron in the semiconductor, from  $z = \infty$  to a position  $z$ , against the image charge in the insulator is<sup>33</sup>

$$V_I(z) = \frac{(\kappa_{SC} - \kappa_{ins})}{4(\kappa_{SC} + \kappa_{ins})} \frac{e^2}{\kappa_{SC} z}. \quad (2.32)$$

These last two terms are small compared to  $V_s(z)$ . The numerical self-consistent calculation is done iteratively.<sup>34</sup> One method is to guess an initial input potential  $V(z)$  and from Schrödinger's equation calculate a wavefunction; this wavefunction then determines an output potential. For each succeeding step of the iteration, the new input potential is a linear combination of the last input and output potentials. This process continues until the input and output potentials converge. The wavefunctions, energy eigenvalues, and potential are then self-consistent.

## 2. Potential Approximations

In the triangular approximation, the potential well is

$$V(z) = \begin{cases} eFz, & z > 0 \\ \infty, & z < 0 \end{cases}, \quad (2.33)$$

where  $F$  is the electric field in the space charge region, assumed constant, and is given by equation (2.1). With this potential, exact solutions of Schrödinger's equation are obtained.<sup>27</sup> However, eigenvalues can be determined from the Bohr-Sommerfeld quantum condition<sup>35</sup> with a single classical turning point

$$\int \hat{p}_z dz = (i + \frac{3}{4})\pi\hbar. \quad i = 0, 1, 2, \dots \quad (2.34)$$

Letting  $\hat{p}_z = \hbar k_z = \sqrt{2m^*}(E_i - eFz)$ , and integrating from  $z = 0$  to

$$z = \frac{E_i}{eF} \equiv z_i \quad (2.35)$$

leads to the solution

$$E_i = \left[ \frac{3\hbar\pi(i + \frac{3}{4})eF}{2\sqrt{2m^*}} \right]^{\frac{2}{3}}. \quad i = 0, 1, 2, \dots \quad (2.36)$$

Neglecting the image term, the self-consistent potential is linear for small  $z$ . The triangular well is therefore a valid approximation close to the surface. For large  $z$ , the triangular potential overestimates the self consistent potential.

A one parameter variational wavefunction for the ground state is<sup>28</sup>

$$\psi(z) = \left(\frac{b^3}{2}\right)^{\frac{1}{2}} z e^{-\frac{b}{2}z}. \quad (2.37)$$

After the energy eigenvalue is found the parameter  $b$  is determined by minimizing the energy per electron,  $E/N_s$ . For a Si inversion layer (neglecting the image potential), the value of  $b$  which minimizes the energy is<sup>36</sup>

$$b = \left[ \frac{48\pi m_z^* e^2 (N_{depl} + \frac{11}{32} N_s)}{\hbar^2 \kappa_{SC}} \right]^{\frac{1}{3}}, \quad (2.38)$$

where  $m_z^*$  is the component of the effective mass normal to the surface. The utility of this method is that the calculations are more simple than the numerical self-consistent calculations. Also, the energy eigenvalue is in good agreement with the self-consistent calculation,<sup>27</sup> especially at large values of  $N_s$ .

For a thin (1000 Å) layer of InAs between layers of GaSb, the self-consistent potential has been modeled by<sup>29</sup>

$$V(z) = E_F \left( 1 - \frac{1}{(1 + \frac{z}{z_0})^4} \right), \quad (2.39)$$

where  $z_0$  determines the width of the well and is a characteristic of the semiconductor material. Choosing a value of  $E_F$ , Schrödinger's equation is solved for the energy eigenvalues. From this, then, the surface number density is calculated, for electrons in the InAs and holes in the GaSb. The procedure is repeated with various values of  $E_F$  until a value is found for which charge neutrality is satisfied.

## D. Magnetic Field

### 1. Normal Magnetic Field

Electric subbands correspond to motion quantized in the direction normal to the plane of the semiconductor surface, but the charge carriers in the space charge layer have free-electron like motion in the plane. A magnetic field applied normal to the surface,  $\vec{H} = (0, 0, H)$ , quantizes the motion further, corresponding (classically) to cyclotron orbits with harmonic oscillator energies. Using the Landau gauge  $\vec{A} = (0, Hx, 0)$ , and neglecting complications such as electron-electron interactions, the Schrödinger equation for a particle of charge  $-e$  is

$$\left[ \frac{1}{2m^*} \left( \hat{p} + \frac{e\vec{A}}{c} \right)^2 + V(z) \right] \Psi = E\Psi, \quad (2.40)$$

and can be written

$$\left[ \frac{1}{2m^*} (\hat{p}_x^2 + \hat{p}_y^2 + \hat{p}_z^2) + \frac{e^2 H^2 x^2}{2m^* c^2} + \frac{eH\hat{p}_y x}{m^* c} + V(z) \right] \Psi = E\Psi. \quad (2.41)$$

If product wave functions  $\Psi = \psi(z)\Phi(x)e^{-ik_y y}$  are assumed, then Schrödinger's equation reduces to the two equations

$$\frac{1}{2m^*} \left[ \hat{p}_x^2 + \left( \hbar k_y + \frac{eHx}{c} \right)^2 \right] \Phi(x) = E_{\parallel} \Phi(x), \quad (2.42)$$

$$\left[ \frac{\hat{p}_z^2}{2m^*} + V(z) \right] \psi(z) = E_{\perp} \psi(z), \quad (2.43)$$

with the total energy  $E = E_{\perp} + E_{\parallel}$ . In the first of these two equations, the effective potential  $(\hbar k_y + \frac{eHx}{c})^2$  is that of a harmonic oscillator, where



the cyclotron orbit center  $x_0$  is found at the potential minimum as

$$\left. \frac{\partial}{\partial x} (\hbar k_y + \frac{eHx}{c})^2 \right|_{x=x_0} = 0,$$

or,

$$x_0 = -\frac{c\hbar k_y}{eH}. \quad (2.44)$$

The Schrödinger equation, then, is in the form of a one-dimensional harmonic oscillator equation

$$\left[ \frac{\hat{p}_x^2}{2m^*} + \frac{m^* \omega_c^2}{2} (x - x_0)^2 \right] \Phi(x) = E_{\parallel} \Phi(x), \quad (2.45)$$

where  $\omega_c = \frac{eH}{m^*c}$  is the cyclotron frequency. The energy eigenvalues are called Landau levels, and are given by

$$E_{\parallel} = (j + \frac{1}{2})\hbar\omega_c. \quad j = 0, 1, 2, \dots \quad (2.46)$$

The second of the two Schrödinger equations is the same equation which applies if there is no magnetic field, and has eigenvalues  $E_{\perp} = E_i$ . so the total energy in the presence of a perpendicular magnetic field is

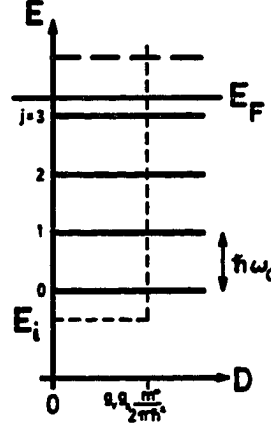
$$E = E_i + (j + \frac{1}{2})\hbar\omega_c. \quad i, j = 0, 1, 2, \dots \quad (2.47)$$

The charge carriers in each subband  $i$  condense onto delta-function like Landau levels  $j$  separated by an energy  $\hbar\omega_c$ , as seen for one subband in Figure 7. The number of states  $N_L$  in each Landau level is

$$N_L = D(E)\hbar\omega_c = \frac{g_v g_s eH}{2\pi\hbar c}. \quad (2.48)$$

Scattering from impurities, surface states, surface roughness, for example, has the effect of broadening the delta-function Landau level energies.<sup>37,38</sup> In this case, the Landau levels may consist of localized states in the Landau level tails (which do not contribute to the current in the space charge layer), and current carrying extended states in the center of the Landau levels. The quantum Hall effect is a result of pinning the Fermi level in the localized states in the Landau level tails.<sup>39</sup>

Figure 7. Landau Levels. With a magnetic field  $H$  normal to the space charge layer, the carriers in the electric subband condense onto a ladder of delta-function Landau levels (index  $j$ ) below the Fermi level  $E_F$ . The Landau levels are separated by an energy  $\hbar\omega_c$ , and have energies  $E_i + (j + \frac{1}{2})\hbar\omega_c$ . The number of states in each Landau level is  $\frac{2\pi g_s e H}{2\pi \hbar c}$ .



## 2. Parallel Magnetic Field

A magnetic field in the plane of the space charge layer exerts on the charge carriers a Lorentz force normal to the plane. For an ideal 2DEG, the charge carriers are confined to the plane. However, for a quasi-2DEG, the wavefunctions of the charge carriers extend into the semiconductor, and the charge carriers undergo cyclotron orbits. The parallel magnetic field can be treated as a perturbation<sup>36</sup> if the cyclotron orbit diameter is large compared to the width of the potential well, i.e., if  $2R_c \gg z_i$ . The cyclotron orbit radius,  $R_c = \sqrt{2(i + \frac{1}{2})\hbar c / eH}$ , is independent of material constants. In the lowest Landau level ( $i = 0$ ), and for large magnetic fields,

say  $H = 10T$ , the cyclotron diameter is about  $160 \text{ \AA}$ . In the triangular well approximation, the width of the well at the energy  $E_i$  is  $z_i = \frac{E_i}{eF}$ . Some appropriate values of  $E_i$  and  $z_i$  for accumulation on  $n\text{-InAs}$  are listed in Table I, and in the ground state ( $i = 0$ ) and at small gate bias  $(V_G - V_T) = 1V$ , the width of the potential well is about  $180 \text{ \AA}$ . Thus, the perturbation approach is valid at large gate voltages and small magnetic fields.

In this perturbation approach, the energy of the  $i^{\text{th}}$  electric subband is increased by an amount<sup>36</sup>

$$\Delta E_i = \frac{e^2 H^2}{2m^* c^2} [\langle z^2 \rangle - \langle z \rangle^2], \quad (2.49)$$

where the angle brackets refer to expectation values. Another test of the validity of the perturbation approach is that this diamagnetic energy shift must be small compared to the energy spacing between electric subband minima. The spread of the wavefunction is about half the width of the well, i.e.,

$$z_i \simeq 2 \left[ \langle z^2 \rangle - \langle z \rangle^2 \right]^{\frac{1}{2}}. \quad (2.50)$$

The width can be estimated in the triangular approximation in order to estimate  $\Delta E_i$ . For the ground state at  $H = 1T$ , and  $(V_G - V_T) = 1V$ ,  $\Delta E_0 \simeq 0.3 \text{ meV}$ , and the separation between the ground state and first excited state is about  $44 \text{ meV}$  (for  $H = 0$ ). Figure 11 of reference 24 gives a value of  $\sim 10 \text{ meV}$ .

If the magnetic field is applied along the  $y$ -direction, then  $\vec{H} = (0, H, 0)$  and the cyclotron orbits are in the  $y = \text{constant}$  plane. With the

TABLE I

Triangular Well Approximation for n-InAs,  
Sample 31-A2( $10^{15}$ )

$i$	$^a E_i$ (meV)	$^a z_i$ (Å)	$^b 2R_c$ (Å)	$^c \Delta E_i$ (meV)
0	231	93	512	0.082
1	407	163	887	0.25
2	550	220	1146	0.46
3	677	271	1356	0.70

<sup>a</sup>Calculated from equations 2.36 and 2.35 for  $V_G - V_T = +9.6V$ , corresponding to  $N_s = 1.5 \times 10^{12} \text{ cm}^{-2}$  (see Table IV).

<sup>b</sup>For  $H = 1T$ .

<sup>c</sup>Calculated from equation 2.49, for the given values of  $z_i$  and  $H = 1T$ .

gauge  $\vec{A} = (Hz, 0, 0)$ , the Schrödinger equation is

$$\left[ \frac{1}{2m^*} \left( \hat{p}_x + \frac{eHz}{c} \right)^2 + \frac{\hat{p}_y^2}{2m^*} + \frac{\hat{p}_z^2}{2m^*} + V(z) \right] \Psi = E\Psi \quad (2.51)$$

The momentum operator  $\hat{p}_y$  is separable, and with the product wavefunctions

$$\psi = \psi(z)e^{i\vec{k} \cdot \vec{r}} \quad (2.52)$$

corresponds to Bloch waves in the  $y$ -direction with momentum  $\hbar k_y$ . Schrödinger's equation, then, reduces to

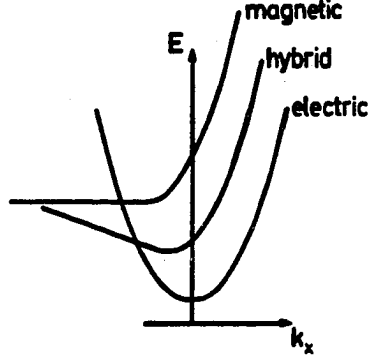
$$\left[ \frac{1}{2m^*} \left( \hbar k_x + \frac{eHz}{c} \right)^2 + \frac{\hat{p}_z^2}{2m^*} + V(z) \right] \psi(z)e^{i\vec{k} \cdot \vec{r}} = E_i(k_x)\psi(z)e^{i\vec{k} \cdot \vec{r}}, \quad (2.53)$$

with eigenvalues  $E_i(k_x)$  and total energy

$$E = E_i(k_x) + \frac{\hbar^2 k_y^2}{2m^*}. \quad (2.54)$$

The dispersion relation has been calculated self-consistently for accumulation on  $n$ -Si, and the ground state results are in good agreement with the perturbation theory, even with a large magnetic field.<sup>31</sup> In the triangular approximation, transcendental solutions for  $E_i(k_x)$  have been found.<sup>40</sup> Hybrid subbands result in the case of crossed electric and magnetic fields of comparable strength, as seen in Figure 8. In this case, and in the magnetic limit (large  $H$ ) the subband minima are diamagnetically shifted up in energy and over in  $k_x$  relative to the electric subband minima. The density of states increases with parallel field.<sup>70</sup>

Figure 8. Dispersion Relations. For an electric subband the dispersion relation is parabolic (see Figure 6). The dispersion relation for crossed electric and magnetic fields of comparable strength is a distorted parabola and the minimum is shifted up in energy and over in  $k_x$ . In the (parallel) magnetic limit, the dispersion relation is further shifted.



### 3. Tipped Magnetic Field

In the general case that the applied magnetic field is incident at some angle to the plane of the surface space charge layer,<sup>36,83</sup> the field can be restricted to the  $x = 0$  plane without loss of generality and can be written

$$\mathbf{H} = (0, H_{\parallel}, H_{\perp}), \quad (2.55)$$

where  $H_{\parallel} = H \sin \theta$ ,  $H_{\perp} = H \cos \theta$ , and the angle  $\theta$  is measured from the surface normal. Using the gauge  $\vec{A} = (zH_{\parallel}, xH_{\perp}, 0)$ , the Hamiltonian is

$$\mathcal{H} = \frac{1}{2m^*} \left[ \hat{p}^2 + \frac{e\vec{A}}{c} \right] + V(z) \quad (2.56)$$

$$= \frac{1}{2m^*} \left[ \hat{p}_x^2 + \hat{p}_y^2 + \hat{p}_z^2 + \frac{2e}{c} (p_x A_x + p_y A_y) + \frac{e^2}{c^2} (A_x^2 + A_y^2) \right] + V(z). \quad (2.57)$$

With product wavefunctions, the operator  $\hat{p}_y$  is separable and corresponds to the energy  $\frac{\hbar^2 k_y^2}{2m^*}$ ; the Hamiltonian becomes

$$\mathcal{H} = \frac{1}{2m^*} \left[ \hat{p}_x^2 + \hat{p}_z^2 + \frac{2eH}{c} (p_x z \sin \theta + \hbar k_y x \cos \theta) + \frac{e^2 H^2}{c^2} (z^2 \sin^2 \theta + x^2 \cos^2 \theta) \right] + V(z) + \frac{\hbar^2 k_y^2}{2m^*}. \quad (2.58)$$

In the limits  $\theta = 0^\circ$  and  $\theta = 90^\circ$ , this Hamiltonian reduces to the expressions found above for the normal and parallel field cases.

### E. Accumulation on InAs

#### 1. Bulk Properties of InAs

Indium arsenide is a high mobility, small band gap III—V compound semiconductor. The lattice is the zinc-blende structure,<sup>41</sup> which can be thought of as two interpenetrating face-centered-cubic sublattices. The four nearest neighbors of each atom are of the other type and sit at the corners of a tetrahedron; the nearest neighbor distance is  $\frac{\sqrt{3}}{4}a$ , where  $a = 6.06 \text{ \AA}$  [reference 42] is the lattice constant of the fcc sublattice. At room temperature the direct<sup>43,44</sup> band gap  $E_G = 0.36 \text{ eV}$  [reference 45] is about one-third of the band gap of silicon.

The room temperature mobility is about  $30,000 \text{ cm}^2/\text{Vs}$  [reference 47], which is about 20 times greater than that of Si. The mobility is determined, in part, by the effective mass of the electrons. At the conduction band minimum the InAs electron effective mass is  $0.023 m_e$  [reference 48]. The single conduction band valley ( $g_v=1$ ) is isotropic<sup>41</sup> but not parabolic<sup>49</sup> in InAs. The isotropy leads to a spherical constant energy surface and the nonparabolicity leads to an effective mass dependence on energy. In contrast, Si has an anisotropic electron effective mass,<sup>3</sup> so the mobility (and hence conductivity) depends on the crystal orientation. Furthermore, the valley degeneracy in Si can be greater than one.<sup>36</sup> This degeneracy can be lifted in

high magnetic fields and observed in the conductivity.<sup>50</sup>

In high magnetic fields the conduction band separates into two bands corresponding to the two electron spins. This spin splitting can be resolved in cyclotron resonance<sup>76</sup> and magnetoabsorption<sup>53</sup> experiments on bulk InAs. The bulk  $g$ -factor in InAs is found to be  $-15.0$  [reference 53].

A 2DEG on the surface of InAs is interesting because the potential well at the surface may be as wide as several hundred Ångströms and as deep as several hundred meV,<sup>54</sup> which allows up to four subbands to be occupied.<sup>24,55</sup> Silicon, on the other hand, has a potential well typically less than 100 Å wide and less than 100 meV deep.<sup>31</sup> The width and depth of the well depends on the penetration depth of the electric field, which depends, partly, on the dielectric constant. The bulk relative static dielectric constant in InAs is 14.6 [reference 57], compared to a value of 11.9 in Si. A partial list of the bulk properties of InAs is in Appendix A.

## 2. 1971—1973

Extensive studies have been made by Tsui<sup>59,109</sup> on the accumulation layer on n-InAs in an InAs-Pb diode junction at 4.2 K. Because of the surface states at the InAs-native oxide interface, the semiconductor surface was under accumulation at zero bias voltage. Differential tunneling currents (through the thin native oxide between the InAs and Pb) proportional to the junction conductance were measured as a function of applied bias voltage. The tunneling current was proportional to the 2D density of



states of the electric subbands in the accumulation layer. The bias voltage increased the band bending and decreased the tunnel barrier height. Thus the junction bias allowed a direct measure of the subband binding energy. Two subbands were occupied in samples with bulk carrier concentration  $\leq 1.5 \times 10^{17} \text{ cm}^{-3}$ , and only one subband was seen in those samples with greater bulk carrier concentration.

With a magnetic field applied normal to the surface accumulation layer, oscillations appeared in both the conductance-*versus*-bias curves and the conductance-*versus*-magnetic field strength curves. The oscillations were associated with the ladder of Landau energy levels into which the electrons were quantized. A separate set of oscillations was observed for each bound subband and for the bulk conduction electrons. Because the bias voltage was a direct energy measurement, the period of the oscillations in bias voltage was a measure of the Landau level energy separation. From this measurement, then, a value for the electron effective mass was obtained. The effective mass was found to depend on the electron energy relative to the subband minima, which indicated the non-parabolicity of the subband dispersion. The oscillation period in inverse field strength was used to determine the number of electrons in the subbands. By tipping the magnetic field direction away from the surface normal, Tsui found that the Landau level spacing depends only on the normal component of the field.

Self-consistent calculations by Appelbaum and Baraff<sup>60</sup> for the bound state energy levels in an accumulation layer have shown that the

shape of the potential well and hence the subband energy levels depends on the magnetic field strength, which agrees qualitatively with Tsui's experimental results. However, with the magnetic field parallel to the surface accumulation layer, Tsui<sup>61</sup> measured the diamagnetic energy shift predicted by Stern and Howard.<sup>36</sup> This leads to a determination of the spread of the electron bound state wavefunction, which is essentially the accumulation layer thickness. In this case (bulk carrier concentration  $\sim 10^{17} \text{ cm}^{-3}$ ) the accumulation layer was quite narrow, about 30 Å.

### 3. 1977—1979

Wagner, Kennedy, and Wieder<sup>55</sup> measured the differential conductivity (transconductance) of an n-InAs MOSFET accumulation layer. The 14  $\mu\text{m}$  epitaxial layer of InAs was grown on a GaAs substrate and had a bulk carrier concentration of  $2 \times 10^{15} \text{ cm}^{-3}$  (at 83K). With a magnetic field normal to the accumulation layer, the transconductance (at 4.2K) was plotted against gate voltage at various field strengths. That at least three subbands were occupied was evident in the Shubnikov-de Haas oscillations in the transconductance. The subband population ( $\sim 0.5 \times 10^{12} \text{ cm}^{-2}$  for the ground state) was determined from the oscillation period in inverse field strength. Spin splitting of the transconductance oscillations was observed in the ground state subband at the highest magnetic fields (6-8T).

Similar experiments were done on similar samples by Washburn and Sites,<sup>62</sup> and Washburn, Sites, and Wieder.<sup>26</sup> Transconductance and differential Hall voltage data (at 4K) were taken at various gate voltages

and (normal) magnetic fields. Again, three subbands were occupied. The subband population was determined from the period of the Shubnikov-de Haas oscillations, resulting in a plot of subband number density-*versus*-gate voltage.

The oscillation amplitude at various temperatures (for constant magnetic field) was plotted against temperature. By adjusting the value of the electron effective mass as a parameter, a curve from an expected temperature dependence was fit to the data. The effective mass was found this way for each of the three subbands at various gate voltages. In each subband, the effective mass increased with increased population, indicating the non-parabolicity of the subband dispersion.

#### 4. 1980—1982

Reisinger and Koch<sup>63</sup> have measured the differential reflection of an n-InAs MOSFET with a bulk carrier concentration of about  $2 \times 10^{16} \text{ cm}^{-3}$ . At constant incident photon energies in the range 112-136 meV, structure in the reflectivity (at 100K) was interpreted as due to electron transitions between the ground state subband and the first excited state ( $0 \rightarrow 1$ ), and between the ground state and the second excited state ( $0 \rightarrow 2$ ). The  $0 \rightarrow 1$  transition appeared as a doublet set of minima.

Riesinger, Schaber, and Doezeema<sup>24</sup> performed cyclotron resonance and Shubnikov-de Haas effect experiments on several n-InAs MOSFET's. Four subbands were observed in the lowest bulk concentration sample ( $2 \times 10^{15} \text{ cm}^{-3}$ ). The cyclotron effective mass (at 20K) in each subband increased

as the total surface number density increased. Again, this indicates the non-parabolicity of the subband dispersion. The scattering rates (primarily from surface scattering) determined from the cyclotron resonance data also increased with increasing surface density. This is because the subbands became more tightly bound as the surface density increased. Furthermore, at constant surface density, the scattering rate was found to be higher for the lower lying subbands which were more tightly bound to the surface.

The subband population was determined from the Shubnikov-de Haas oscillations (at 4.2K). Because the Fermi level was in the conduction band, as the total surface density increased the subband population made a discontinuous change from zero to a finite value (dependent only on the bulk carrier concentration) at occupation threshold. This effect was more pronounced in the samples with higher bulk carrier concentration ( $2.0 \times 10^{16} - 1.0 \times 10^{17} \text{ cm}^{-2}$ ) because these samples were more highly degenerate.

Taking into account the energy dependence of the effective mass, an expression for the number density of each subband was given in terms of the subband binding energy. Of course, the binding energy was dependent on the total surface density. This resulted in a plot of subband binding energies, measured from the bulk conduction band edge, *versus* total surface density for the three lowest subbands in four samples. At the highest surface densities ( $\sim 6 \times 10^{12} \text{ cm}^{-2}$ ), the ground state binding energy was about 200 meV; the first excited state energy was about 75 meV; and the second excited state energy was about 25 meV.

## CHAPTER III

### EXPERIMENTAL APPARATUS

Magnetotransport measurements are made of the surface accumulation layer on n-type InAs at low temperatures. Although the transconductance is the property of primary interest, the differential resistance and capacitance also are used to probe the samples. The measurements are made as a function of 2D number density of electrons (gate voltage), magnetic field strength and direction, and sample temperature. The apparatus used in this experiment can be divided into three major parts: the cryostat, the control and measuring electronics, and the samples.

#### A. Cryostat

The cryostat, shown in Figure 9, consists of two dewars and a sample holder. The outer dewar holds the magnet and the liquid helium bath, and the inner dewar holds the sample. The inner dewar is used to isolate the sample from the liquid helium bath, yet keep the sample in thermal contact with the bath for measurements at 4.2 K. For this purpose, the inner dewar and its jacket are filled with helium exchange gas.

A liquid nitrogen jacket around the outer dewar is unnecessary because of the superinsulation in the outer dewar jacket, although the

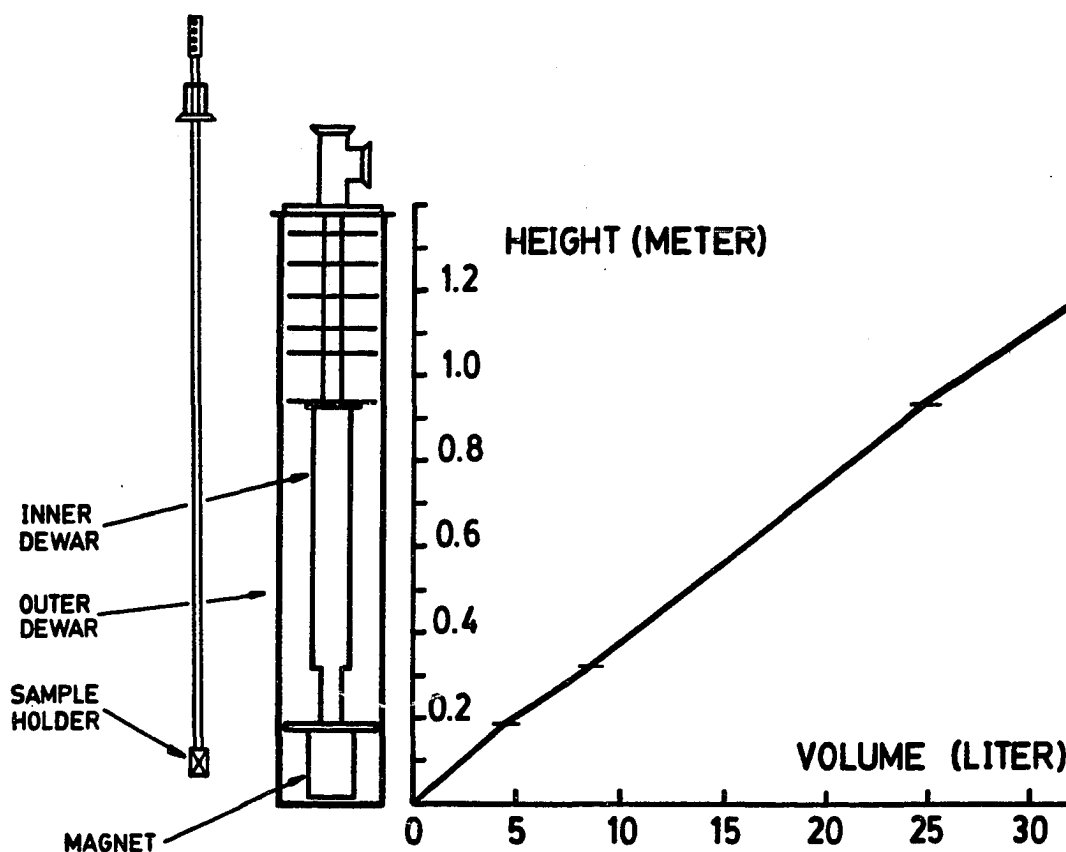


**Figure 9. Cryostat.** The sample holder is inserted into the magnet through the top port of the inner dewar. The inner dewar and its vacuum jacket are filled with helium exchange gas for thermal contact between the sample and the liquid helium bath in the outer dewar. The graph gives the volume of the helium liquid as a function of height above the bottom of the outer dewar. Typically about 20 liters of helium are collected for each experimental run. Since it takes about five liters to cover the magnet, this allows about 30 hours running time.

cryostat is precooled with liquid nitrogen before a liquid helium transfer. The magnet is a superconducting NbTi solenoid, which is suspended by three fiberglass rods from a stainless steel flange at the top of the outer dewar. When the magnet is energized the cryostat is vented through the power supply leads to reduce the heating of the helium bath by the resistance heating of the leads. The volume of liquid in the outer dewar as a function of depth is shown in Figure 9. During the liquid helium transfer about ten liters of liquid helium are required to cool the cryostat (primarily the magnet) from 77 K to 4.2 K; the magnet occupies a volume of about one liter. For comparison, about the same amount of liquid helium is required to cool one liter of liquid nitrogen from 77 K to 63 K and solidify it. This means that great care must be taken to remove all of the liquid nitrogen after precooling the cryostat. The helium loss rate with the magnet on is about 0.5 liter per hour, and about 0.4 liter per hour with the magnet off.

Calibration of the magnet by nuclear magnetic resonance of Al has shown that the current in the magnet produces a field of 0.11190 Tesla per Ampere, assumed constant for all currents. The magnet power supply provides a voltage proportional to the current, from which all field measurements are taken, with a conversion factor of 0.0854 T/mV. The maximum field strength before quenching at 4.2 K is 7.9 T. The error in the field strength measurements is estimated to be less than 0.1%.

The sample is mounted in a holder which allows rotation of the sample in the magnetic field. The angle,  $\theta$ , is measured from the surface

normal. The rotation is controlled by a stepping motor as shown in Figure 10. The sample is mounted on the shaft of a pinion which meshes with a worm gear. The worm gear is then driven by the stepping motor, at a rate of 990 steps per degree of rotation. For data taken at a fixed angle, the number of steps is taken as a measure of the angle. For data taken as the angle is swept through 90 degrees, two methods are used to drive the X-Y plotter and hence measure the angle. Sweeping the angle at a constant rate allows the use of a time base sweep of the plotter. The sweep rates (typically about three minutes per 90 degrees of rotation) of the motor and time base must be synchronized. Slipping of the clutch must be avoided since the time base would not stop. Another method used to measure the angle while the sample is rotating is shown in Figure 10. The ten turn potentiometer is driven (below the clutch) by the shaft which turns the worm gear. The voltage at the center wiper of the potentiometer then drives the X-Y plotter.

Prior to insertion of the sample holder into the cryostat, the normal to the sample surface is aligned by eye with the axis of the sample holder (the field direction). After cooling the sample to liquid helium temperature, data is taken at symmetric positive and negative angles in order to find the zero angle. Error in the angle measurements is about  $\pm 1$  degree.

### B. Circuit Analysis

Transconductance is measured in samples with a large ( $> 100\Omega$ ) source/drain resistance  $R_{SD}$ . In order to make this measurement the cir-



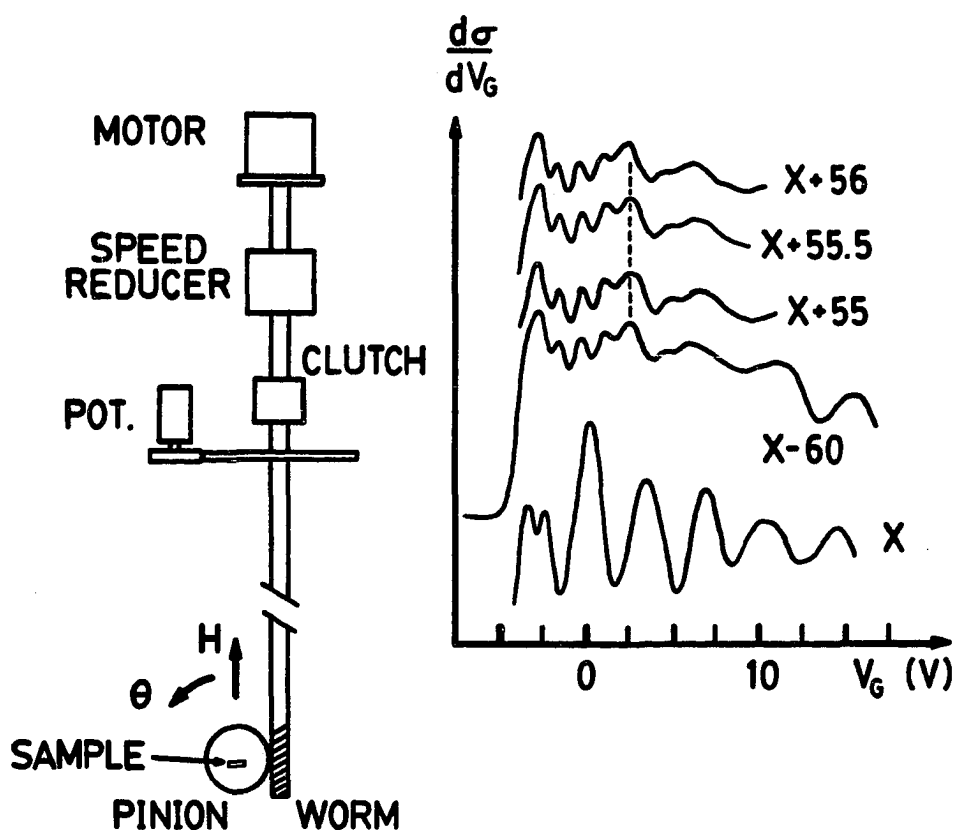


Figure 10. Sample Rotation Mechanism. The sample is mounted on the shaft of the pinion which meshes with the worm gear. The clutch is used to prevent breakage of the gears in case the gears freeze. Below the clutch is a gear which drives a potentiometer. The voltage at the center wiper of the potentiometer is proportional to the angle of rotation. The trace labeled  $X$  was taken at the sample orientation as inserted into the magnet. Then a trace was taken at  $X - 60^\circ$  (negative direction arbitrarily chosen). Traces were taken at various positive angles until a close match of the peak position was found (illustrated by the dashed line). In this case the  $X + 55.5^\circ$  trace matched, and this gave  $X = +2.25^\circ$ .

cuit in Figure 11a is used with a small series resistance  $R$ . The source/drain current is

$$i_{SD} = \frac{V_{SD}}{R + R_{SD}} = \frac{V}{R}, \quad (3.1)$$

where  $V$  is the voltage drop across the series resistor. Now in this case,  $R_{SD}/R \gg 1$  so that

$$\begin{aligned} V &= \frac{V_{SD}}{1 + \frac{R_{SD}}{R}} \\ &\simeq \frac{RV_{SD}}{R_{SD}} \propto RV_{SD} \sigma, \end{aligned} \quad (3.2)$$

where  $\sigma$  is the sample sheet conductivity. Because the source/drain resistance is inversely proportional to the conductivity, the voltage drop across the series resistor is proportional to the sample conductivity (provided that the geometrical factors remain constant). For samples with a small ( $< 10\Omega$ ) source/drain resistance, the differential resistivity is measured. A similar analysis of the circuit of Figure 11a in the alternate configuration ( $R/R_{SD} \gg 1$ ) gives the result

$$V \simeq \frac{V_{SD}R_{SD}}{R} \propto \frac{V_{SD}}{R} \rho, \quad (3.3)$$

where, now,  $V$  is the voltage drop across the sample.

The sheet conductivity (or resistivity) is a function of the gate voltage and magnetic field, and it remains only to take the derivative of the voltage  $V$  with respect to the gate voltage with the lock-in amplifier to obtain the transconductance  $\frac{d\sigma}{dV_g}$  (or  $\frac{d\rho}{dV_g}$ ). The bulk transverse magnetoresistance of one of the samples is shown in Figure 12.

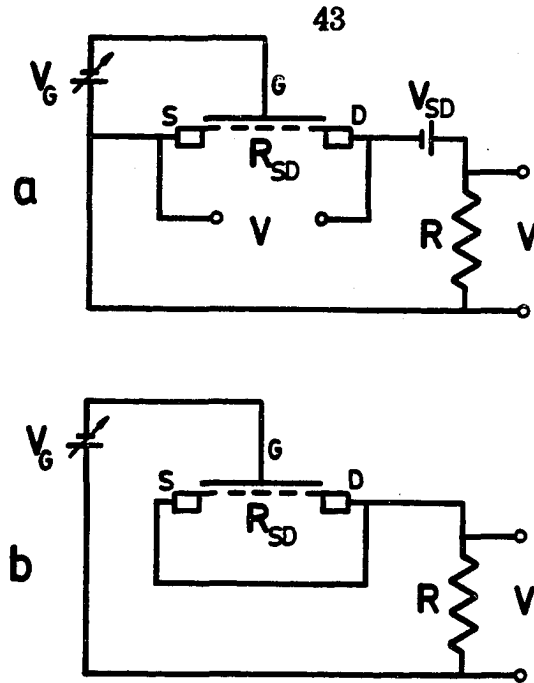


Figure 11. Schematic Circuit. (a) The variable DC gate voltage is AC modulated in this general circuit for measuring  $\frac{dI}{dV_G}$  or  $\frac{d\rho}{dV_G}$ .  $V_{SD}$  is kept constant in both measurements. See the text for a discussion on the lock-in amplifier input voltage  $V$  and the value of the series resistance  $R$ . (b) The source and drain are shorted in the capacitance measurement. The frequency of the gate modulation is the measurement frequency  $f$ .

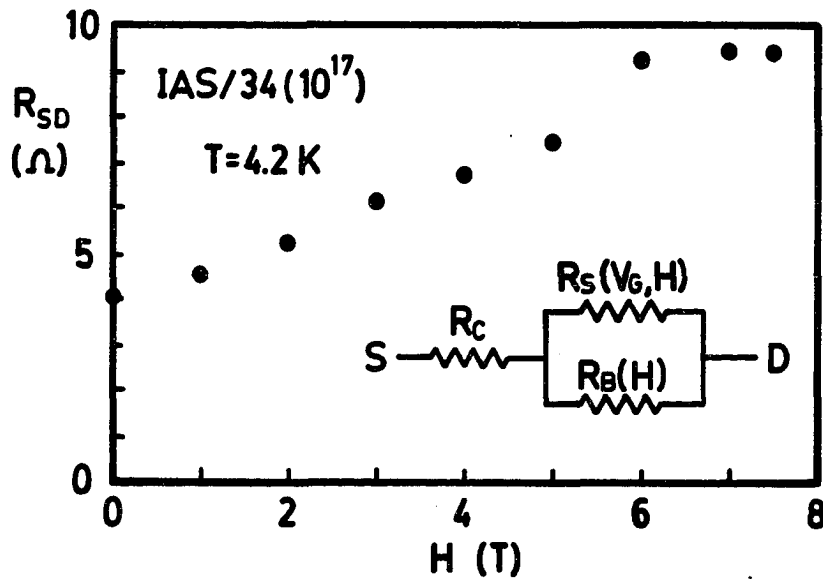
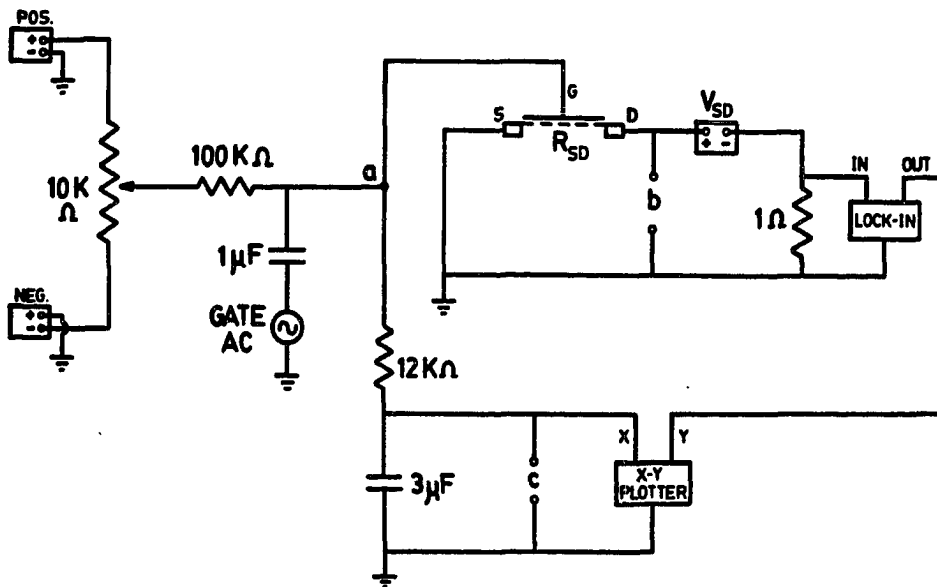


Figure 12. Bulk Magnetoresistance. The surface layer resistance  $R_S$  is in parallel with the bulk resistance  $R_B$ . This parallel combination is in series with any contact resistance  $R_C$ . The bulk resistance is not a function of gate voltage. The source/drain resistance plotted here as a function of perpendicular magnetic field strength was taken with an ohm meter while the gate was left floating.

A complete circuit for transconductance measurements as a function of gate voltage is shown in Figure 13. Two DC power supplies provide a variable gate voltage ( $-25V \leq V_G \leq +25V$ ), which also drive the X-axis of the X-Y plotter. The gate AC modulation (200 Hertz) is provided by the lock-in amplifier reference oscillator. The amplitude of the lock-in output is proportional to the gate AC modulation amplitude (typically about  $0.5 V_{pp}$ ). The source/drain current is kept low ( $\sim 1 \text{ mA}$ ) to avoid heating the sample.



**Figure 13. Complete Circuit for Transconductance-versus-Gate Voltage.** Two DC power supplies are connected in opposition across the motor driven  $10 \text{ k}\Omega$  ten-turn potentiometer to provide the variable gate voltage ( $-25V \leq V_G \leq +25V$ ). The lock-in reference oscillator, which is protected from the DC supplies by the  $1 \mu\text{F}$  capacitor, provides the AC gate modulation. The  $100 \text{ k}\Omega$  resistor prevents any appreciable DC current in the gate circuit. The  $12 \text{ k}\Omega/3 \mu\text{F}$  filter blocks the gate AC modulation from the X-Y plotter. The modulation amplitude is measured at point a. Monitoring the gate DC level at point c leads to a slight error, since there is a small DC voltage drop across the  $12 \text{ k}\Omega$  resistor. The source/drain current is monitored at point b. The voltage drop across the  $1 \Omega$  series resistor is the input to the lock-in amplifier; the output is proportional to the sample transconductance and drives the Y-axis of the plotter.

The MOS device capacitance  $C$  is measured with the source and drain shorted as in Figure 11b. If the series resistance  $R$  is small compared to the device capacitance reactance  $X_c$ , then the voltage drop across  $R$  is

$$V \simeq 2\pi f C V_G, \quad (3.4)$$

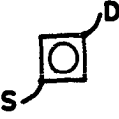

where  $f$  is the gate voltage modulation frequency. The lock-in amplifier takes the derivative of the voltage with respect to the gate voltage, so the lock-in output is proportional to  $C$ .

### C. Sample Preparation

Two samples of n-type InAs are used, one of them, sample number 31-A2( $10^{15}$ ), is an  $n = 2 \times 10^{15} \text{ cm}^{-3}$  epitaxial layer, and the other is sample number IAS632P5S1Q1/34, with  $n = 1.4 \times 10^{17} \text{ cm}^{-3}$ . This latter sample will be referred to hereafter as sample IAS/34( $10^{17}$ ). Both samples have been described elsewhere.<sup>56</sup> Sample 31-A2( $10^{15}$ ) was received with electrical connections, but sample IAS/34( $10^{17}$ ) required attachment of gate and source/drain electrodes. (The insulating layer and gate metal are considered here as part of the sample.) A few characteristics of the samples are listed in Table II.

Sample IAS/34( $10^{17}$ ) came stuck in beeswax on an aluminum block. A hot plate is used to melt the beeswax ( $\sim 55^\circ\text{C}$ ). To remove the beeswax the sample is placed on filter paper in a bath of hot trichloroethylene ( $\sim 90^\circ\text{C}$ ), as in Figure 14. Next, the sample is put in a second bath of trichloroethylene for a moment, then lifted out of the liquid, but held to dry

**TABLE II**  
**Sample Properties<sup>a</sup>**

	31-A2( $10^{15}$ )	IAS/34( $10^{17}$ )	
Bulk electron density	$2.0 \times 10^{15}$ (83K)	$1.4 \times 10^{17}$	$\text{cm}^{-3}$
$E_B = E_C - E_F^b$	-2.5	-42	meV
Gate			
area	3	3	$\text{mm}^2$
material	Ni	NiCr	
capacitance <sup>c</sup>			
300K	1.26	1.03	nF
4.2K	1.02	0.702	
Source/drain resistance <sup>d</sup>			
300K	133	9.4	$\Omega$
4.2K	179	2.7	
Insulating layer thickness	1000	2000	$\text{\AA}$
Sample			
thickness	10 — 15 $\mu\text{m}$ (epilayer)	0.5mm (bulk)	
area	10	10	$\text{mm}^2$
crystal orientation	(100)	(111)	
Source/drain geometry	corners	sides	
			

<sup>a</sup>See reference 56

<sup>b</sup>Calculated from bulk density of states

<sup>c</sup>Includes  $\sim 0.1$  nF lead capacitance

<sup>d</sup>Includes  $\sim 3\Omega$  lead resistance

with the gate exposed over the trichloroethylene vapor. This removes any residual film, leaving a clean gate. This last step is most important. After the sample is cleaned, electrical connections are made.

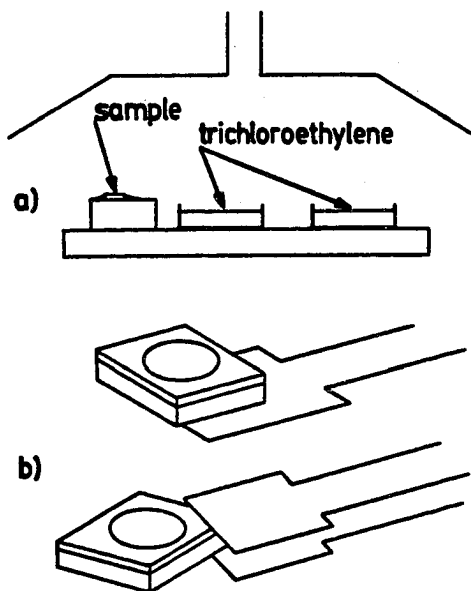


Figure 14. Cleaning the Sample. (a) The sample is imbedded in beeswax on an aluminum block for protection. The beeswax is melted by placing the block on a hotplate. The beeswax is cleaned from the sample by placing the sample in the baths of boiling trichloroethylene. After the sample is removed from the second bath, it is held to dry with the gate upside down over the trichloroethylene vapor. This process must be done under a vent hood. (b) Two methods of safely handling the sample with tweezers. Care must be taken not to touch the gate area.

The source/drain connections of this sample are made on the bottom of the sample with pure indium used as solder, without flux. A thick layer of indium is evaporated along two edges of the sample. This is shown in Figure 15. After evaporation, the sample is placed in an oven (bottom side down on a piece of quartz) and annealed at 140C for about 20 - 30 minutes, in order that the indium diffuse through the oxide layer which covers the InAs.

The sample is mounted on the copper-clad fiberglass disk ( $\frac{1}{2}$ " dia.) shown in Figure 15. The copper is etched away except for two pads which are tinned with indium. The sample is set onto the pads and pressed gently on the corners with the edges of toothpicks while a soldering iron melts the indium solder. The source/drain resistance is measured to determine whether the connections are made. After the connections are properly made, a drop of varnish is put on the sample's edge to hold the sample on the disk.

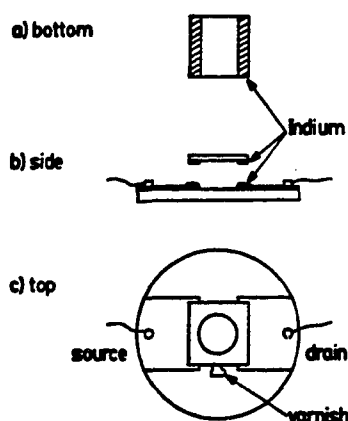


Figure 15. Source/Drain Connections. (a) The bottom of the sample is shown with two strips of evaporated indium. (b) The thickness of the evaporated indium layer is slightly exaggerated. The copper pads on the fiberglass disk have been tinned with indium and the sample is set onto the pads. (c) A soldering iron just hot enough to melt the indium is touched to the pads, making the solder connections; the sample is then glued to the disk with a drop of varnish.

Connection to the gate, made with a small wire epoxied to the gate, is difficult because of the delicacy of the insulating layer. Too much force exerted on the gate may punch through the insulating layer, yet the connection may become open if not enough force is exerted by the wire.



A 2 mil diameter annealed (hard) BeCu wire is soldered onto a small piece of copper-clad fiberglass board, and bent into a spring, which is shown in Figure 16. For connection to the external circuit, another wire is soldered to the board. This board is then glued with varnish to a small Vespel post. The arrangement just before making connection is shown in the figure. This post is held with tweezers so that the BeCu spring is poised above the gate; a small drop of conducting epoxy is put on the saddle point of the spring and a small drop of varnish is put on the bottom of the Vespel post. The sample is raised (or the spring-post assembly lowered) so that the spring makes contact with the gate and the post is glued to the fiberglass disk. The capacitance of the sample is checked to insure connection.

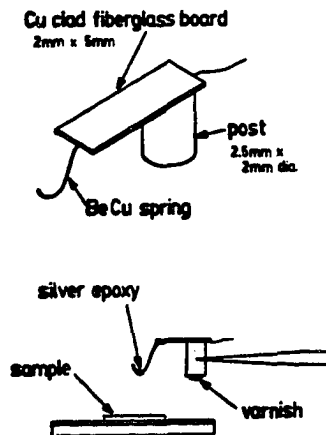


Figure 16. Gate Connection. The BeCu spring is bent so that it exerts a slight force on the gate, and glued with the conducting epoxy. The varnish holds the post in place on the fiberglass disk of Figure 15.

#### D. Temperature

Carbon resistors are used as thermometers to measure the tem-

perature of the samples, and a standard AC Wheatstone bridge technique is used to measure their resistance. Thermometer calibration is performed at three known temperatures in liquid hydrogen and liquid helium. The relative precision of a single temperature measurement is about 0.5%. However, because of thermal gradients across the sample holder, the sample temperature is not known to such high precision.

The thermometers are commercially available 1/4 Watt Allen-Bradley carbon composition electrical resistors. The nominal room temperature resistances for three thermometers are listed in Table III. To insure better thermal contact with the carbon, most of the insulation is filed off, although enough of the insulation is left on to provide strength against breakage in handling. The exposed resistors are then wrapped in cigarette paper and electrically insulated with varnish. They are then wrapped in copper foil, with a small tab left for attaching to the sample holder. An identifying number is tooled into each of the copper tabs. In order to use the resistors as thermometers, the resistance  $R$  is measured, and the temperature  $T$  is given by<sup>65</sup>

$$T = \frac{1}{\frac{A}{\ln R} + B + C \ln R}. \quad (3.5)$$

The three constants  $A$ ,  $B$ , and  $C$  are found for each resistor and are listed in Table III.

A Wheatstone bridge with an AC null detection technique is used to measure the resistance of the thermometers. This circuit is shown in Figure 17. In order to cancel the lead resistance, the measurements are

made using a three lead connection to each resistor, as shown in the figure. (Although for three resistors, a total of five lead wires are needed.) The decade resistance box covers the resistance range up to 20K  $\Omega$ .

To avoid self-heating, the power dissipated by each thermometer should be less than about  $10^{-6}$  Watt,<sup>65</sup> which means that the voltage drop across the thermometer should be less than about 10 mV<sub>pp</sub>. All resistance measurements are made at a frequency of 2 KHz. After the frequency and amplitude of the oscillator are set, the filter of the null detector is tuned to the oscillator frequency. Once this is done, the thermometer resistance can be measured by varying the resistance of the decade box. At balance the

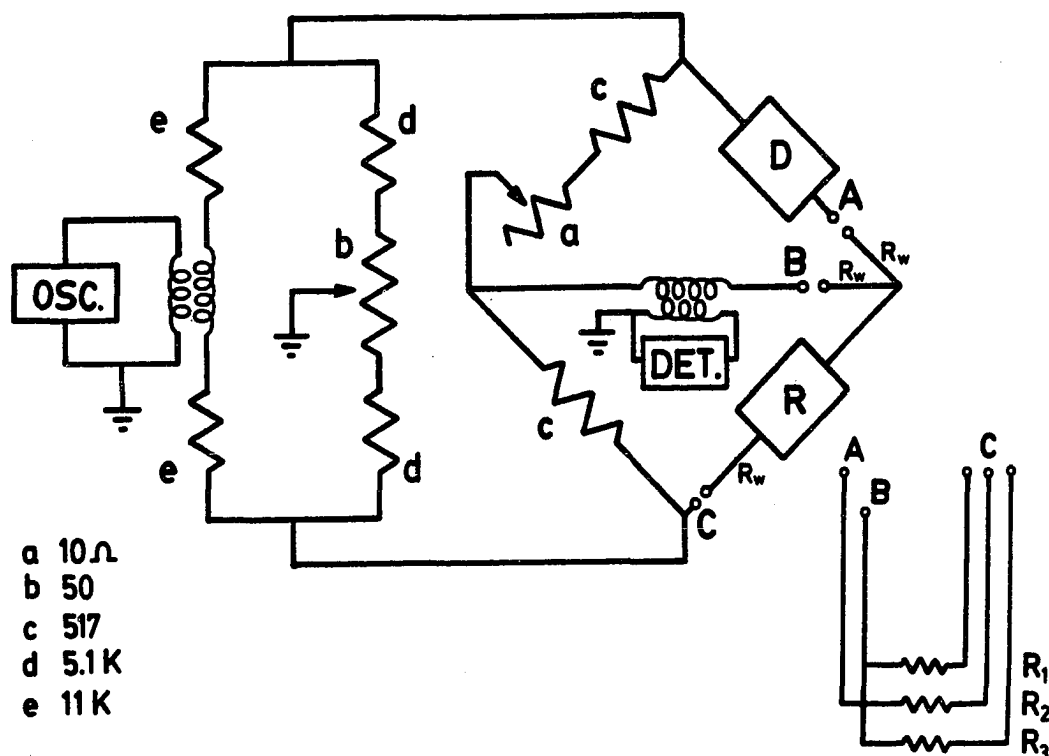


Figure 17. Wheatstone Bridge. This circuit is used to measure the resistance  $R$  of the three thermometers,  $R_1$ ,  $R_2$ , and  $R_3$ .  $D$  is the decade resistance box which balances the right side of the bridge.  $R_w$  is the resistance of each lead wire,  $\sim 3\Omega$ . To avoid measuring the lead resistance, the three lead technique is employed. The measurement frequency is 2 kHz. The voltage drop across  $R$  is kept low, less than about 10 mV<sub>pp</sub>, to avoid self-heating.

**TABLE III**  
**Thermometer Calibration**

	Nominal Resistance $\Omega$ (300K)	Measured Resistance $\Omega$	Measured Temperature K	Constants		
				A	B	C
$R_1$	125	297.78	20.174 <sup>a</sup>	2.916	-1.413	0.1668
		393.52	13.854 <sup>b</sup>			
		2006.	4.1787 <sup>c</sup>			
$R_2$	220	535.87	20.174	3.055	-1.414	0.1556
		707.3	13.854			
		5750.	3.5032			
$R_3$	220	541.68	20.174	3.081	-1.424	0.1564
		714.	13.854			
		5750.	3.5032			

<sup>a</sup>H<sub>2</sub> boiling point<sup>b</sup>H<sub>2</sub> triple point<sup>c</sup>He boiling point

decade box and the thermometer have the same resistance value, which is indicated on the decade box.

The apparatus used to immerse the thermometers in liquid hydrogen and liquid helium for calibration is a set of glass dewars with a cold finger in the inner dewar. The resistors are placed at the bottom of the inner dewar (not in thermal contact with the cold finger) and the outer dewar is filled with liquid nitrogen. To collect liquid hydrogen, the inner dewar is first filled with about one atmosphere of hydrogen gas (at 77K). Then, as liquid helium (at 4.2K) is blown into the cold finger, the hydrogen gas condenses into liquid (at 20K). More liquid is obtained by slowly bleeding in hydrogen gas from the storage bottle through a beach ball. A mercury manometer measures the vapor pressure above the liquid hydrogen. The temperature is then obtained from a vapor pressure-temperature table.<sup>66</sup> Data is taken at the  $H_2$  boiling point and the  $H_2$  triple point.

In order to take data at helium temperatures, the hydrogen is removed and liquid helium is collected in the inner dewar. Here again, the vapor pressure is measured, and the temperature is found from a vapor pressure-temperature table.<sup>67</sup> The results of this calibration for three thermometers are listed in Table III.

The precision of a single measured resistance value is about 0.5% which corresponds to a temperature measurement of roughly the same precision. Furthermore, during an experimental run, with three ther-

mometers at thermal equilibrium with the liquid helium bath, the temperature measured by each thermometer is the same to within that same relative precision. However, the uncertainty in the knowledge of the sample temperature is greater than that precision at temperatures above 4.2K. Because of thermal gradients across the sample holder, the temperature at the thermometer is not necessarily the temperature of the sample.

A resistance heater is used to raise the temperature above 4.2K. A 100  $\Omega$  (at 4.2K) length of silk insulated 40 gauge manganin resistance wire is wound non-inductively and varnished to the sample holder. Heat is conducted (not very efficiently, it seems) from the heater to the sample by the helium exchange gas in the inner dewar. The exchange gas in the inner dewar jacket is not removed, so the heater is in thermal contact with the liquid helium bath. Because of the geometry of the sample holder and the position of the heater, a large thermal gradient (as much as 10 K/inch) appears across the sample holder. This gradient depends on the exchange gas pressure as well as the position of the heater on the sample holder. Various positions of the heater and thermometers have been tried, two of which are shown in Figure 18. In most experimental runs, a thermometer ( $R_2$  shown in the figure) is mounted on the fiberglass board on which the sample is mounted. In this case, the temperature indicated by that thermometer is taken to be the sample temperature.

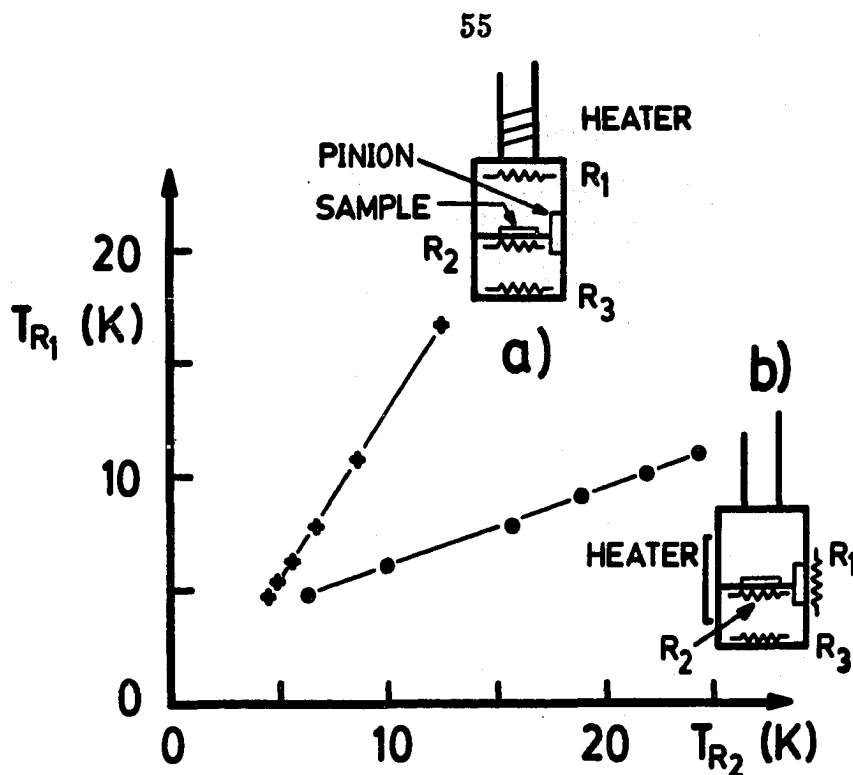


Figure 18. Temperature Gradient. In both (a) and (b) the thermometer  $R_2$  is mounted near the sample on the shaft of the pinion and  $R_3$  is mounted on the inside bottom of the sample holder.  $R_2$  is taken to be the sample temperature. (a) The heater is mounted on the 1/2" diameter stainless steel tube at the top of the sample holder and  $R_1$  is mounted on the inside top of the sample holder. (b) The heater is mounted on one side of the sample holder with  $R_1$  on the other side. The temperature of  $R_1$  is plotted against  $R_2$ , and a strong thermal gradient is seen in both configurations.

This was not the case, however, for the first experiment in which the temperature was raised above 4.2K. Only one thermometer was used.  $R_1$  and the heater were mounted as shown in Figure 18b. In this case, the temperature indicated by that thermometer is a lower limit of the temperature, since the heater and thermometer are on opposite sides of the sample. The sample temperature is determined by using this lower limit and subsequent gradient data as shown in the figure. This temperature correction for the gradient is not expected to give the absolute temperature of the sample, since the temperature gradient varies with each experimental

run. It does, however, give a relative temperature, which is sufficient for the purpose of analyzing the transconductance amplitude data.

Temperatures below 4.2K are obtained by reducing the vapor pressure above the liquid helium, which decreases the temperature of the helium bath. The liquid helium bath is in excellent thermal contact with the sample through the helium exchange gas, so there should be no thermal gradient across the sample holder, and the thermometers placed anywhere on the sample holder should indicate correctly the sample temperature.



## CHAPTER IV

### DATA AND ANALYSIS

#### A. Introduction

The population of the surface subbands in the accumulation layer on n-type InAs is studied. The Shubnikov-de Haas (SdH) effect is used as a probe of the subband population. The behavior of the population with the magnetic field normal to the surface layer has long been understood:<sup>56</sup> Landau quantization of the constant density of states. In an ideally 2DEG the Landau quantization depends on only the normal field component. A parallel magnetic field diamagnetically shifts the subbands up in energy (equation 2.49). Therefore, tipping the magnetic field away from the normal should decrease the subband population because the parallel field component increases the subband energy; the perpendicular field component gives rise to the SdH oscillations from which the subband population is determined.

Also studied is the total depopulation of the subbands in strong parallel fields. This depopulation is observed as oscillatory structure in the transconductance. The temperature dependence of the oscillation amplitude is used to measure the intersubband energy spacing.

The transconductance reveals structure at gate voltages below the accumulation threshold. This structure is attributed to conduction in a 2D impurity band. The effect of a magnetic field (both strength and direction) on the impurity conduction is investigated.

The Shubnikov-de Haas effect is understood physically as follows: in a magnetic field normal to the 2DEG, the electrons condense into Landau energy levels, but occupy only those levels that are below the Fermi level. As the magnetic field strength increases, the highest occupied Landau level is depopulated as it is pushed through the Fermi level. This gives rise to the SdH effect as observed in the conductance (and transconductance) as a function of the magnetic field. The SdH effect is seen as a function of gate voltage as well, since sweeping the gate voltage corresponds to sweeping the Fermi level through the ladder of Landau levels. For a single subband  $i$ , with  $g_s = 2$  and  $g_v = 1$ , the number density is given by equation 2.21, so the total number of electrons is therefore

$$N_{S_i} = \ell \frac{m^*}{\pi \hbar^2} \hbar \omega_c, \quad (4.1)$$

where  $\ell$  is the total number of occupied Landau levels. Using the expression for  $\hbar \omega_c$ , this equation becomes

$$\frac{1}{H} = \ell \frac{e}{\pi \hbar c} \frac{1}{N_{S_i}}. \quad (4.2)$$

The period  $\Delta(\frac{1}{H})_i$  for subband  $i$ , in inverse magnetic field strength is determined by a unity change in the number of occupied Landau levels. The number of electrons in the subband, then, can be determined from the

SdH period,<sup>68</sup> i.e.,

$$N_{S_i} = \frac{e}{\pi \hbar c} \frac{1}{\Delta(\frac{1}{H})_i}. \quad (4.3)$$

## B. Normal Field

### 1. Shubnikov-de Haas Effect

Transconductance data at  $\theta = 0$  is shown in Figure 19 for sample 31-A2( $10^{15}$ ) at 4.2K. In the figure, the transconductance is plotted against inverse magnetic field strength for several values of constant gate voltage. Sets of SdH oscillations with constant period are evident in the curves; each set corresponds to a single electric subband. A total of four subbands have been observed in this sample at the highest gate voltages. The figure also shows representative plots of transconductance-*versus*-gate voltage at fixed magnetic fields. Each transconductance peak is associated with a Landau level at the Fermi level.<sup>55</sup> Notice that the peak positions shift in  $V_G$  as the field strength is changed. This is a consequence of the field dependence of the Landau level separation.

The amplitude of the oscillations depends on the field strength and temperature, and is given by<sup>23,77-79</sup>

$$A(H, T) \propto \frac{k_B T}{(\hbar \omega_c)^{\frac{1}{2}}} \exp\left(-\frac{2\pi^2 k_B T_D}{\hbar \omega_c}\right) \text{csch}\left(\frac{2\pi^2 k_B T}{\hbar \omega_c}\right), \quad (4.4)$$

where  $T$  is the absolute temperature of the electron gas and  $k_B$  is the Boltzmann constant. The Dingle temperature,  $T_D$ , is a measure of the energy broadening of the Landau levels due to collisions,<sup>80</sup> and for a mean

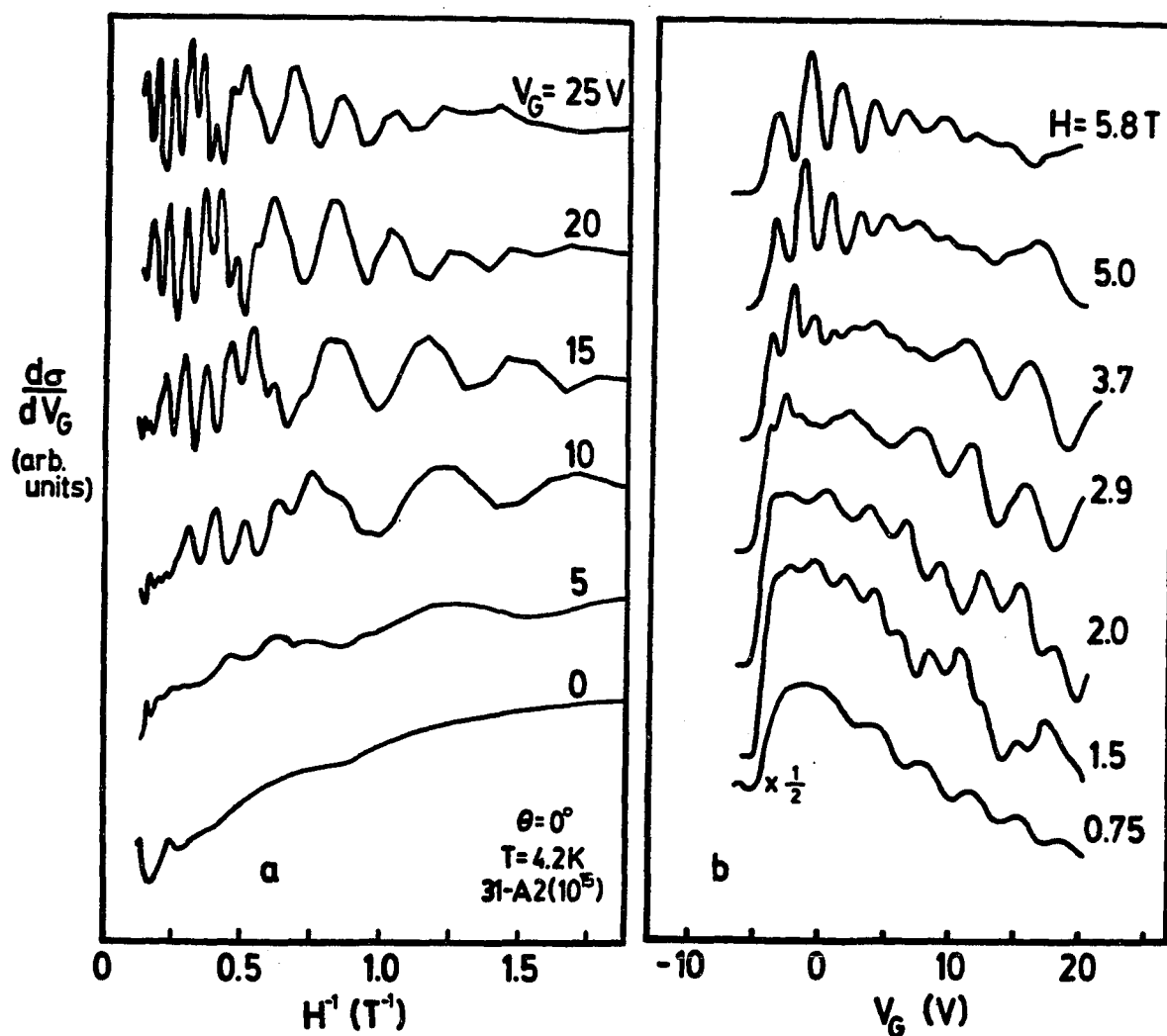


Figure 19. Shubnikov-de Haas Oscillations. The normal field transconductance is plotted in (a) against inverse field strength and against gate voltage in (b). In (a) the period is constant for each subband at fixed  $V_G$ . As  $V_G$  increases the period decreases. The angular look (smoothed-out somewhat by hand tracing) of the data at low fields is due to the digital resolution used in taking  $\frac{1}{H}$ . In both figures the transconductance is plotted in arbitrary units and the traces are displaced along the ordinate axis for clarity. In figure (b) the scale of the bottom trace is one-half that of the other traces.

time between collisions  $\tau_c$ ,

$$k_B T_D = \frac{\hbar}{\pi \tau_c}. \quad (4.5)$$

The magnetic field dependence of  $A$  can be used to determine the Dingle temperature,<sup>81</sup> and the temperature dependence of the amplitude can be used to find the electron effective mass.<sup>23,26,51</sup>

A plot of the values of  $H$  and  $V_G$  at which the peaks occur results in the fan charts of Figure 20. The gate voltage threshold values for each subband are found by extrapolating to  $H = 0$ , and are listed in Table IV. Identification of the correct Landau level sequence can be made from the fan charts by plotting an integer sequence against the inverse of the anticipated values of the magnetic field at which peaks should occur at fixed gate voltage.<sup>55</sup> This is shown in Figure 21. If the integer sequence is chosen correctly, the extrapolated intercept value will be  $-\frac{1}{2}$ . The slopes of the lines in Figure 21 are proportional to the number density of electrons in the subbands at the indicated gate voltage. The subband number densities found this way are plotted against  $V_G$  in Figure 22 for the four subbands. The total surface number density,  $N_s$ , is the sum of the subband densities (equation 2.22), but in accumulation,  $N_s$  can be found also from the device capacitance, where the accumulation threshold value is taken to be the  $i = 0$  threshold, i.e.,

$$N_s = 1.58 \times 10^{11} (V_G + 4.6V) \frac{1}{\text{cm}^2 \text{V}}. \quad (4.6)$$

The slopes of Figure 22 are the subband population rates,  $\frac{dN_{s_i}}{dV_G}$ , and are listed in Table IV.

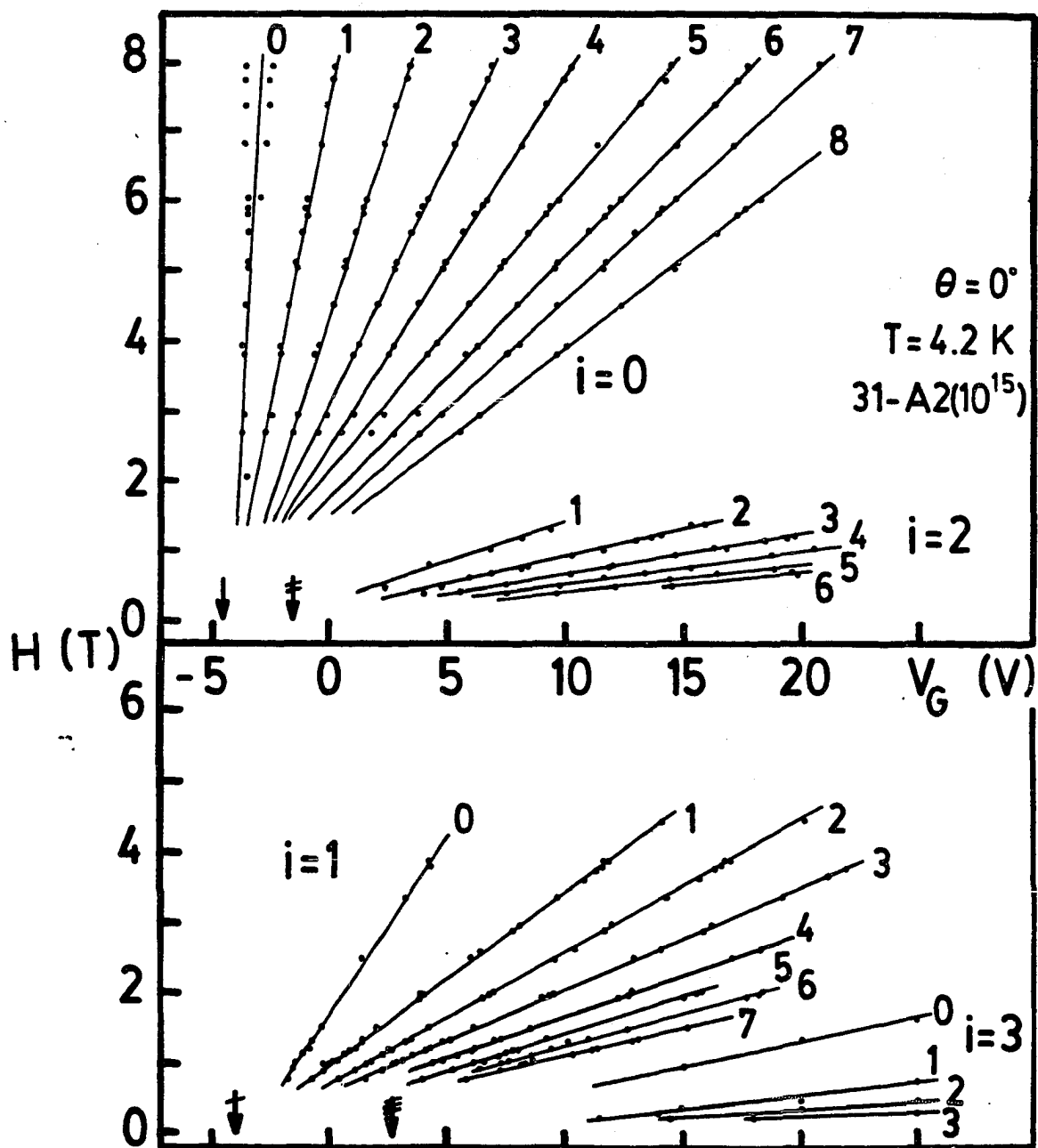


Figure 20. Fan Chart. The values of  $H$  and  $V_G$  at which the peaks of Figure 19 occur are plotted and result in the fan diagram. The lines are labeled with the Landau integer  $j$ . The electric subband threshold gate voltages (arrows) are taken from the extrapolation to  $H = 0$ , and are listed in Table IV. The number of slashes on the arrows corresponds to the index  $i$ .

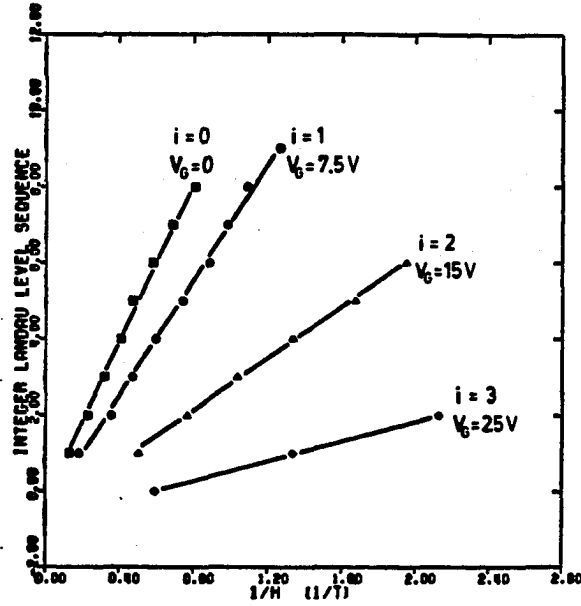


Figure 21. Landau Level Sequence. At fixed  $V_G$  the anticipated values in magnetic field of the peak position are determined from the fan charts of Figure 20. Integer values are assigned to the peaks and are plotted against  $\frac{1}{H}$ . The slopes of the line are proportional to  $N_S$  at the indicated gate voltages.

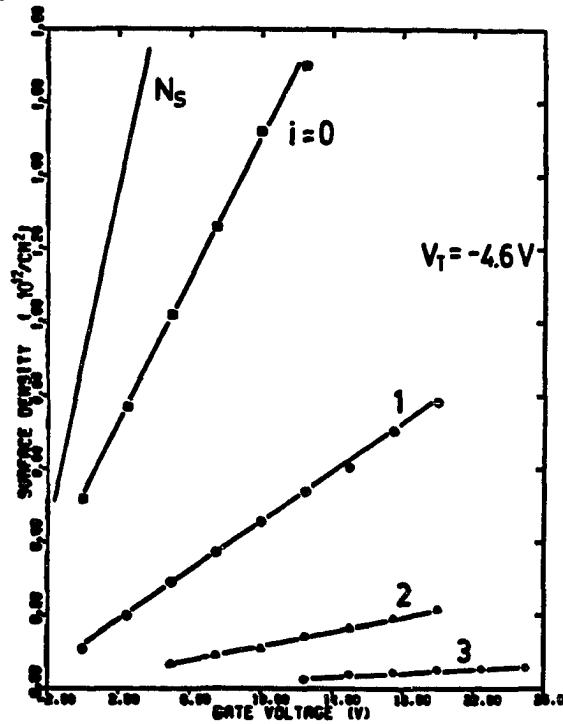


Figure 22. Surface Density. The two-dimensional surface density  $N_S$  is plotted against gate voltage for the four electric subbands. The slope of the lines gives the electric subband population rates and are listed in Table IV. Extrapolation of the ground state to zero population gives the accumulation threshold  $V_G = -4.6V$ . Also plotted is the total 2D surface density  $N_S$  determined from the measured capacitance.

## 2. Spin Splitting

The spin degeneracy in the Landau levels can be lifted by a magnetic field and observed as a splitting of the transconductance peaks. In perpendicular fields this spin splitting, as shown in Figure 23, is evident in sample 31-A2( $10^{15}$ ) only in the ground state Landau level of the  $i = 0$  subband in high magnetic fields,  $H \geq 6T$ , and at low gate voltages,  $V_G \leq -2.5V$  ( $N_s \leq 3 \times 10^{11} \text{ cm}^{-2}$ ). This surface density is low enough that the non-parabolicity (equation 2.25) can be neglected. The Landau energy is split by an amount

$$\Delta\epsilon = \pm \frac{1}{2}g\beta H, \quad (4.7)$$

where  $\beta = \frac{e\hbar}{m_e c}$  is the Bohr magneton. For  $g = -15$  [reference 53] this energy is  $\sim 5 \text{ meV}$  at  $H = 6T$ . The energy difference between spin levels,  $2|\Delta\epsilon| = \hbar\omega_s$ , is written in terms of the spin angular frequency  $\omega_s = |g|\frac{eH}{m_e c}$ . Because the Landé  $g$ -factor is negative, the spin up ( $+\frac{1}{2}$ ) level has a lower energy than the spin down ( $-\frac{1}{2}$ ) level and each level contains the number of electrons given by equation 2.48 with  $g_s = 1$ . An estimate of the gate voltage difference between the spin split peaks in transconductance shown in Figure 23 can be made from the subband population rate and the spin energy  $\hbar\omega_s$ . Consider the constant density of states (equation 2.20) without the spin degeneracy lifted, i.e.,  $g_s = 2$ . In this case, the spin energy width  $\hbar\omega_s$  corresponds to a number of electrons



$$\begin{aligned}
\Delta N^{\text{spin}} &= D(E)\hbar\omega_s \\
&= \left(\frac{m^*}{m_e}\right)|g|\frac{eH}{\pi\hbar c}.
\end{aligned} \tag{4.8}$$

Now the required gate voltage change to populate this number is

$$\Delta V_G^{\text{spin}} = \frac{\Delta N^{\text{spin}}}{\frac{dN_{s_i}}{dV_G}}. \tag{4.9}$$

Using the  $i = 0$  subband population rate  $1.11 \times 10^{11} \text{ cm}^{-2}\text{V}^{-1}$  and  $g = -15$ , this last expression gives a value of  $\Delta V_G^{\text{spin}} = 1.2\text{V}$  for the spin split peak at  $H = 7.69\text{T}$ , which compares to the measured value of  $1\text{V}$ .

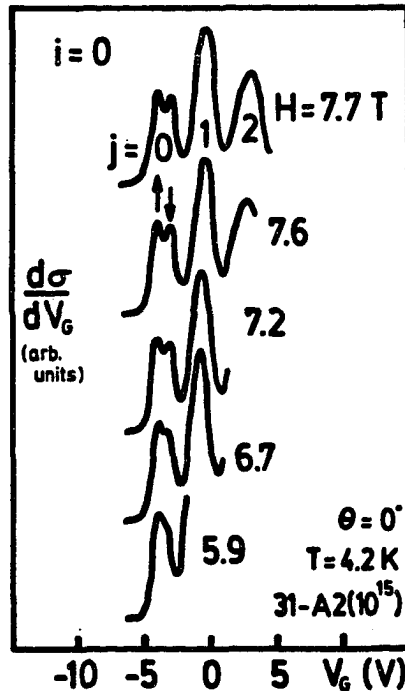


Figure 23. Spin Splitting. In the  $i = 0$  electric subband, splitting of the ground state ( $j = 0$ ) Landau level is observed. The spin up state has a lower energy than the spin down state and therefore is occupied at lower gate voltages. The peak positions are plotted in the fan chart of Figure 20.

### C. Parallel Field

#### 1. Hybrid Subbands

a. Sample 31-A2( $10^{15}$ ). Transconductance measured in a parallel field,  $\theta = 90^\circ$ , for the same sample is shown in Figure 24, where the source/drain current is  $\sim 45^\circ$  to the field direction. Two sets of data are shown:  $\frac{dg}{dV_G}$  vs.  $H$  for several values of constant  $V_G$  and  $\frac{dg}{dV_G}$  vs.  $V_G$  for several values of  $H$ . In these latter curves, notice that the area under the curves is proportional to the sample conductivity, and that as the field increases the conductivity (area) increases. This is in contrast to the decrease in transverse conductivity with increasing  $H$ , as, for example, illustrated by Figure 12. One scattering mechanism is surface scattering and the scattering rate is greater for the lowest lying subbands, since these subbands are more tightly bound to the surface.<sup>24</sup> Another important scattering mechanism is intersubband scattering.<sup>69</sup> As the parallel field increases, at fixed gate voltage for example, the density of states in the subbands increases<sup>70</sup> as the dispersion becomes a hybrid mix of electric and magnetic states. In addition, the hybrid subbands are diamagnetically shifted up in energy,<sup>36,71</sup> and the energy spacing between successive subband minima increases with increasing  $H$ . With this increase in energy the electron wavefunction extends farther into the semiconductor, decreasing the surface scattering rate;<sup>70</sup> with the increased energy spacing between subband minima, the intersubband scattering is decreased.<sup>72</sup> Thus the conductivity increases. The increase in the conductance of an inversion layer on p-Si

at high magnetic fields also has been attributed to the effect of decreased surface scattering as the electrons are pushed away from the surface by the magnetic field.<sup>85</sup>

Also observed in Figure 24 is strong oscillatory structure not periodic in  $\frac{1}{H}$  or  $V_G$ , unlike the normal field oscillations.<sup>73</sup> Similar structure is observed in InSb,<sup>86</sup> and is discussed in § IV.E.1. The mechanism identified with this structure is illustrated in Figure 25. At sufficiently high magnetic fields, the diamagnetic energy shift will raise a subband above the Fermi level, and the increased density of states of the lower lying subbands accommodates the surface charge in fewer subbands. A qualitative argument can be made for the structure in the transconductance to be identified with the coincidence of a subband minima at the Fermi level, and is illustrated in Figure 26. At a constant magnetic field, as the gate voltage is increased above the mobility turn-on, the conductance increases since the number of electrons in the surface channel accumulation layer increases. However, as the gate voltage increases further, the rate of increase of the conductance drops somewhat because of the increased surface scattering as the subbands become bound closer to the surface (deeper in the well). At the population of another subband with increasing  $V_G$  (i.e., the coincidence of a subband minima at the Fermi level), the rate of increase in conductance decreases further because of the intersubband scattering with the newly occupied subband. Thus a minimum in transconductance corresponds to a dip in the conductance (peak in resistance) and is identified as occurring at the oc-

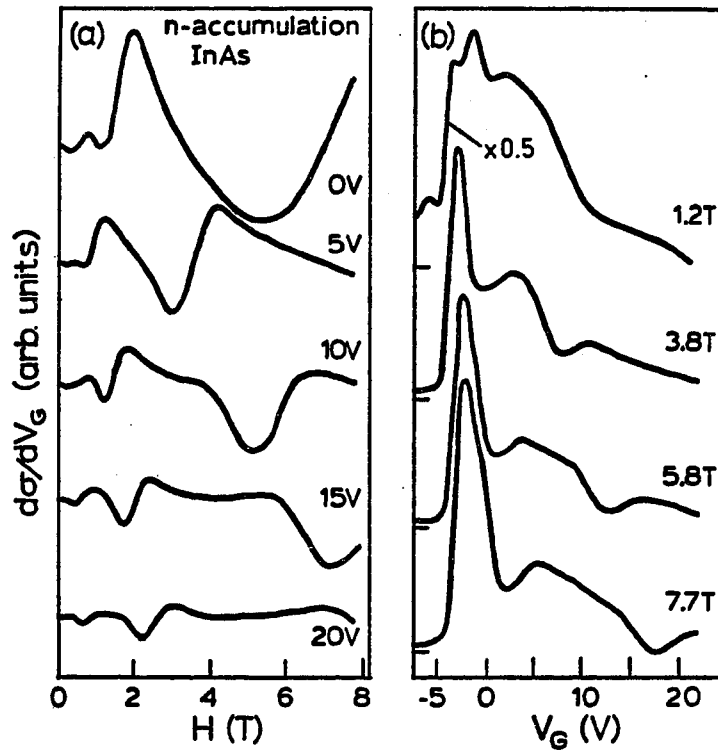


Figure 24. Parallel Field Transconductance. The transconductance at 4.2 K of sample 81-A2( $10^{15}$ ) is plotted against  $H$  at various values of  $V_G$  in (a) and against  $V_G$  at various values of  $H$ . In figure (b) the tick marks along the ordinate are the zero values of transconductance; the area under the curves is proportional to the conductance and is seen to increase as the field increases.

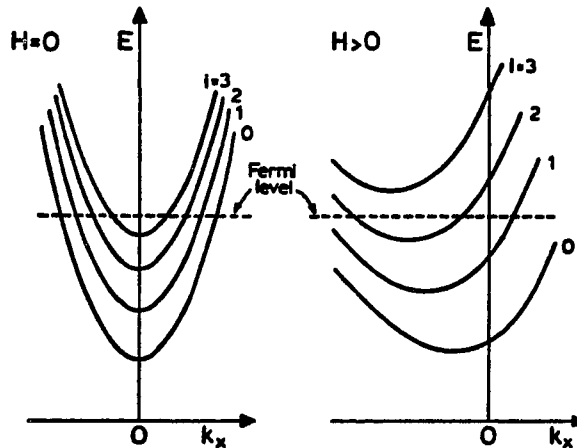


Figure 25. Depopulation Mechanism. With an increasing parallel field the hybrid subbands are pushed up in energy and the spacing between subbands increases. In a strong enough field the highest occupied subband is pushed above the Fermi level, with a consequent total depopulation.

cupation of a subband.<sup>74,75</sup>

A plot of  $H$  and  $V_G$  at which the minima occur is given in Figure 27, and since the minima are identified with the occupation of a hybrid subband, this plot gives the shift in threshold gate voltage for a given parallel field. The four lines in the figure are identified with the  $i = 1 - 4$  subbands. It may be noted that the  $i = 4$  subband has not been observed in normal field SdH experiments and that this identification is different than previously reported.<sup>73</sup> This change in identification of the subband index is made in order to resolve some discrepancies in observed effects in the data<sup>84</sup> and in anticipation of the arguments given below. The former numbering scheme was introduced primarily because 1) the number of minima in the parallel transconductance must be the same as the number of subbands occupied at  $H = 0$ , and 2) the observed structure in parallel transconductance occurs at gate voltages above the  $H = 0$  threshold for subband occupation. Number one is not necessarily correct since a) the accumulation threshold voltage (extrapolation of the transconductance turn-on region) does not shift in a parallel field, and b) the possibility of the magnetic field lifting the spin degeneracy in the hybrid subbands is ignored. Number two is a more serious argument; however, a close inspection of the lines in Figure 27 reveals a slight discrepancy in the extrapolated  $V_G$  threshold values in the parallel field with the subband threshold voltages from the perpendicular field.

Because the perturbation approach (equation 2.49) is not valid at

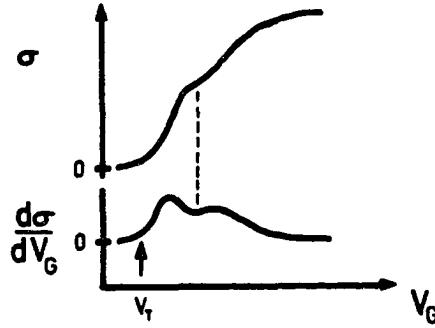


Figure 26. Schematic Picture of Conductance. The increase in  $\sigma$  beyond the threshold gate voltage is due to the accumulation of electrons at the surface. The dip in  $\sigma$  corresponds to the local minima in transconductance (dashed line) and is due to the intersubband scattering at the occupation of another subband.

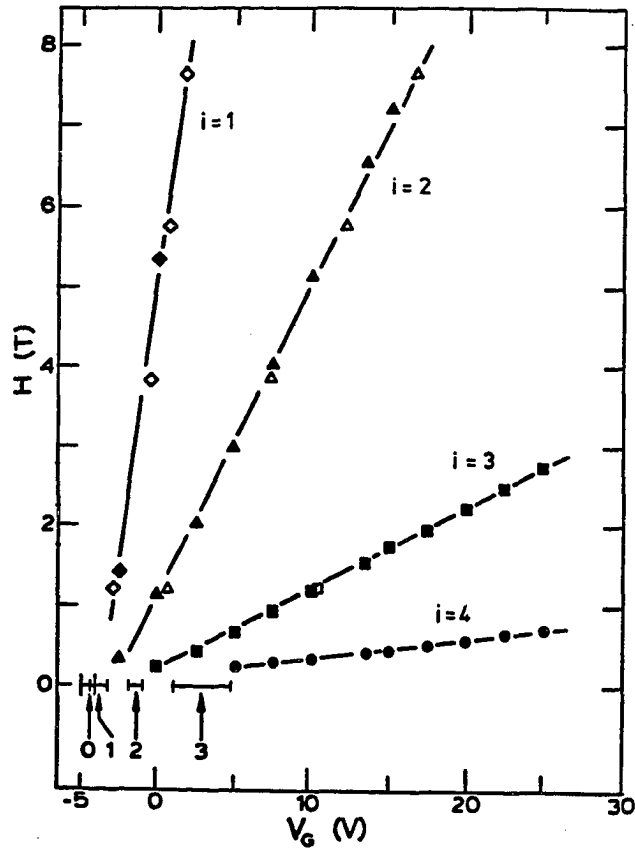


Figure 27. Hybrid Fan Chart. The value of  $H$  and  $V_G$  at which the minima of Figure 24 occur are plotted here, with the subband identification  $i = 1-4$ . The  $i = 0$  subband does not shift the accumulation threshold with parallel field. The arrows and error bars are the electric subband threshold values taken from the fan charts of Figure 20. Open (filled) symbols are from  $H(V_G)$  sweeps.

large magnetic fields, the shift in energy of the subband minima is taken to be on the order of  $\hbar\omega_c$  for all subbands. This leads to a depopulation of

$$\Delta N_{S_i} \simeq D_i(E_F)\hbar\omega_c \quad (4.10)$$

electrons per unit area from subband  $i$ . Including the non-parabolicity of the conduction band (equations 2.25 and 2.26), but neglecting the increase in density of states due to the parallel field, the density of states at the Fermi level is

$$D_i(E_F) = \frac{m^*}{\pi\hbar^2} \left(1 + \frac{4\pi\hbar^2 N_{S_i}}{E_G m^*}\right)^{\frac{1}{2}}. \quad (4.11)$$

This correction over the usual expression for the 2D density of states (equation 2.20) is most important for the lower lying subbands. Using  $E_G = 410$  meV [reference 76], the increase is important for  $N_{S_i} \geq 10^{12} \text{ cm}^{-2}$ , and for the example in Table IV, is about 40% and 14% for the ground and first excited states, respectively. An estimate of the shift in the threshold gate voltage  $\Delta V_T^i(H) = V_T^i(H) - V_T^i(0)$ , due to a parallel field of one Tesla can be made from the normal field data. The expected threshold shift in each subband is related to the normal field population rate as

$$\Delta V_T^i(H) \simeq \frac{\Delta N_{S_i}}{\frac{dN_{S_i}}{dV_G}}. \quad (4.12)$$

These estimated shifts in the threshold voltage for the  $i = 0, 1, 2, 3$  subbands are, respectively (Table IV), 0.6, 1.7, 5.0 and 20 V. The slopes of the experimental lines of Figure 27 give a gate voltage threshold shift of 1.5, 4, 10 and 35 V for the  $i = 1, 2, 3, 4$  subbands, respectively.

**TABLE IV**  
**Population Rates and Threshold Shifts,**  
**Sample 31-A2( $10^{15}$ )**

$i$	$^a V_T^i(0)$ (V)	$^b \frac{dN_{S_i}}{dV_G}$ ( $10^{11} \text{ cm}^{-2} \text{ V}^{-1}$ )	$^c N_{S_i}(V_G = +5.0V)$ ( $10^{11} \text{ cm}^{-2}$ )	$^d \Delta N_{S_i}$ ( $10^{11} \text{ cm}^{-2}$ )	$^e \Delta V_T^i(H = 1T)$ (V)
0	$-4.6 \pm 0.4$	1.11	10.2	0.69	0.6
1	$-4.0 \pm 0.5$	0.32	2.90	0.55	1.7
2	$-1.6 \pm 0.4$	0.10	0.648	0.50	5.0
3	$+2.7 \pm 2$	0.024	0.116	0.49	20.

<sup>a</sup>Threshold values from Figure 20

<sup>b</sup>Population rates from Figure 22

<sup>c</sup>Subband number densities from Figure 22 at  $V_G = +5.0V$ , corresponding  
to  $N_S = 1.5 \times 10^{12} \text{ cm}^{-2}$

<sup>d</sup>Calculated from equation 4.10

<sup>e</sup>Calculated from equation 4.12



b. Sample IAS/34( $10^{17}$ ). Hybrid subband depopulation has been observed in sample IAS/34( $10^{17}$ ), which has a greater bulk number density,  $n = 1.4 \times 10^{17} \text{ cm}^{-2}$ . In samples of this doping up to three electric subbands can be occupied.<sup>24,54</sup> In this experiment the accumulation threshold, as determined from the  $i = 0$  normal field SdH oscillations, is  $-19.0\text{V}$ . The surface density, then, via the capacitance (measured with a Data Precision Model 938 Capacitance Meter at  $V_G = 1\text{V}$  and at a frequency of  $1000 \text{ Hz}$ ) is

$$N_s = 1.46 \times 10^{11} (V_G + 19\text{V}) \text{ cm}^{-2} \text{ V}^{-1}. \quad (4.13)$$

Because of the low source/drain resistance, the differential resistivity  $\frac{d\rho}{dV_G}$  is measured as a function of  $H$  and  $V_G$ , and at  $\theta = 90^\circ$  is shown in Figure 28. The hybrid fan chart in Figure 29 is a plot of the peak positions of  $\frac{d\rho}{dV_G}$  in  $H$  and  $V_G$ , which correspond to the minima in transconductance. An analysis similar to that of the previous section (IV.C.1.a) can be made in order to estimate the slopes of the lines in the hybrid fan chart. Taking into account the non-parabolic conduction band, the number of electrons depopulated by the parallel field is given by equation 4.10 and the density of states is given by equation 4.11. At a total surface density of  $N_s = 2 \times 10^{12} \text{ cm}^{-2}$ , the  $i = 0, 1$  subband populations are

$$\begin{aligned} N_{S_0} &= 1.0 \times 10^{12} \text{ cm}^{-2}, \\ N_{S_1} &= 0.4 \times 10^{12} \text{ cm}^{-2}. \end{aligned} \quad (4.14)$$

The expected shift in threshold gate voltage due to a parallel field is given

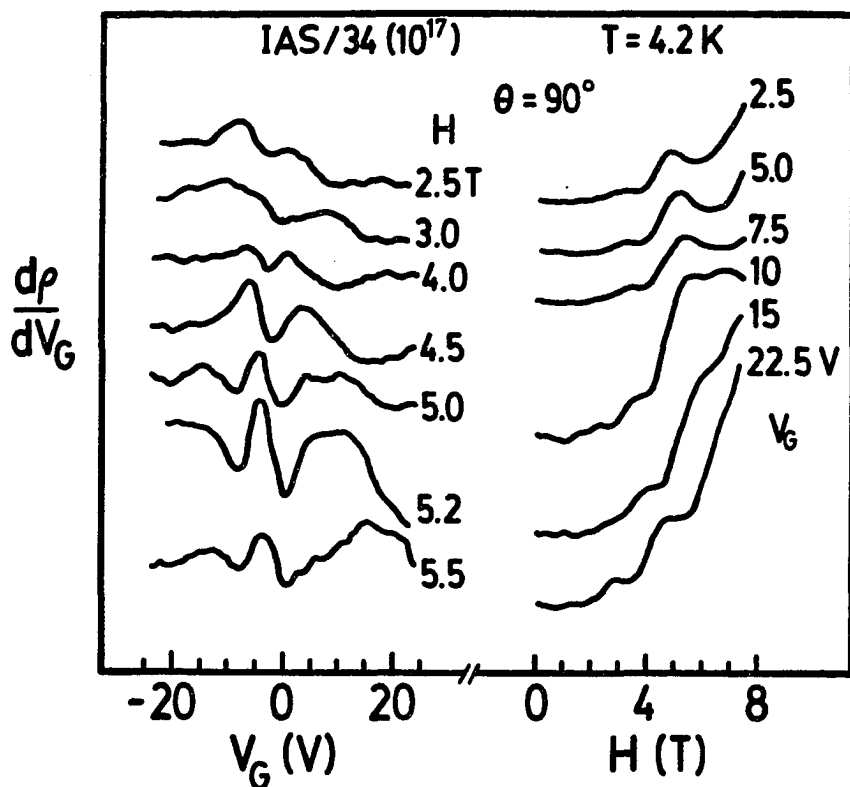


Figure 28. Hybrid Oscillations in Sample IAS/34( $10^{17}$ ). The differential resistance in parallel field is plotted against gate voltage at fixed  $H$  and against  $H$  for fixed  $V_G$ . The curves are not drawn to the same scale.

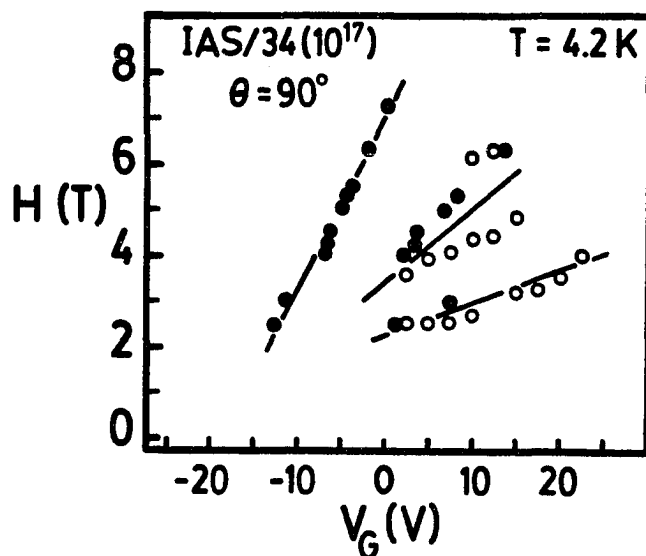


Figure 29. Hybrid Fan Chart. The values of the maxima in  $H$  and  $V_G$  of Figure 28 are plotted here. The open (filled) symbols are from  $H$  ( $V_G$ ) sweeps.

by equation 4.12. Finding the population rates for this sample in a similar manner as that of Figure 22, for a field of 1T the threshold shifts are 0.72 and 2.3V for the  $i = 0, 1$  subbands, respectively. The experimental values from the slopes of the hybrid fan chart of Figure 29 are, for the  $i = 1, 2, 3$  subbands 2.5, 5.8 and 12 V, respectively.

## 2. Spin Splitting

In an experiment subsequent to the one which produced the data of Figure 24, structure in the parallel transconductance is evident which was not previously observed [in the same sample: 31-A2( $10^{15}$ )]. In the first experiment the gate electrode was left floating during the cool-down procedure and the accumulation threshold was  $-4.6V$ . In the subsequent experiment the gate was shorted to the source during cool-down, and in this latter case, the threshold voltage shifted to  $-13.6V$ . This shift in  $V_T$  indicates that in the first experiment bias charges in the surface were frozen in during cool-down. The fact that the threshold shifted to a lower gate voltage in the subsequent experiment indicates that the impurities were positively charged, i.e., electron traps. The parallel field transconductance of the second experiment is shown in Figure 30, clearly indicating the structure that was not observed in the first experiment, as does the associated hybrid fan chart of Figure 31.

This additional structure is attributed to spin splitting of the hybrid subbands. An analysis similar to that of § IV.C.1.a can be made of the slope

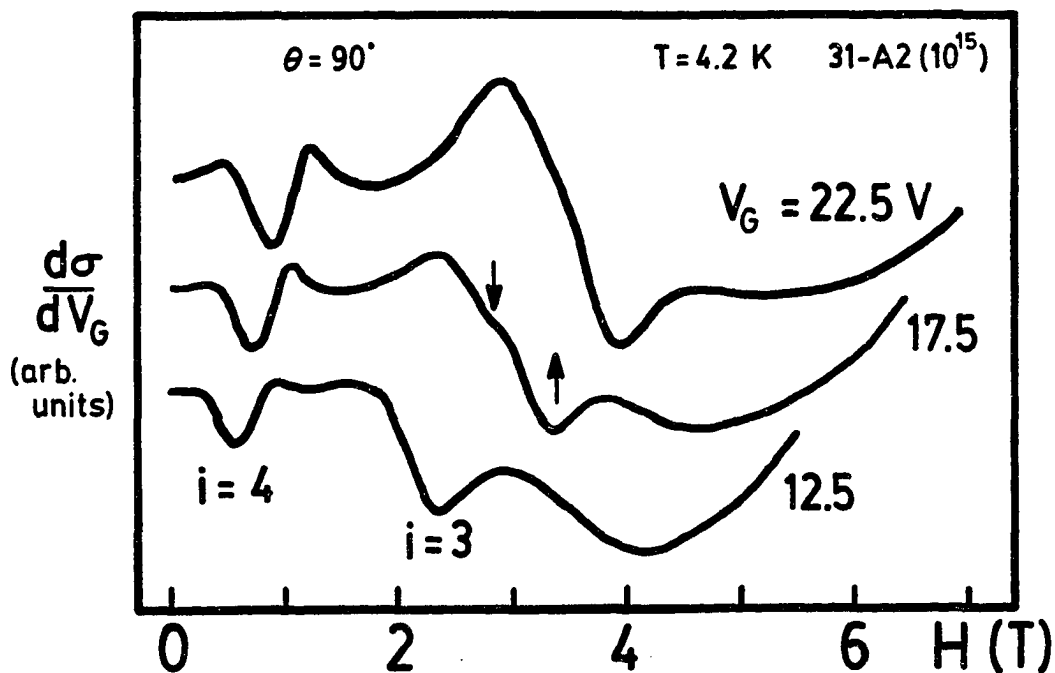


Figure 30. Spin Split Hybrid Oscillations. Doublet structure shown here appears in the  $i = 3$  hybrid subband. The structure is seen also at  $V_G = 15V$  at a slightly elevated temperature in Figure 39.

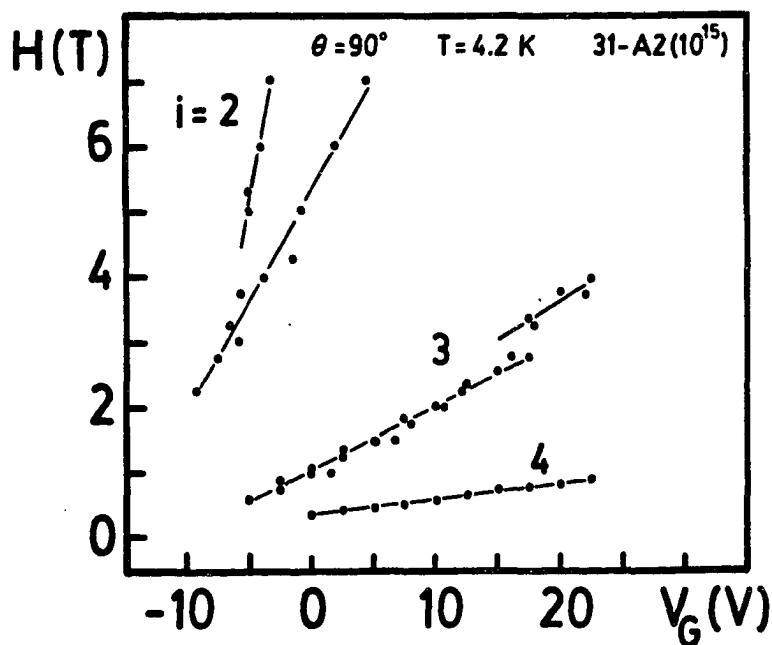


Figure 31. Spin Split Hybrid Fan Chart. Spin splitting is observed in only the  $i = 2$  and  $3$  hybrid subbands. In the  $i = 3$  subband the doublet structure appears only in the range  $15V \leq V_G \leq 20V$ .

of the spin split hybrid fan chart. If spin splitting is observed, i.e., if  $g_s = 1$ , then relative to the unsplit subband, the density of states (equation 4.10), the number of electrons depopulated by the parallel field (equation 4.9), and the shift in gate voltages (equation 4.11) are all decreased by one half, and therefore, the expected gate voltage threshold shift is decreased by one half. The number of electrons depopulated by the parallel field is not given by equation 4.9, but rather by integrating the density of states over the energy range  $\hbar\omega_c$  below the Fermi level. Because the density of states is not constant the spin splitting does not populate the two spin levels evenly, i.e., with both spin levels fully occupied, the spin down level has more electrons than the spin up level.

The spin splitting should be observed if the spin energy is at least on the order of the energy spacing between the hybrid subband minima. This is shown in Figure 32. The energy spacing between adjacent hybrid subband minima is

$$\Delta E_{ij} + \hbar\omega_c \quad (4.15)$$

where  $\Delta E_{ij}$  is the intersubband energy spacing between electric subbands  $i$  and  $j$ . The energy difference between spin levels is

$$2|g|\frac{\hbar eH}{cm_e} \quad (4.16)$$

The case shown in Figure 32 is the condition that the relations (4.15) and (4.16) are equal. This condition is probably too extreme (i.e., (4.15) is probably greater than (4.16)) for the data of Figures 30 and 31, since the

spin splitting is just resolved. However, a comparison of the two relations can be made from the data. In Figure 31 the (extrapolated) values of  $H$  and  $V_G$  at which the spin splitting first occur are, for the  $i = 2$  hybrid subband,  $H = 2.9T$ ,  $V_G = -7.0V$  ( $N_s = 1.0 \times 10^{12} \text{ cm}^{-2}$ ); and for the  $i = 3$  hybrid subband,  $H = 1.0T$ ,  $V_G = 0V$  ( $N_s = 2.1 \times 10^{12} \text{ cm}^{-2}$ ). The  $\Delta E_{ij}$  are estimated from Figure 11 of reference 24, and the values (at corresponding  $N_s$  values) are  $\Delta E_{12} \simeq 15 \text{ meV}$  and  $\Delta E_{23} \simeq 5 \text{ meV}$ . Using the bulk value of  $|g| = 15$ , the relation (4.16) is 10 meV for the  $i = 2$  subband; the relation (4.15) for the  $i = 1, j = 2$  subbands is 29meV. For the  $i = 3$  subband the relation (4.16) is 3.4meV; the relation (4.15) for the  $i = 2, j = 3$  subbands is 10meV. The fact that (4.15) is greater than (4.16) in both cases may also be an indication that the  $g$ -factor is surface enhanced. Spin splitting is resolved in a magnetoresistance experiment on the InAs/GaSb sample described in the next section, and a surface enhanced  $g$ -factor of 19-23 is reported.<sup>64</sup> In Si inversion layers the  $g$ -factor is enhanced<sup>51</sup> from the bulk Si value of about two and is found to depend on the 2D number density and magnetic field strength.<sup>52</sup>

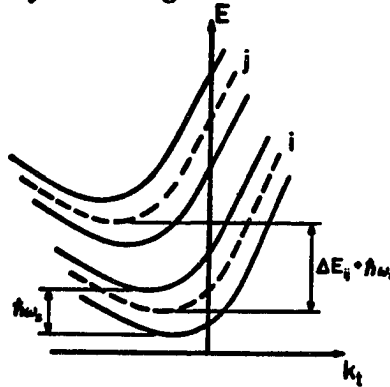


Figure. 32 Spin Split Hybrid Dispersion Relation. The spin splitting condition shown here is expected to be an overestimate of the actual splitting since the doublet minima of Figure 30 is just discernible.  $k_t$  is the wavevector transverse to the magnetic field direction in the plane of the 2DEG.

### D. Tipped Field

One effect of a parallel magnetic field, as discussed in the previous section, is to raise the energies of the subbands. On the other hand, a perpendicular field creates Landau quantization from which the subband populations can be determined via the SdH effect. Tipping the magnetic field away from the sample normal produces a mixture of parallel and perpendicular field components. In this event, a combination of the effects just mentioned can lead to intersubband-cyclotron resonance effects,<sup>82</sup> wherein photon induced transitions occur between different Landau levels of different subbands. Furthermore, the tipped magnetic field couples the motion in the direction normal to the surface to the in-plane motion, leading to a parallel field dependence on the Landau level spacing.<sup>83</sup>

An example of the combination of these effects is shown in Figure 33. The transconductance of sample 31-A2( $10^{15}$ ) is measured as a function of gate voltage with the total field strength kept constant at various tipped field angles. For comparison, data with the same normal field but no parallel field are also shown. It is evident from this data that the accumulation threshold gate voltage does not shift in parallel field. The structures labeled  $i = 1$  and  $2$  are identified from the normal field SdH oscillations. Notice that at small angles there is little effect due to the small parallel field: a slight shift in  $V_G$  and a decrease in amplitude of the transconductance structure.

At large tilt angles, for example the trace shown at  $\theta = 80^\circ$ , the

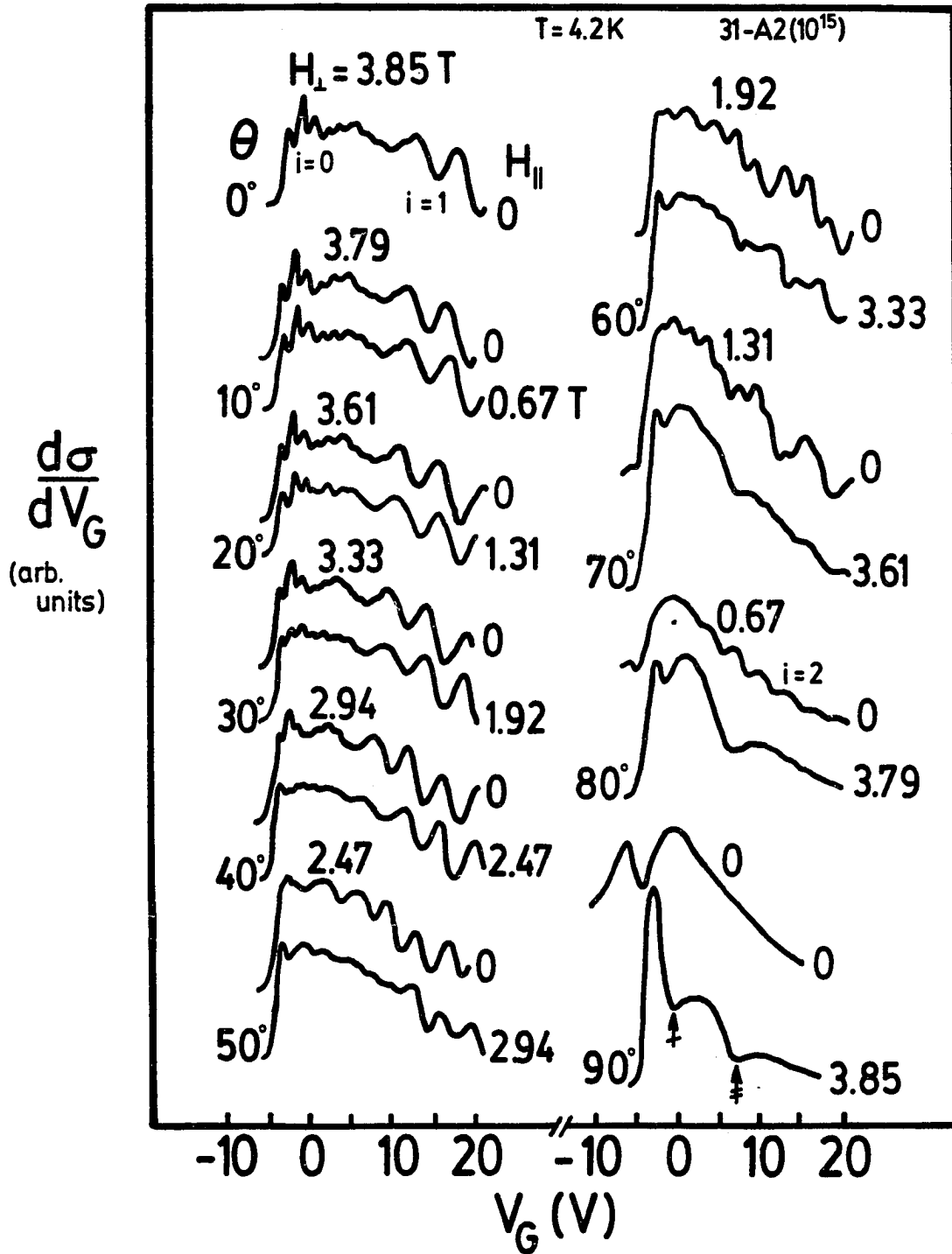


Figure 33. Transconductance in Tipped Fields. Each pair of traces has the same  $H_{\perp}$  and the top trace of each pair has  $H_{\parallel} = 0$  (i.e.,  $\theta = 0$ ). Notice that at  $\theta = 80^\circ$  the  $i = 2$  and 3 hybrid oscillations and the  $i = 2$  SdH oscillations are present.



hybrid oscillations are present along with the SdH oscillations. Here, the SdH oscillations are identified with the  $i = 2$  subband. The SdH oscillations are seen only for gate voltages greater than the  $i = 2$  hybrid subband threshold (contradictory to our original hybrid structure numbering scheme<sup>84</sup>).

A similar effect is seen in Figure 34. Here, a set of transconductance-*versus*-magnetic field curves are shown at fixed gate voltage, for various angles. In the  $\theta = 0^\circ$  trace, the normal field SdH oscillations are identified. At small angles the structure due to a given Landau level is seemingly pushed to greater total field strengths as the tipping angle is increased. This is simply because a greater total field is required to produce the same  $H_\perp = H \cos \theta$  as in the  $\theta = 0^\circ$  trace. Notice that in the  $\theta = 80^\circ$  trace, the hybrid structure and the SdH oscillations are present. Here, the  $i = 2$  oscillations are seen to occur at fields for which the second excited state is expected to be occupied (again in contrast to our original numbering scheme<sup>84</sup>).

In order to determine the effects on subband population due to a parallel component of magnetic field, the ideal experiment would be to apply a constant parallel field and sweep the perpendicular field, thus extracting the subband number density as a function of parallel field. Another method is to take a series of  $V_G$  sweeps with a constant parallel field at various perpendicular fields, producing a fan chart from which the subband population rates can be determined. It is difficult to extract the

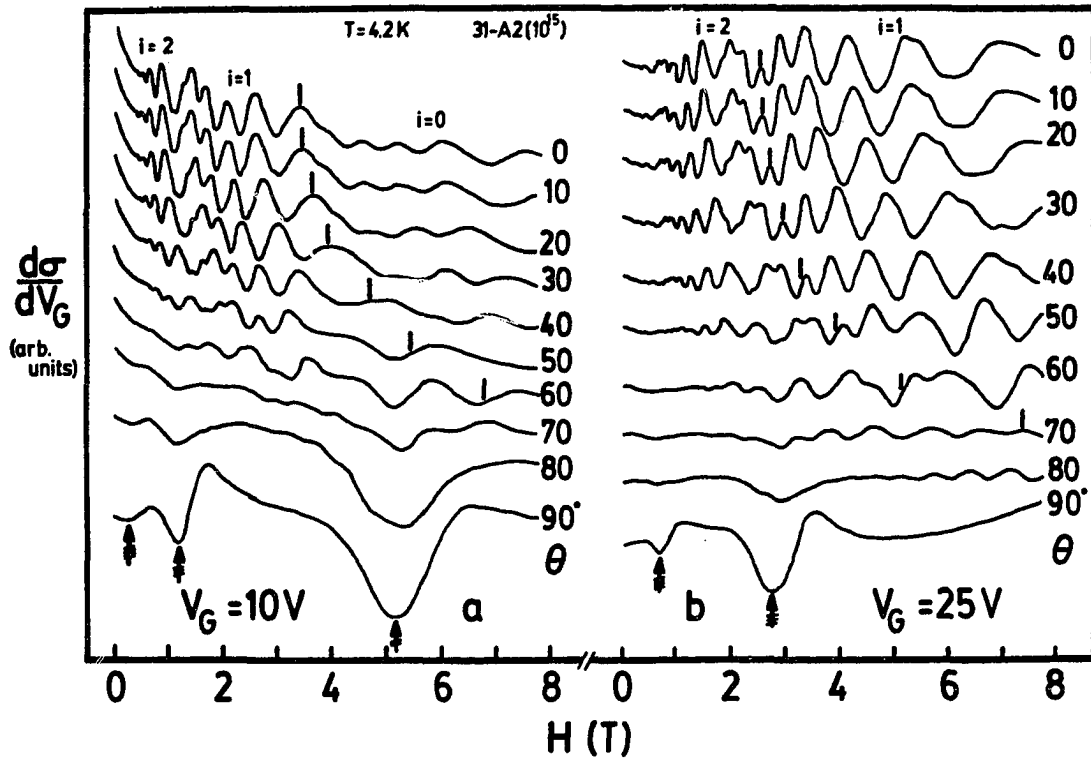


Figure 34. Transconductance in Tipped Fields. Transconductance is plotted against field strength at various angles for a gate voltage of (a) 10 V and (b) 25 V. The vertical bar above the data represents an increasing field as  $\frac{1}{\cos \theta}$ , showing that for small angles,  $\theta \leq 30^\circ$ , the structure depends on only the normal field component.

parallel field effects on the subband population by sweeping the magnetic field at a fixed tipped field angle, since both field components change.

An alternative method, employed here, is to sweep the angle, keeping the gate voltage and total magnetic field strength constant, as shown in Figure 35. The SdH oscillations are readily apparent, yet it is more instructive to see the data as in Figure 36, where the transconductance is plotted against  $H_{\perp}^{-1}$ . In this figure, along with the transconductance obtained by varying  $\theta$ , is a curve obtained by sweeping  $H = H_{\perp}$  at  $\theta = 0^{\circ}$ . It is seen from this figure that as the sample is rotated the period of the  $i = 2$  oscillations is increased relative to the  $\theta = 0^{\circ}$  trace, clearly indicating the subband depopulation by the parallel field. The population is then determined from the perpendicular field component and is given by (see Eq. 4.3)

$$N_{S_i} = \frac{e}{\pi \hbar c} \frac{1}{\Delta(H_{\perp}^{-1})_i}, \quad (4.17)$$

where the 2D expression is assumed to be independent of  $H_{\parallel}$ . Both  $H_{\parallel}$  and  $H_{\perp}$  change as the angle is swept. However, at large angles, for a small change in  $\theta$ , the change in  $H_{\parallel} = H \sin \theta$  is small compared to the change in  $H_{\perp} = H \cos \theta$ .

The depopulation of the subbands by the parallel field is illustrated in Figure 37. The data at  $H_{\parallel} = 0$  comes from the normal field SdH oscillations (Figure 22) and help to provide the tipped field subband identification. The tipped field data come from plots of transconductance like that of Figure 36. Average values of both  $H_{\parallel}$  and the period in inverse perpen-

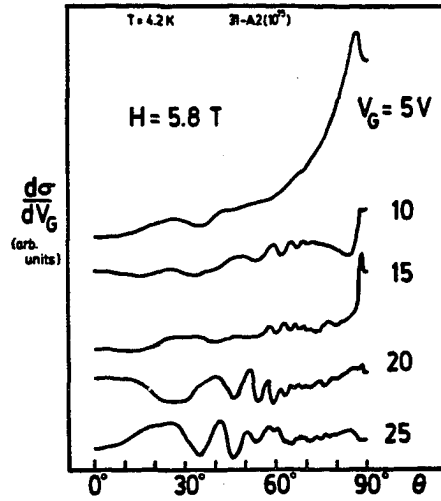


Figure 35. Transconductance-*versus*-Angle. The SdH oscillations are seen in these traces taken at fixed  $H$  and  $V_G$  as the angle is swept.

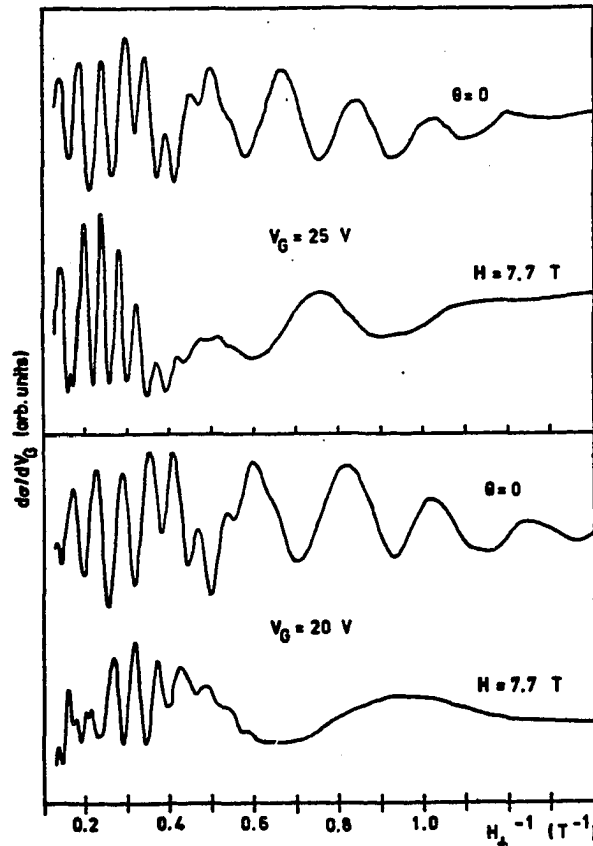


Figure 36. Transconductance-*versus*- $\frac{1}{H_{\perp}}$ . The bottom trace of each box comes from the angle sweep data. At both gate voltages the period in inverse field is increased compared to the  $\theta = 0$  trace.

dicular field over several oscillations are used in the figure. A significant decrease in the population of the  $i = 2$  subband is seen with increasing parallel field, especially at the higher gate voltages. The arrows along the axis of abscissas point to the values of parallel field (only) at which the hybrid fan chart of Figure 27 predicts total depopulation. (These data were taken during the same experimental run.) By the same analysis, no depopulation of the  $i = 1$  subband is seen at strong gate voltages in the same range of  $H_{\parallel}$ , as expected by inspection of the hybrid fan chart.

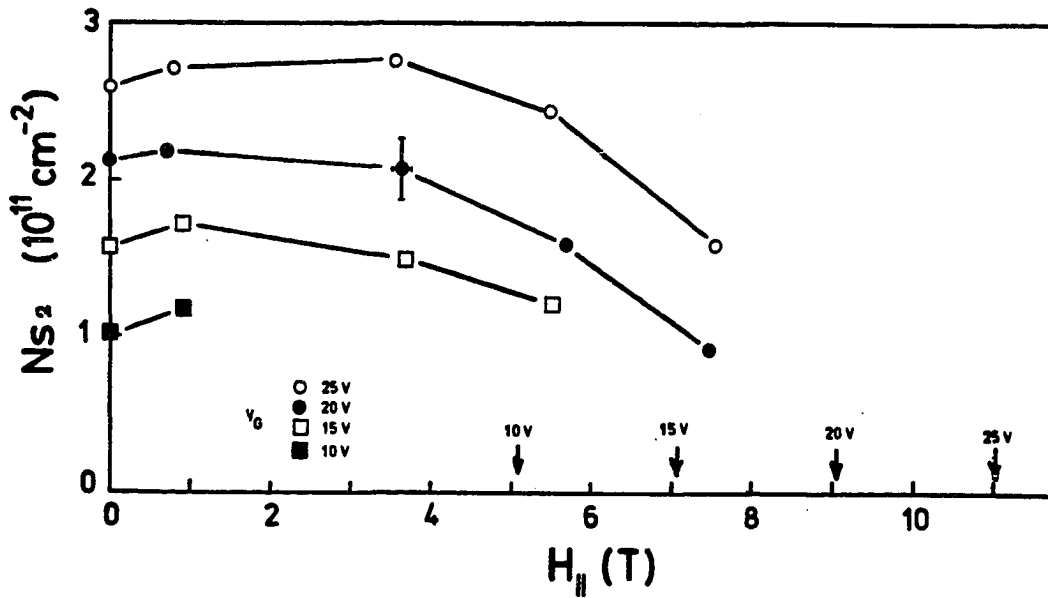


Figure 37. Depopulation of the  $i = 2$  Subband. The number density as determined by equation 4.17 with the period measured from data such as that in Figure 36. The arrows predict the total depopulation in a parallel field (only) given by the hybrid fan chart of Figure 27.

At  $V_G = 25V$  (and  $H = 0$ ) the  $i = 3$  subband has a population of about  $0.5 \times 10^{11} \text{ cm}^{-2}$ . According to the fan chart of Figure 27 this subband is depopulated at a parallel field of about 3T. These electrons fall into the lower lying subbands so the slight rise in population in the range  $H = 1 - 5T$  for the  $i = 2$  subband seen in Figure 37 may be significant. Similarly, an increase in the  $i = 1$  population of about  $1 \times 10^{11}$  electrons per  $\text{cm}^{-2}$  occurs at  $V_G = 15V$  for a parallel field of about 5T. The fan chart indicates a total depopulation of the  $i = 2$  subband at a parallel field at about 7T.

This kind of analysis of subband depopulation has not been made for the  $i = 3$  subband since SdH oscillations from this subband are not observed in the existing angle sweep data. A more detailed study at low magnetic fields and high gate voltages should produce such data. If such an analysis were to reveal a rise in the population of the  $i = 3$  subband, this would provide further evidence for the existence of an  $i = 4$  subband.

## E. Discussion of Parallel and Tipped Fields

### 1. Electrical Transport

Depopulation of hybrid subbands by a parallel field has been seen also in GaAs.<sup>75</sup> In particular, the device consists of alternating  $n$ -type and  $p$ -type layers of GaAs, with  $n = p = 7 \times 10^{17} \text{ cm}^{-3}$ . By an appropriate choice of the layer thicknesses, electrons are confined in a parabolic potential well in the  $n$ -type layers and form subbands with a uniform energy spacing. The 2D electron number density can be altered (by a factor of about two) by the application of a voltage between the  $n$  — and  $p$  — type layers. The usual SdH effect is observed in the normal field configuration. However, in the parallel field, the resistance shows oscillatory structure which is attributed to the total depopulation of a subband. In both field orientations the energy spacing between subbands is determined from analytical solutions of Schrödinger's equation (with a parabolic potential), and is written in terms of the (experimentally determined) surface electric and magnetic fields. The intersubband energy spacing is found to decrease with increasing 2D number density. This result is quite contrary to the behavior of MOSFET accumulation and inversion layers.

Maan *et al.*<sup>75</sup> make the argument that in the parallel field configuration the peak in resistance should be associated with the coincidence of the subband minima with the Fermi level (see § IV.C.1.a). This is based on two reasons: 1) the density of states increases as the parallel field increases, reaching a maximum value at depopulation, hence the intrasub-

band scattering rate and its contribution to the resistance reach maximum at depopulation, and 2) the intersubband scattering mechanism vanishes at depopulation and therefore the resistance decreases.

Evidence for this last assertion is found in a 2D electron gas in a GaAs/AlGaAs heterojunction in a perpendicular magnetic field.<sup>69</sup> There, the high mobility electron gas forms just inside the GaAs surface, and the 2D number density is variable over a small range ( $\sim 7.5 - 9.5 \times 10^{11} \text{ cm}^{-2}$ ) by an externally applied gate voltage. The usual (normal field) SdH effect shows that the population of a second subband can be induced within this variable range of gate voltages. However, a slight decrease in the surface density as determined via the Hall effect occurs at the gate voltage corresponding to the excited state threshold voltage. This deviation indicates that the scattering rates and hence mobilities of the two subbands are different. Indeed, the measured Hall mobility, taken to be about equal to the mobility of the ground state subband, decreases by about 30% at the excited state threshold gate voltage. This is an indication of the onset of intersubband scattering with the occupation of the excited state.

In a similar sample (GaAs/AlGaAs heterojunction) with two subbands normally occupied, the application of a parallel field diamagnetically shifts the subbands in energy, increasing the subband separation (although not completely depopulating the excited state) and therefore decreasing the intersubband scattering rate, as manifested in a drop in the device resistance.<sup>87</sup>



In an experiment on a *p*-type InSb MOSFET the SdH effect in normal and tipped magnetic fields reveals two subbands in the surface inversion layer.<sup>86</sup> In a parallel field, however, the transconductance has structure similar to that of Figure 24b. Just as in the case of InAs, the InSb structure is attributed to the occupation of a subband and it shifts in gate voltage with a variation of parallel field.<sup>88</sup> Indeed, according to the interpretation of § IV.C.1.a, there are up to three [Figure 8, reference 86] or four [Figure 9, reference 88] subbands occupied in InSb. This hybrid structure also appears in the transconductance for  $H = 0$  in contrast to the present case of InAs, where no structure is observed (see Figure 42). This lack of structure in InAs at  $H = 0$  may be due to surface scattering; the structure is observed for  $H_{\parallel} \neq 0$ , where the scattering rate has decreased with increasing parallel field.<sup>24</sup>

Mercury Cadmium Telluride, another small band gap, high mobility semiconductor, exhibits the same effect:<sup>89</sup> transconductance structure attributed to hybrid subband occupation shifts in  $V_G$  with a change in parallel field. In this material, however, spin split transconductance minima in parallel fields are quite readily apparent.

Another system in which normally two subbands are occupied is the electron layer in a GaInAs-AlInAs heterojunction described in reference 74. With a fixed 2D number density ( $n \sim 7 \times 10^{11} \text{ cm}^{-2}$  determined from the normal field SdH effect) a strong parallel field diamagnetically shifts the subbands up in energy and depopulates the first excited subband.

This depopulation is seen in both the resistivity structure in parallel field (here again, as broad negative magnetoresistance (at  $H_{\perp} \sim 6T$ )) and in the tipped field SdH oscillations. At large tipped field angles ( $80^{\circ} \leq \theta \leq 85^{\circ}$ ), the SdH oscillations are not periodic in inverse field, the fact of which indicates the varying populations of the two subbands. The subband populations thus determined (from the periods) are plotted against  $H_{\parallel}$  and it is found that the number density of the ground state (excited state) increases (decreases) as the parallel field increases up to  $H_{\parallel} \sim 6T$ . In this method of determining the subband population the sum of the two subband number densities gives the same value as that determined from the normal field SdH effect, as expected.

## 2. Infrared Absorption

At small tipped field angles ideal 2D behavior is shown by the InAs MOSFET, as evidenced in Figure 34 where the SdH structure is pushed to higher fields as  $\frac{1}{\cos \theta}$ , indicating a dependence on only the perpendicular field component. At large angles, however, quasi-2D behavior is seen, as for example in the hybrid oscillations. This is because in strong fields the cyclotron orbit diameter is on the order of the accumulation layer thickness. If the cyclotron orbit diameter is small compared to the accumulation layer thickness, 3D-like behavior may occur. Examples of such behavior are the cyclotron resonance in inversion layers on *p*-type PbTe,<sup>90</sup> and infrared absorption on InSb.<sup>91,92</sup> In fact, a recent publication reports SdH oscillations in a 2DEG on GaAs/GaAlAs with the magnetic field parallel

to the layer surfaces.<sup>108</sup>

In the usual normal field resonance experiment the transmittivity or reflectivity of the surface space charge layer is plotted against magnetic field strength. The 2D cyclotron resonance peak position,  $H_{res} = \omega m^* c/e$  (where  $\omega$  is the incident photon angular frequency), shifts in  $H$  with varying surface number density,<sup>93</sup> since the non-parabolicity of the subbands manifests itself in the carrier effective mass. In an experiment on InSb,<sup>91</sup> the normal field absorption resonance at  $\hbar\omega \sim 30$  meV is attributed to a Landau level  $0 \rightarrow 1$  transition in the ground state subband. Tipping the magnetic field away from the surface normal pushes the resonance to higher fields as  $\frac{1}{\cos \theta}$ , for small angles. This is 2D-like behavior. However, at large angles,  $\theta \geq 30^\circ$ , the resonance peak (at  $H \sim 4$  T) splits into two maxima, with the high field peak vanishing with increasing  $\theta$ , and the low field peak position not changing as  $\theta \rightarrow 90^\circ$ . This low field resonance behavior is 3D-like. In fact, at  $\theta = 90^\circ$  the absorption peak position no longer shifts in  $H$  with changing surface number density.<sup>92</sup>

At lower incident photon energy,  $\hbar\omega \sim 10$  meV, the InSb inversion layer absorption spectra is 2D-like in a parallel field,<sup>92</sup> since the peak positions shift in  $H$  with varying  $N_s$ . Two resonance peaks are observed (both near  $H \sim 2$  T). This parallel field absorption is due to transitions between hybrid subbands. The 3D-like behavior occurs when the cyclotron orbit center coordinate is inside the semiconductor so the orbits can be completed, and for 2D-like behavior, the center coordinate is well outside

the semiconductor so (classically) specular reflection occurs from the surface. The same experiment performed on a sample like the InAs epitaxial sample used here, where typical intersubband energy spacing is the order of 100 meV, should be interesting because more hybrid subbands can be occupied. This should lead to a more complex absorption spectrum. In principle, one could map the hybrid subband energy spacing as a function of parallel field and gate voltage, and hence measure the diamagnetic energy shift. However, it is not quite so simple, since the hybrid minima do not coincide in  $k_t$ , the in-plane wave vector transverse to the magnetic field direction. At any rate, in order to extract the diamagnetic energy in this way one must know the electric subband energy spacing. This electric subband energy spacing in InAs has been measured as a function of  $N_s$  in a reflectivity experiment. The range of fixed incident photon energies is  $\hbar\omega \sim 110\text{-}140$  meV, as reported in reference 63 and mentioned in § II.E.4.

A parallel field resonance experiment on a heterostructure superlattice of alternating InAs (1000 Å) and GaSb (1000 Å) reveals strong absorption due to transitions between hybrid subbands.<sup>29</sup> In this structure an electron accumulation layer ( $\sim 500$  Å) forms just inside each of the InAs surfaces. With a constant surface density of  $n \sim 10^{11}$  cm<sup>-2</sup>, two electric subbands are formed with an energy spacing  $\sim 10$  meV.<sup>94</sup> The hybrid dispersion relation of the accumulation layers on the two InAs surfaces are “coupled,” since the accumulation layers overlap somewhat. The energy spacing between the hybrid subbands is on the order of  $\hbar\omega_c$  (at  $k_t = 0$ )

and, as seen in the resonance data, doubles (from  $\sim 10$  meV to 20 meV) in the range  $H \sim 3$ -5 T. A magnetotransport experiment on a similar device shows 2D-like behavior in tipped fields.<sup>64</sup> However, in strong fields the spin degeneracy is lifted, showing up as doublet structure in the differential magnetoresistance, and a surface enhanced  $g$ -factor, is reported.<sup>64</sup>

## F. Temperature Dependence of Hybrid Oscillation Amplitude

The effect of temperature on the hybrid oscillation amplitude in transconductance is analyzed by analogy with the normal field SdH oscillation amplitude (see Eq. 4.4). In the normal field case the temperature dependence probes the uniform energy spacing between the Landau levels, since at a finite temperature, the Landau levels are partially occupied in accordance with the Fermi-Dirac distribution function. That is, the SdH oscillations vanish at temperatures such that  $k_B T \geq \hbar \omega_c$ . In the parallel field case, the hybrid subbands are not uniformly spaced in energy. However, if one assumes that the energy spacing,  $\Delta E$ , between hybrid subbands is independent of temperature, then the hybrid oscillation amplitude may be expected to follow the same temperature dependence.<sup>75</sup> That is, the hybrid structure should vanish at temperatures such that  $k_B T \geq \Delta E$ , as illustrated in Figure 38.

Due to the non-uniform spacing between hybrid subbands the variation in temperature is expected to probe the smallest energy spacing at the Fermi energy. The energy difference between the  $i = 2$  and  $i = 3$  electric subbands and the binding energy of the  $i = 3$  electric subband is typically on the order of 10 meV.<sup>24</sup> The energy difference between the lower lying electric subbands is somewhat greater, on the order of 100 meV. The intersubband energy spacing between electric subbands is independent of temperature in the range 4.2-100 K.<sup>63</sup> The presence of a strong magnetic field enhances the energy spacing by an amount on the

order of  $\hbar\omega_c$ . The amplitude, then, is expected to follow the temperature as

$$A \propto T \operatorname{csch}\left(\frac{2\pi^2 k_B T}{\Delta E}\right). \quad (4.18)$$

A set of transconductance curves as a function of parallel field at fixed gate voltage is shown in Figure 39 for two values of  $V_G$  at several temperatures. The temperature is varied in the range 2-30 K. The gate voltage of 25 V corresponds to  $N_s = 5.9 \times 10^{12} \text{ cm}^{-2}$ . The subband identification in the figure is taken from the hybrid fan chart (at 4.2 K) of Figure 31 (see § IV.C.2); the variable temperature data was taken during the same experimental run.

Inspection of the  $i = 4$  oscillation amplitude at  $V_G = 25\text{V}$  in Figure 39 reveals a decrease in amplitude as the temperature is increased. Here, the transconductance minima does not shift in  $H$  at the various temperatures, which indicates the temperature independence of  $\Delta E$ . The structure identified with the  $i = 3$  hybrid subband does not change amplitude in this temperature range at this gate voltage; however, the shape of the structure does change.

The ratio of the measured values  $A/T$  are plotted on a log scale against temperature, as shown in Figure 40. In this figure, the data are from the  $i = 4$  hybrid subband at  $V_G = 20\text{V}$  and  $H = 0.82T$ . In order to extract an energy value, a curve with the form of Eq. 4.18 is fit to the data. The energy value thus found is  $\Delta E = 4.4 \pm 0.5 \text{ meV}$ .

A plot against gate voltage of similarly determined energy values is given in Figure 41 for the  $i = 3$  and 4 subbands. For the  $i = 4$  subband the

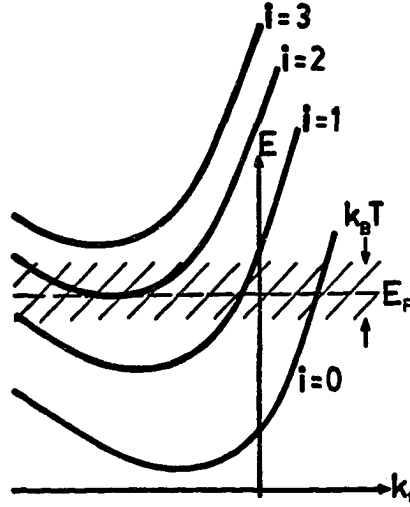


Figure 38. Hybrid Dispersion Relation. At  $T = 0$  the  $i = 2$  subband shown here at the Fermi energy would be empty. At a finite temperature it will be partially populated.

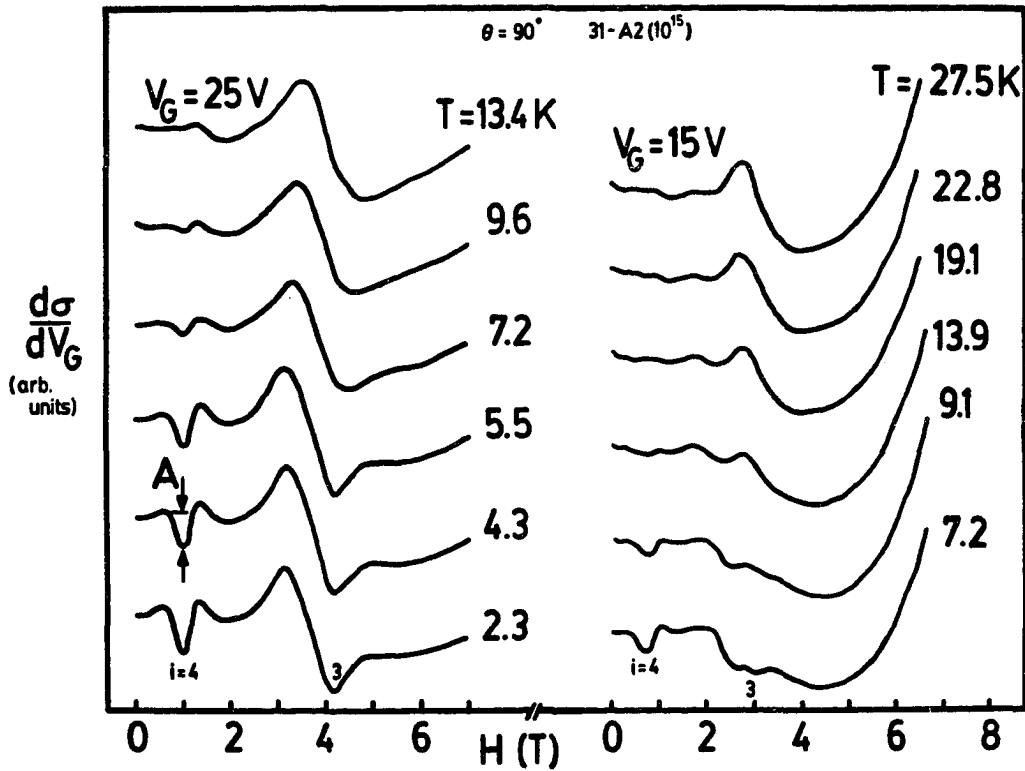


Figure 39. Temperature Dependence of the Hybrid Oscillation Amplitude. The transconductance in parallel field is plotted against field strength at two fixed gate voltages for various temperatures. The amplitude  $A$  is measured as shown for the  $i = 3$  and 4 hybrid oscillations. Note the spin splitting evident in the  $i = 3$  subband at  $V_G = 15V$ .



energy value is unchanged at the gate voltages shown. This is unexpected, since the energy difference between subbands increases as the gate voltage increases.

The energy values associated with the  $i = 3$  hybrid subband show a maximum value in the gate voltage range shown. The smaller than expected value of  $\Delta E = 4.5$  meV at  $V_G = 15V$  may be due to the spin splitting of the hybrid subband. In other words, this  $\Delta E$  value may be the spin splitting energy  $\hbar\omega_s$ . This structure occurs at  $H = 2.5T$ , so with  $|g| = 15$ , we have  $\hbar\omega_s = 4.3$  meV. Notice from Figure 31 that the observed onset of spin splitting in the  $i = 3$  hybrid subband is at  $V_G \sim 15V$ .

The change in shape of the  $i = 3$  structure at  $V_G = 25V$  shown in Figure 39 may be due to the spin splitting also. The minima structure at  $H \simeq 4.5T$  shifts slightly in  $H$  as the temperature is varied. At this field,  $\hbar\omega_s = 7.8$  meV.

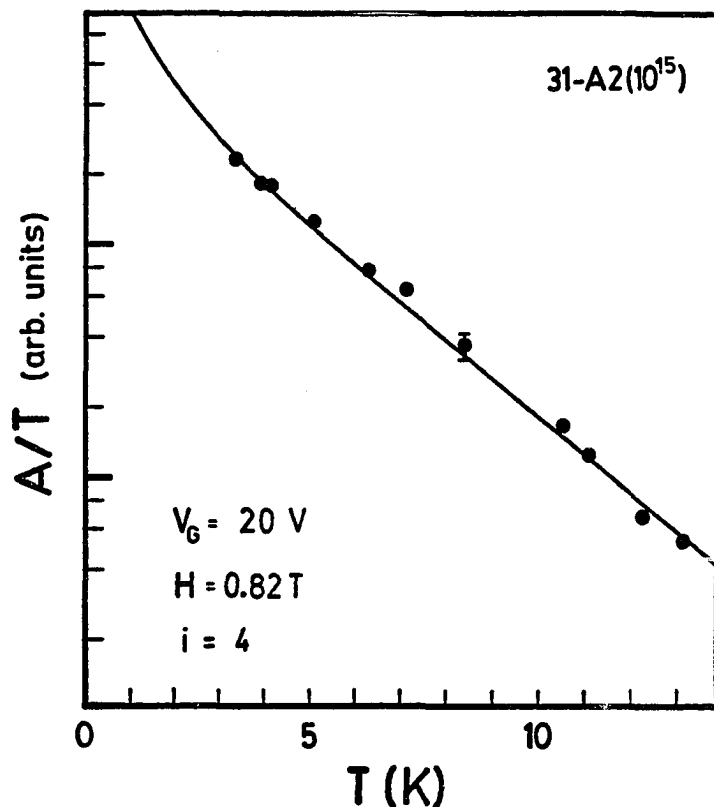
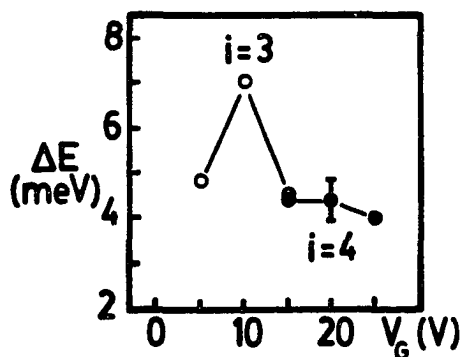


Figure 40. Amplitude Decay. The ratio of the hybrid oscillation amplitude to the sample temperature is plotted on a log scale against temperature. The curve is the function  $\text{csch}(\frac{2\pi^2 k_B T}{\Delta E})$  and is fit to the data by varying  $\Delta E$ .



$i=3$			$i=4$		
$V_G \text{ (V)}$	$H \text{ (T)}$	$\Delta E \text{ (meV)}$	$V_G \text{ (V)}$	$H \text{ (T)}$	$\Delta E \text{ (meV)}$
5	15	4.8	15	0.68	4.4
10	19	6.9	20	0.82	4.4
15	2.5	4.5	25	0.95	3.9

Figure 41. Hybrid Subband Energy Spacing. The energy value  $\Delta E$ , as determined by the analysis of Figure 40, is plotted against gate voltage. The open (filled) symbols are for the  $i=3$  ( $i=4$ ) hybrid oscillations. The data in this figure do not occur at the same value of magnetic field strength, as indicated in the table.

### G. Magnetic Freeze-Out of Impurity Band Conduction

Impurities in the semiconductor-oxide interface create states at the surface which may be filled and emptied by varying the gate voltage. The charge in the interface states affects the surface potential, can cause a shift in the voltage at which flat band occurs,<sup>96</sup> and can be observed as a broadening of the width in  $V_G$  of the low frequency capacitance minima.<sup>97</sup> In an AC measurement, “slow” surface states are those for which the associated electron scattering rate is small compared to the AC frequency, and hence have slow response to changes in gate voltage. Slow surface states lead to hysteresis in the capacitance as the DC component of the gate voltage is swept up and down through the range of  $V_G$  which fills the surface states.<sup>98</sup>

A residual peak in the transconductance-*versus*-gate voltage curves below the accumulation threshold in perpendicular magnetic field is shown in Figure 42. The peak is due to impurities near the surface that create an impurity band below the conduction band edge.<sup>99,100</sup> The peak position in the transconductance (down sweep) is independent of  $H$  and occurs at a gate voltage of  $V_G = -6.0V$ , well below the threshold for accumulation. The density of states for an impurity band below a 2D electric subband is shown schematically in Figure 43. The impurity peak in conductance is presumed to occur at the peak density of states, so the impurity band is half filled at the conductance peak.

An upper limit estimate of the number of electrons in the impurity

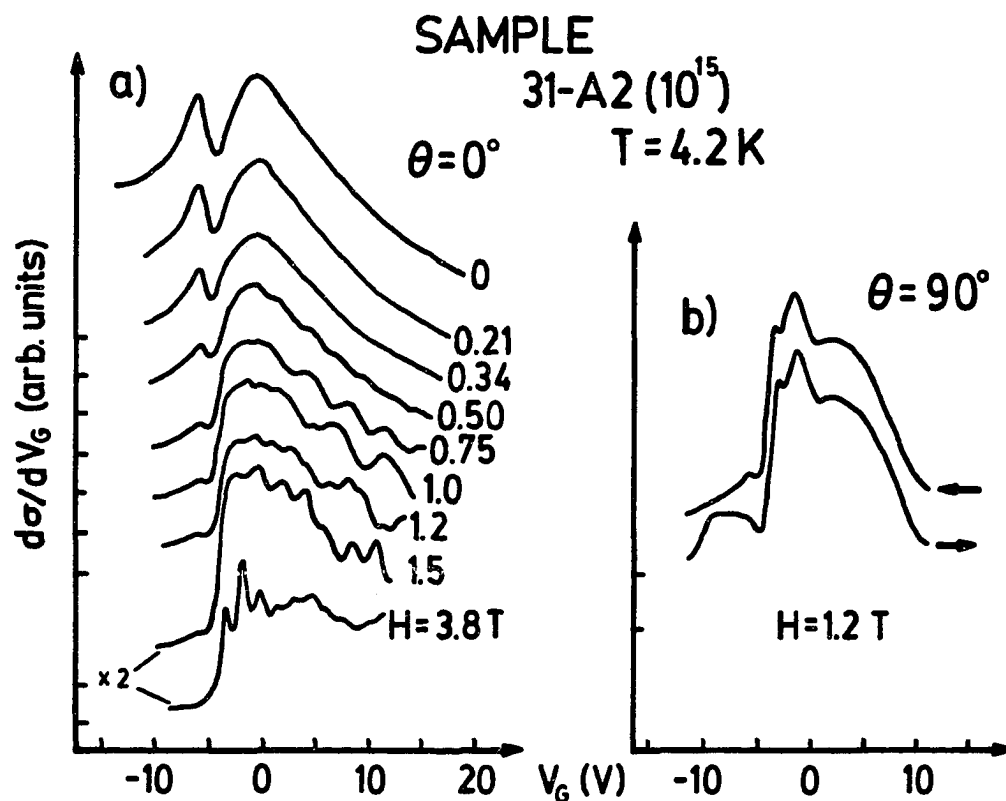


Figure 42. Impurity Band Transconductance. The peak in transconductance below threshold is due to a 2D impurity band at the semiconductor surface. (a) As the field increases the peak height decreases. The peak position in  $V_G$  ( $-6.0\text{V}$ ) does not shift with varying  $H$ . All of the data are taken by sweeping  $V_G$  down. (b) At  $H = 1.2\text{ T}$  in the parallel configuration the amplitude is somewhat greater compared to the  $\theta = 0$  trace. The hysteresis is evident at all angles but shown only for  $\theta = 90^\circ$ .

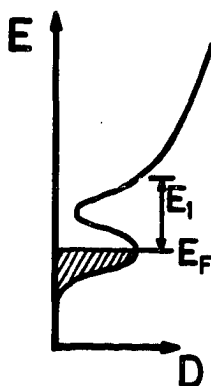


Figure 43. Impurity Band Density of States. The peak in conductivity occurs at the maximum density of states, so the band is half full.  $E_1$  is the activation energy to the mobility edge in the conduction band tail.

band can be made via the device capacitance. Since the impurity conduction is observed near flat band the device capacitance is substantially less than the oxide capacitance. Using an estimate of a decrease of about 40% from Figure 46, the number of charges per unit area that fill the impurity states is (see Eqs. 2.11 and 4.6)

$$N_{ox} = 0.95 \times 10^{11} \Delta V_G \text{ cm}^{-2} \text{V}^{-2} \quad (4.19)$$

where  $\Delta V_G$  is the width of the peak in gate voltage. One method of determination of  $\Delta V_G$  is the peak's full width at half maximum. For  $H=0$ ,  $\Delta V_G = 2\text{V}$ , and therefore  $N_{ox} = 2 \times 10^{11} \text{ cm}^{-2}$ . Another method for determining  $N_{ox}$ , given in reference 96, is to define  $\Delta V_G$  as the shift in threshold between liquid nitrogen temperature and liquid helium temperature.

The peak width decreases with increasing  $H$ , which means that the number of electrons that contribute to the impurity conduction decreases also. Furthermore, the transconductance at the peak position decreases with increasing field and is effectively frozen-out by  $H \sim 1.5 \text{ T}$ , as illustrated in Figure 44.

That the carriers are frozen-out by the magnetic field may be explained by the theory of Yafet, Keyes, and Adams (YKA).<sup>101-103</sup> The ground state binding energy of a hydrogenic impurity atom at the semiconductor/insulator interface is the effective Rydberg energy

$$Ry^* = Ry \left( \frac{m^*}{m_e} \right) \frac{1}{\kappa^2}, \quad (4.20)$$

where  $\bar{\kappa} = \frac{1}{2}(\kappa_{\infty} + \kappa_{ins})$  is an average dielectric constant and  $Ry=13.6$  eV is the Rydberg energy. Thus the impurity states at the InAs/SiO<sub>2</sub> interface have binding energies of  $Ry^*=5.1$  meV, compared to a value of about 44 meV at the Si/SiO<sub>2</sub> interface. The difference is essentially due to the greater effective mass in Si. With the application of a large magnetic field such that the Landau level separation is comparable to the effective Rydberg energy, the ground state hydrogenic wavefunction is compressed, although primarily in the direction perpendicular to the field direction (i.e., the electron cloud becomes egg-shaped), and the binding energy increases.<sup>101</sup> The dimensionless parameter

$$\gamma = \frac{\hbar\omega_c}{2Ry^*} \quad (4.21)$$

describes the condition for freeze-out: whenever  $\gamma > 1$ . The freeze-out observed at 1.5 T in Figure 44 leads to a value  $\gamma=0.7$ .

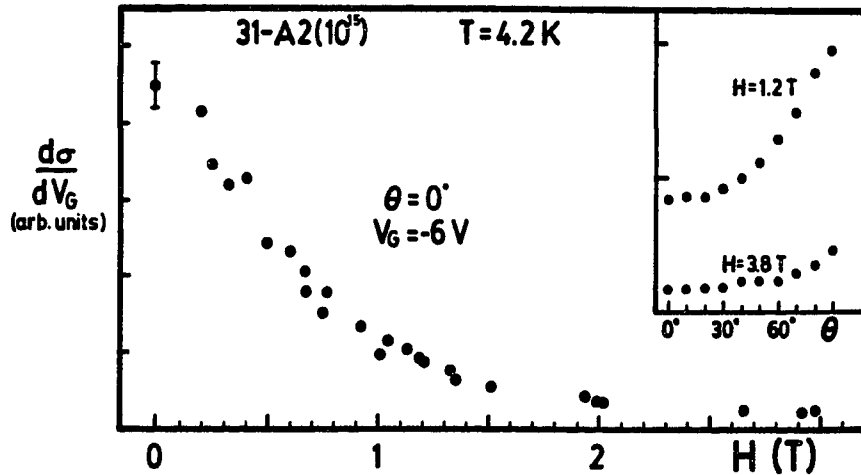


Figure 44. Magnetic Freeze-Out. The amplitude of the impurity band peak transconductance is plotted against magnetic field. The transconductance is effectively frozen-out by  $H \sim 1.5T$  for  $\theta = 0$ . The inset shows that at perpendicular fields strong enough to freeze-out the transconductance, tipping the field away from the surface normal increases the peak amplitude.

The freeze-out of conduction in the impurity band occurs when the nearest neighbor spacing between impurities is large (say, by an order of magnitude<sup>102</sup>) compared to the effective Bohr radius. The YKA theory is valid if neighboring impurities about which the electrons become localized are separated to an extent that the wavefunctions do not overlap, although the impurity band occurs only if there is some overlap. The effective Bohr radius is

$$a_B^* = a_B \left( \frac{m^*}{m_e} \right)^{-1} \kappa, \quad (4.22)$$

where  $a_B = 0.529 \text{ \AA}$  is the Bohr radius. The value for InAs/SiO<sub>2</sub> is 180  $\text{\AA}$ , much greater than the value 20  $\text{\AA}$  for Si/SiO<sub>2</sub>. Using the value of  $N_{ox}$  given above as a valid measure of the impurity density, then if it is assumed that the impurities are uniformly distributed, the nearest-neighbor spacing is given by  $\frac{1}{\sqrt{N_{ox}}} = 230 \text{ \AA}$ , slightly more than one effective Bohr radius.

It is not at all clear what sort of impurities are in the InAs/SiO<sub>2</sub> interface, or even exactly where they are. It is quite possible for example that sodium ions have gotten into the SiO<sub>2</sub> and have diffused to the interface. (Sodium ions are mobile in SiO<sub>2</sub> at room temperature, but frozen into place below that temperature, and are known to produce bound states at Si/SiO<sub>2</sub> interfaces. See reference 3, page 530.) This conjecture may explain the peculiar behavior of the accumulation threshold gate voltage as described in § IV.C.2. In the run with the threshold at  $-13.6 \text{ V}$  (when hybrid subband spin splitting was present) the impurity conduction was not present. Inconsistent with this explanation, however, is another run

(data from which is shown in figure 46). The threshold voltage is  $\sim -15$  V and the impurity conduction is observed. Thus, the origin of the impurity conduction is left unresolved. On the other hand, presumably the impurity-band ions are not completely responsible for the shift in gate voltage threshold.

It may be that the impurity states at the interface are due to the electron donors within about a depletion width of the surface. For the case at hand, the depletion width is  $\sim 440$  Å (Eq. 2.2), so with the assumption that the donors are uniformly distributed, the number of donors in the depletion region is  $\sim 8.8 \times 10^9 \text{ cm}^{-2}$ . This, then, gives a nearest neighbor spacing of  $\sim 9 a_B^*$ . This low density may suggest that the donor ions are not the impurity ions.

Three-dimensional magnetic freeze-out has been reported in InSb both experimentally<sup>104</sup> and theoretically.<sup>105</sup> This material has a higher dielectric constant and a lower effective mass than InAs, and both differences serve to enhance the effect.

Two-dimensional magnetic freeze-out of impurity conduction is observed in a Si/SiO<sub>2</sub> interface.<sup>106,107</sup> In these experiments the impurity band ( $N_{ox} \sim 4 - 5 \times 10^{11} \text{ cm}^{-2}$ ) is caused by the deliberate introduction of sodium into the SiO<sub>2</sub>.

A parallel field suppresses the conduction in the impurity band, as well. However, the effect of the parallel field is not as strong as the perpendicular field, as can be seen in Figure 42. The inset of Figure 44



shows that with a magnetic field strong enough to freeze-out the transconductance, tipping the field away from the surface normal increases the transconductance. This tipped field behavior indicates the 2D nature of the impurity band. The idea is illustrated physically in this way: with no magnetic field an impurity state electron cloud is already compressed in the direction normal to the surface by the surface electric field. As the magnetic field is applied normal to the surface the electron cloud condenses in the plane of the surface, cutting off the conduction path between nearest neighbor impurities. If the field is applied parallel to the surface, the effect is to compress the electron cloud in one direction in which it is already compressed. Therefore, it requires a larger parallel field to cut off the conduction. This idea is shown schematically in Figure 45.

A strong hysteresis is evident in the impurity peak as the gate voltage is swept up and down. This is seen in Figure 42 and again in Figure 46. Along with the transconductance in Figure 46 is the device capacitance. Notice that the capacitance has structure only in the up sweep. Furthermore, the capacitance is unaffected by the presence of a magnetic field which is strong enough to suppress the impurity conduction. The hysteresis in transconductance and the glitch in capacitance may be understood in terms of the filling (up sweep) or emptying (down sweep) of the impurity band. Beginning with a strong negative gate voltage, as the impurity band is being filled the sharp rise (compared to the down sweep) in both transconductance and capacitance is probably due to the enhancement

of the surface electric field by the positively charged impurities. This field enhancement is absent at the beginning of the down sweep, since the impurities are filled. The magnetic field has no effect on the capacitance since the capacitance depends only on the number of charges and their location, not whether they conduct electricity.

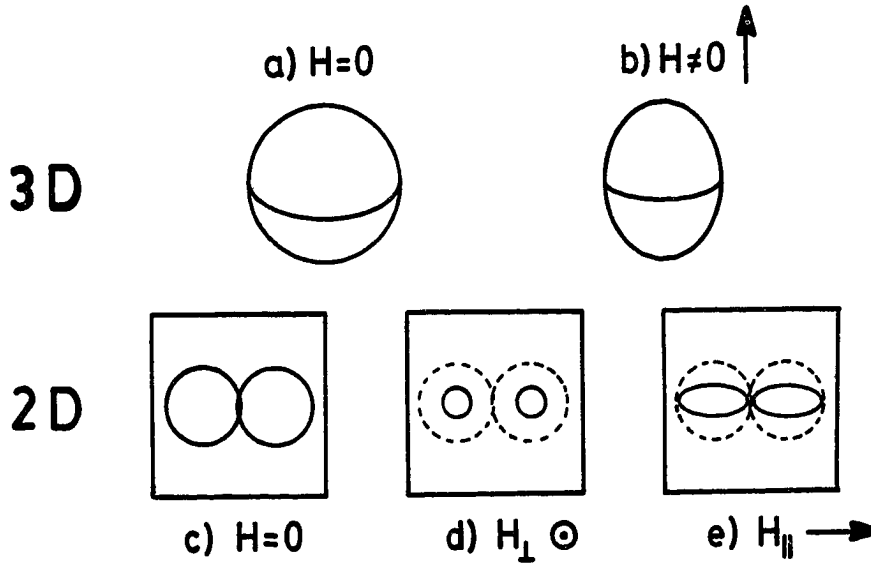


Figure 45. Electron Clouds. (a) In 3D isotropic configuration space the electron cloud is spherical if there is no magnetic field. (b) With a non-zero magnetic field the electron cloud becomes egg- or cigar-shaped. (c) In 2D shown here are two impurities slightly overlapping with no magnetic field. Impurity conduction can occur. The square represents the plane of the 2DEG. (d) In a perpendicular magnetic field the conduction path is cut off. The dotted lines are for  $H = 0$ . (e) In a parallel field the electron clouds are condensed in only one in-plane direction, shown here with a path for conduction.

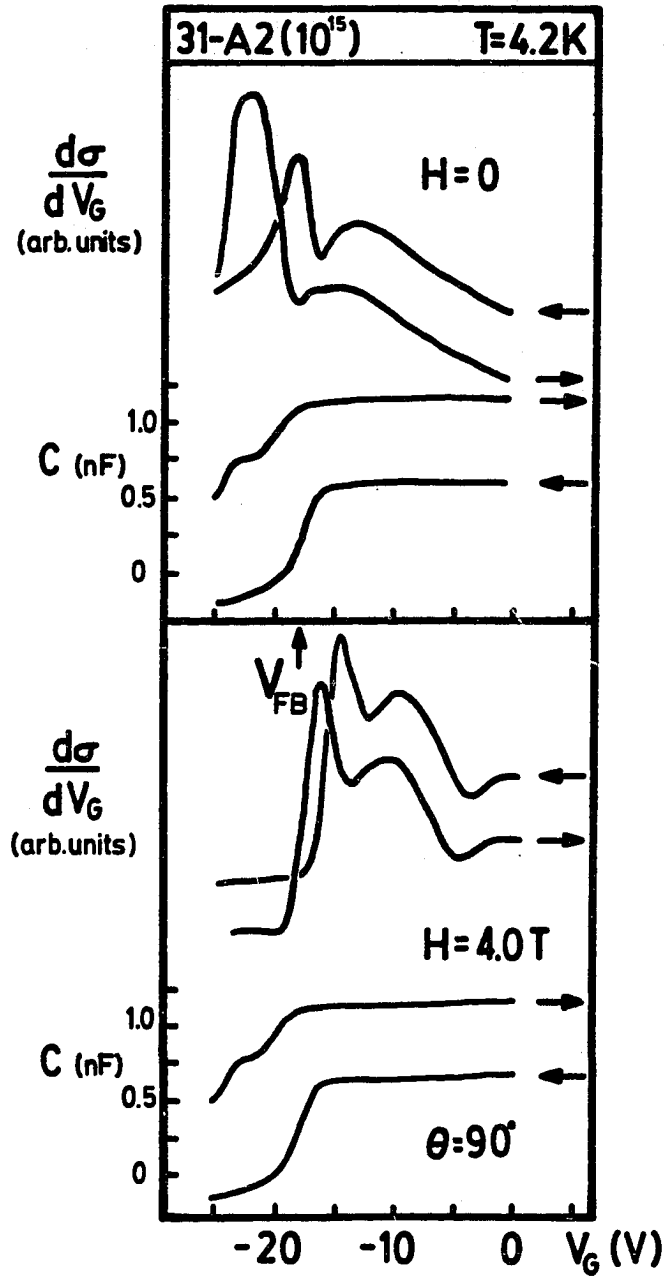


Figure 46. Capacitance. The hysteresis is illustrated in the capacitance and again in the transconductance. The glitch in capacitance is seen only in the  $V_G$  up sweep. The scale for the capacitance traces goes with the up sweeps; the down sweep is shifted vertically down for clarity but has the same scale. At fields strong enough to freeze-out the transconductance the capacitance is unchanged. The flat band voltage ( $V_G = -18V$ ) is identified via the capacitance, calculated from equation 23, p. 372 in reference 16. Notice that at a gate voltage corresponding to the peak in the impurity transconductance, the capacitance has decreased as much as about 40% relative to the oxide capacitance.

## CHAPTER V

### CONCLUSIONS

#### A. Summary

Oscillations in the transconductance of two *n*-type InAs samples are observed in the parallel field configuration. The crossed surface electric and magnetic fields are coupled and give rise to hybrid dispersion relations for the surface electrons. For small magnetic fields, the field is treated as a perturbation of the electric subbands and the field diamagnetically raises the energy of the electric subbands. In large fields where the perturbation approach breaks down the energy increase is taken to be on the order of  $\hbar\omega_c$ . Thus in large parallel fields the hybrid subbands depopulate as they are pushed up in energy and are emptied completely as the subband minima are pushed above the Fermi level. This total depopulation causes the hybrid subband structure in the transconductance. Consequently, a hybrid fan chart of subband threshold shifts is made.

In the weakly degenerate epitaxial sample with a bulk carrier concentration  $n = 2.0 \times 10^{15} \text{ cm}^{-3}$ , up to five hybrid subbands are observed, whereas, only four subbands are evident in the perpendicular field transconductance (SdH effect) and cyclotron resonance.

In a second experimental run on the epitaxial sample, in which the gate and source were shorted during cool-down, the surface impurity band vanished. Therefore, presumably, the surface potential was much more smooth. This then, allowed the hybrid spin splitting to be resolved in the transconductance.

If the magnetic field is tipped at some angle away from the surface normal the perpendicular field component produces the SdH effect and the parallel field diamagnetically shifts the subband energies. At small angles the SdH oscillations depend only on the normal field component. At large angles the subband depopulation is observed via the SdH period, where the period is assumed to depend on only the perpendicular field component. The decrease in number density thus determined is plotted against parallel field, and is consistent with the parallel field (only) hybrid depopulation.

The hybrid oscillation amplitude is made to decrease by increasing the sample temperature. Analysis of the temperature dependence is made by analogy with the SdH oscillation amplitude temperature dependence. The energy decay associated with the  $i = 4$  hybrid subband in the epitaxial sample is probably the binding energy of the subband. The energy value is  $\sim 4$  meV and is independent of gate voltage in the range over which the subband is occupied. The energy value determined by the temperature decay of the  $i = 3$  hybrid subband is probably the energy spacing between the  $i = 3$  and  $i = 4$  subbands, except at  $V_G = 15$  V. At this voltage the temperature decay appears to measure the spin splitting energy.

The epitaxial sample shows structure in the transconductance at gate voltages below the accumulation threshold. This structure is due to conduction via impurity states at the semiconductor/oxide interface and vanishes with increasing magnetic field. This magnetic freeze-out of conduction is understood in terms of nearly isolated impurities with ground state hydrogenic wave functions. The overlap of impurity states creates a two-dimensional impurity conduction band. The two-dimensional nature of the impurity band is illustrated by tipping the magnetic field away from the surface normal, since a stronger magnetic field is required in tipped fields to produce the same freeze-out effect as a perpendicular field. The device capacitance shows structure due to the impurities which is independent of the magnetic field.

### B. Further Investigations

A self-consistent calculation, or a more realistic model, of the InAs parallel field surface potential well would be interesting since the diamagnetic energy shift in strong fields could be more precisely estimated. Here, the shift is taken to be on the order of  $\hbar\omega_c$  for all subbands, although it is dependent on the wavefunction extent into the semiconductor, and therefore different for the different subbands. Furthermore, the estimates made here for the subband energies are based on the triangular potential well, which is more properly used for the lower lying electric subbands since it overestimates the potential for the higher energy subbands. The spin splitting and the temperature dependence of the hybrid subbands is

investigated primarily in these higher lying hybrid subbands where the triangular potential is expected to be least valid.

In this connection it may be interesting to perform spectroscopy experiments (in the infrared) on the hybrid subbands in order to measure the intersubband energy spacing as a function of magnetic field strength and gate voltage. Using the temperature dependence as a measure of the energy spacing is valid; however, a wider range of gate voltage and temperature should be useful in understanding the field dependence of the intersubband energies.

A calculation of the conductance line shape in the parallel field configuration should help resolve the problem of subband identification. A misidentification of structure in conductance that corresponds to the coincidence of the subband minima at the Fermi level may lead to a misunderstanding of the observed behavior.

Finally, the temperature dependence of the impurity conductance at various magnetic fields needs to be investigated in order to determine the conductance mechanism. The conductance is most likely by hopping between impurities, so by fitting the data to an expected temperature dependence one may extract the activation energy for hopping.

## APPENDIX A

## Properties of Bulk InAs

Properties	Comments	Reference
<b>Band Gap</b>		
$E_G = 0.360 \pm 0.002$ eV	T $\sim$ 300K, optical	45
$E_G = 0.41$ eV	T $\sim$ 77K, optical	73
$E_G = 0.44 \pm 0.01$ eV	T $\sim$ 0K, optical	46
<b>Mobility</b>	Hall effect	
$\mu = 30000$ cm <sup>2</sup> /Vs	T $\sim$ 300K, $n = 1.7 \times 10^{16}$ cm <sup>-3</sup>	47
<b>Effective Mass</b>		
$\frac{m^*}{m_e} = 0.023 \pm 0.002$	T $\sim$ 80K cyclotron resonance	48
<b>Landé g-factor</b>		
$g = -15.0 \pm 1.0$	magneto absorption	53
<b>Dielectric Constant</b>		
static $\kappa_{sc} = 14.5 \pm 0.3$	T $\sim$ 300K, optical	57
high frequency $\kappa_\infty = 11.8 \pm 0.1$		
<b>Index of Refraction</b>		
$n = 4.5$	$\lambda = 0.5$ $\mu$ m	58
<b>Crystal Structure</b>		
zinc-blende		41
<b>Lattice Constant</b>		
$a = 6.0584 \pm 0.0001$ Å		42
<b>Conduction Band Structure</b>		
— constant energy surface		44
sphere		
— valley degeneracy		
$g_v = 1$		
— transition		
direct		



## APPENDIX B

## Physical Constants and Conversion Factors

Quantity	Symbol	Value
Free electron rest mass	$m_e$	$9.11 \times 10^{-28} \text{ g}$
Elementary charge	$ e $	$4.80 \times 10^{-10} \text{ statcoulomb}$
Speed of light <i>in vacuo</i>	$c$	$3.00 \times 10^{10} \text{ cm s}^{-1}$
Reduced Planck constant	$\hbar$	$1.05 \times 10^{-27} \text{ erg s}$
Boltzmann constant	$k_B$	$0.0862 \text{ meV K}^{-1}$

## Conversion Factors

SI	esu
farad	$9 \times 10^{11} \text{ statfarad}$
volt	$\frac{1}{300} \text{ statvolt}$
coulomb	$3 \times 10^9 \text{ statcoulomb}$
	$3 \times 10^9 \text{ cm}^{\frac{3}{2}} \text{ g}^{\frac{1}{2}} \text{ s}^{-1}$
meV	$1.60 \times 10^{-15} \text{ erg}$

## REFERENCES

1. M. Chester and L.C. Yang, *Phys. Rev. Lett.* **31**, 1377 (1973)
2. J.M. Kosterlitz and D.J. Thouless, **Progress in Low Temperature Physics**, Vol. VIIB (edited by D.F. Brewer), North-Holland, New York (1978), chapter 5, p. 371
3. T. Ando, A.B. Fowler, and F. Stern, *Rev. Mod. Phys.* **54**, 437 (1982)
4. For a review of two-dimensional physics, see reference 2
5. S.C. Yang, *Phys. Rev. B* **3**, 4160 (1971)
6. D.C. Licciardello and D.J. Thouless, *Phys. Rev. Lett.* **35**, 1475 (1975)
7. J.F. Janak, *Phys. Rev.* **178**, 1416 (1969)
8. E. Arnold, *Surface Science* **58**, 60 (1976)
9. C.C. Grimes and G. Adams, *Phys. Rev. Lett.* **42**, 795 (1979)
10. R. Dingle, H.L. Störmer, A.C. Gossard, and W. Wiegmann, *Appl. Phys. Lett.* **33**, 665 (1978)
11. G.H. Döhler, *Phys. Stat. Sol. B* **52**, 79 (1972)
12. K. von Klitzing, G. Dorda, and M. Pepper, *Phys. Rev. Lett.* **45**, 484 (1980)
13. D.C. Tsui, H.L. Störmer, and A.C. Gossard, *Phys. Rev. Lett.* **48**, 1559 (1982)
14. H.L. Störmer, A. Chang, D.C. Tsui, J.C.M. Hwang, A.C. Gossard, and W. Wiegmann, *Phys. Rev. Lett.* **50**, 1953 (1983)
15. R.B. Laughlin, *Phys. Rev. Lett.* **50**, 1395 (1983)
16. For a comprehensive review of device physics, see S.M. Sze, **Physics**

of **Semiconductor Devices**, Second edition, Wiley and Sons, New York (1981)

17. F. Stern, *Phys. Rev. B* **5** (1972)
18. H.H. Wieder, *Appl. Phys. Lett.* **25**, 206 (1974)
19. J.R. Sites and H.H. Wieder, *CRC Crit. Rev. Solid State Sci.* **5**, 385 (1975)
20. H.A. Washburn, *Thin Solid Films* **45**, 135 (1977)
21. See S.M. Sze, reference 16, chapter 7, p. 362
22. See, for example, N.W. Ashcroft and N.D. Mermin, **Solid State Physics**, Holt, Rinehart and Winston, New York (1976), chapter 2, p. 30
23. G.A. Antcliffe, R.T. Bate, and R.A. Reynolds, **Proceedings of the Conference on the Physics of Semimetals and Narrow-Gap Semiconductors**, 1970, (edited by D.L. Carter and R.T. Bate), Pergamon, New York (1971), p. 499
24. H. Reisinger, H. Schaber, and R.E. Doezema, *Phys. Rev. B* **24**, 5960 (1981)
25. F.J. Ohkawa and Y. Uemura, *J. Phys. Soc. Japan* **37**, 1325 (1974)
26. H.A. Washburn, J.R. Sties, and H.H. Wieder, *J. Appl. Phys.* **50**, 4872 (1979)
27. F. Stern, *Phys. Rev. B* **5**, 4881 (1972)
28. F.F. Fang and W.E. Howard, *Phys. Rev. Lett.* **16**, 797 (1966)
29. J.C. Maan, Ch. Uihlein, L.L. Chang, and L. Esaki, *Solid State Comm.* **44**, 653 (1982)
30. F. Stern, *Phys. Rev. Lett.* **33**, 960 (1974)
31. T. Ando, *J. Phys. Soc. Japan* **39**, 411 (1975)
32. See, for example, W.A. Harrison, **Solid State Theory**, Dover, New York (1979) p. 73
33. See, for example, P. Lorrain and D.R. Corson, **Electromagnetic Fields and Waves**, Second Edition, Freeman and Company, San Francisco

- (1970) p. 153
34. F. Stern, *J. Computational Physics* **6**, 56 (1970)
  35. See, for example, L.D. Landau and E.M. Lifshitz, Quantum Mechanics (Nonrelativistic Theory), Third Edition Pergamon Press, Oxford (1977), chapter 7, p. 164
  36. F. Stern and W.E. Howard, *Phys. Rev.* **163**, 816 (1967)
  37. T. Ando and Y. Uemura, *J. Phys. Soc. Japan* **36**, 959 (1974)
  38. T. Ando, Y. Matsumoto, and Y. Uemura, *J. Phys. Soc. Japan* **39**, 279 (1975)
  39. R.B. Laughlin, *Phys. Rev. B* **23**, 5632 (1981)
  40. M. Wanner, R.E. Doezema, and U. Strom, *Phys. Rev. B* **12**, 2883 (1975)
  41. O. Madelung, **Physics of III-V Compounds**, Wiley and Sons, New York (1964)
  42. Von G. Giesecke and G.H. Pister, *Acta. Crystl.* **11**, 369 (1958)
  43. F. Matossi and F. Stern, *Phys. Rev.* **111**, 472 (1958)
  44. D. Long, *J. Appl. Phys.* **33**, 1682 (1962)
  45. S. Zwerdling, B. Lax, and L.M. Roth, *Phys. Rev.* **108**, 1402 (1957)
  46. J.R. Dixon and J.M. Ellis, *Phys. Rev.* **123**, 1560 (1961)
  47. T.C. Harman, H.L. Goering, and A.C. Beer, *Phys. Rev.* **104**, 1562 (1956)
  48. E.D. Palik and R.F. Wallis, *Phys. Rev.* **123**, 131 (1961)
  49. E.O. Kane, **Semiconductors and Semimetals, Vol. 1, Physics of III-V Compounds** (edited by R.K. Willardson and A.C. Beer), Academic Press, New York (1966), chapter 3, p. 75
  50. A.B. Fowler, F.F. Fang, W.E. Howard, and P.J. Stiles, *Proceedings of the International Conference on the Physics of Semiconductors, Kyoto, 1966*, *J. Phys. Soc. Japan* **21**, Supplement p. 331

51. F.F. Fang and P.J. Stiles, *Phys. Rev.* **174**, 823 (1968)
52. T. Ando and Y. Uemura, *J. Phys. Soc. Japan* **37**, 1044 (1974)
53. C.R. Pidgeon, D.L. Mitchell, and R.N. Brown, *Phys. Rev.* **154**, 737 (1967)
54. H. Reisinger, Diplom Thesis, Technische Universität München (1978), unpublished
55. R.J. Wagner, T.A. Kennedy, and H.H. Wieder, *Proceedings of the Third International Conference on the Physics of Small Gap Semiconductors*, Warsaw, 1977 p. 427
56. For sample 31-A2( $10^{15}$ ) see references 55, 26, 62, and see also 18-20. For sample IAS/34( $10^{17}$ ) see references 24 and 54.
57. O.G. Lorimor and W.G. Spitzer, *J. Appl. Phys.* **36**, 1841 (1965)
58. B.O. Seraphin and H.E. Bennett, **Semiconductors and Semimetals, Vol. 3, Optical Properties of III-V Compounds** (edited by R.K. Willardson and A.C. Beer), Academic Press, New York (1967) p. 499
59. D.C. Tsui, *Phys. Rev. B* **4**, 4438 (1971); see also reference 68 and references therein
60. J.A. Appelbaum and G.A. Barraff, *Phys. Rev. B* **4**, 1235 (1971); see also G.A. Barraff and J.A. Appelbaum, *Phys. Rev. B* **5**, 475 (1972) and references therein
61. D.C. Tsui, *Solid State Comm.* **9**, 1789 (1971)
62. H.A. Washburn and J.R. Sites, *Surface Science* **73**, 537 (1978)
63. H. Reisinger and F. Koch, *Solid State Comm.* **37**, 429 (1980)
64. L.L. Chang, E.E. Mendez, N.J. Kawai, and L. Esaki, *Surface Science* **113**, 306 (1982)
65. J.R. Clement and E.H. Quinzel, *Rev. Sci. Inst.* **23**, 213 (1962)
66. G.K. White, **Experimental Techniques in Low Temperatures Physics**, Second Edition, Clarendon Press, Oxford (1968), appendix table A, p. 307
67. R.J. Donnelly, **Experimental Superfluidity**, University of Chicago Press,

Chicago (1967), Appendix C, Table 1, p. 214

68. D.C. Tsui, *Phys. Rev. B* **8**, 2657 (1978)
69. H.L. Störmer, A.C. Gossard, and W. Wiegmann, *Solid State Comm.* **41**, 707 (1982)
70. Y. Uemura, Proceedings of the Twelfth International Conference on the Physics of Semiconductors, Stuttgart, 1974, (edited by M.H. Pilkuha), B.G. Teubner, Stuttgart (1974) p. 665
71. W. Beinvogl, A. Kamgar, and J.F. Koch, *Phys. Rev. B* **14**, 4274 (1976)
72. Th. Englert, J.C. Maan, D.C. Tsui, and A.C. Gossard, *Solid State Comm.* **45**, 989 (1983)
73. R.E. Doezema, M. Nealon, and S. Whitmore, *Phys. Rev. Lett.* **45**, 1593 (1980)
74. J.C. Portal, R.J. Nicholas, M.A. Brummell, A.Y. Cho, K.Y. Cheng, and T.P. Pearsall, *Solid State Comm.* **43**, 907 (1982)
75. J.C. Maan, Th. Englert, Ch. Uihlein, H. Künzel, A. Fischer, and K. Ploog, *Solid State Comm.* **47**, 383 (1983)
76. E.D. Palik and J.R. Stevenson, *Phys. Rev.* **130**, 1344 (1963)
77. T. Ando, *J. Phys. Soc. Japan* **37**, 1233 (1974)
78. E.N. Adams and T.D. Holstein, *J. Phys. Chem. Solids* **10**, 254 (1959)
79. K. Seeger, **Semiconductor Physics**, Second Edition, Springer-Verlag, New York (1982) p. 279
80. R.B. Dingle and D. Shoenberg, *Nature (London)* **166**, 652 (1950); see also R.B. Dingle, *Proc. Royal Soc. London A* **211**, 517 (1952)
81. G. Bauer and H. Kahlert, *Phys. Rev. B* **5**, 566 (1972)
82. W. Beinvogl and J.F. Koch, *Phys. Rev. Lett.* **40**, 1736 (1978)
83. S.K. Bhattacharya, *Phys. Rev. B* **25**, 3756 (1982)
84. M. Nealon, S. Whitmore, R.R. Bourassa, and R.E. Doezema, *Surface Science* **113**, 282 (1982)

85. S. Tansal, A.B. Fowler, and R.F. Cotellessa, *Phys. Rev.* **178**, 1326, (1969)
86. N. Kotera, Y. Katayama, and K.F. Komatsubara, *Phys. Rev.* **B5**, 3065 (1972)
87. Th. Englert, J.C. Maan, D.C. Tsui, and A.C. Gossard, *Solid State Comm.* **45**, 989 (1983)
88. F. Koch, **Physics in High Magnetic Fields** (edited by S. Chikazumi and N. Miura), Springer-Verlag, Berlin (1981) p. 262
89. F. Koch, private communication
90. H. Schaber and R.E. Doezema, *Phys. Rev. B* **20**, 5257, (1979)
91. J.H. Crasemann and U. Merkt, *Solid State Comm.* **47**, 917 (1983)
92. J.H. Crasemann, U. Merkt and J.P. Kotthaus, *Phys. Rev. B* **28**, 2271 (1983)
93. A Därr, J.P. Kotthaus, and J.F. Koch, *Solid State Comm.* **17**, 455 (1975)
94. L.L. Chang, N.J. Kawai, E.E. Mendez, C.-A. Chang, and L. Esaki, *Appl. Phys. Lett.* **38**, 30 (1981)
95. M. Nealon and R.E. Doezema, *Solid State Comm.* **50**, 661 (1984)
96. A.B. Fowler and A.M. Hartstein, *Surface Science* **98**, 169 (1980)
97. A.M. Voshchenkov and J.N. Zemel, *Phys. Rev. B* **9**, 4410 (1974)
98. Reference 3, p.442
99. A. Hartstein and A.B. Fowler, *Phys. Rev. Lett.* **34**, 1435 (1975)
100. A.B. Fowler and A. Hartstein, *Philosophical Mag. B* **42**, 949 (1980)
101. Y. Yafet, R.W. Keyes, and E.N. Adams, *J. Phys. Chem. Solids* **1**, 137 (1956)
102. E.H. Putley, **Semiconductors and Semimetals**, Vol. 1, Physics of III-V Compounds (edited by R.W. Willardson and A.C. Bear), Academic Press, New York (1966), Chapter 9, p. 289

- 103. Reference 79, p. 282
- 104. R.W. Keyes and R.J. Sladek, *J. Phys. Chem. Solids* **1**, 143 (1956)
- 105. M. von Ortenberg, *J. Phys. Chem. Solids* **34**, 397 (1973)
- 106. A. Hartstein and A.B. Fowler, *Physica* **117B & 118B**, 655 (1983)
- 107. H. Reisinger, A.B. Fowler and A. Hartstein, Proceedings of the Fifth International Conference on Electronic Properties of Two-Dimensional Systems, Oxford, 1984. To be published in *Surface Science*
- 108. J. Yoshino, H. Sakaki, and T. Hotta, *ibid.*
- 109. D.C. Tsui, *Phys. Rev. Lett.* **24**, 303 (1970).